Research on Sensorless and Robust Control of High-Speed Surface-Mounted Permanent Magnet Synchronous Motors

by

Kai Xu

A thesis submitted in fulfilment of the requirements for the degree of

Doctor of Philosophy

under the supervision of Prof. Youguang Guo, and
Prof. Jianguo Zhu

at the
Faculty of Engineering and Information Technology

University of Technology Sydney

February 2026

Certificate of Original Authorship

I, Kai Xu, declare that this thesis is submitted in fulfillment of the requirements for the award of Doctor of Philosophy, in the School of Electrical and Data Engineering at the University of Technology Sydney.

This thesis is wholly my own work unless otherwise referenced or acknowledged. In addition, I certify that all information sources and literature used are indicated in the thesis.

This document has not been submitted for qualifications at any other academic institution.

This research was supported by an Australian Government Research Training Program (RTP) Scholarship doi.org/10.82133/C42F-K220.

Production Note:

Signature: Signature removed prior to publication.

Date: 6 February 2025

Abstract

High-speed permanent magnet synchronous motors (PMSMs) are increasingly adopted in electric vehicles, high-speed rail traction, aerospace, and flywheel energy storage systems. The advantages of PMSMs include high efficiency, compact design, and excellent dynamic performance. However, their application is limited by three key challenges: ensuring reliable and efficient performance analysis, achieving accurate sensorless control at high speeds and in flux-weakening (FW) regions, and maintaining robustness under disturbances and parameter variations. This thesis addresses these challenges through advanced modeling, estimation, and adaptive robust control strategies.

First, to strengthen fundamental analysis, a proper orthogonal decomposition-based model order reduction (MOR) method is developed for bearingless PMSMs. The approach drastically reduces computation time while preserving high accuracy in flux density, torque, levitation force, and dynamic response compared with finite element analysis. These achieve relative errors below 3.5%, enabling efficient and precise loss prediction across wide operating ranges.

Second, for sensorless control, a cascade high-order extended state observer (CHESO) is introduced to accurately estimate back-electromotive force, rotor position, load torque, and disturbances. Unlike conventional linear ESOs (LESOs) limited by bandwidth and phase lag, CHESO provides improved accuracy and robustness at high speeds. To further enhance performance in the FW operation, a second-order generalized integrator (SOGI) combined with a high-order ESO (HESO) framework is proposed. The SOGI suppresses noise and harmonics, while the HESO reduces phase lag and expands bandwidth. Experimental results show that these approaches reduce rotor position errors and significantly improve harmonic suppression.

Finally, to address robust control, adaptive feedforward torque compensation and an adaptive linear active disturbance rejection controller (ALADRC) are developed. The feedforward strategy enhances dynamic response and disturbance rejection, while ALADRC adjusts bandwidth in real time to cope with FW conditions. The results confirm reductions in speed error amplitudes, improved stability under parameter mismatches, and stronger robustness compared with conventional PI and LESO-based methods.

In conclusion, this thesis advances both analysis and control of high-speed PMSMs. The proposed MOR provides an efficient tool for design and evaluation, while CHESO, SOGI-HESO, and

ALADRC deliver accurate and robust sensorless control across wide speed ranges. Together, these contributions enable reliable and high-performance operation of high-speed PMSMs in critical energy and transportation applications, supporting the transition to sustainable and intelligent electrification.

Keywords: Cascade high-order extended state observer, high-speed permanent magnet synchronous motors, sensorless control, robust control, parameter mismatches.

Acknowledgements

I wish to express my sincere gratitude to all the people who have supported me throughout this long journey.

Firstly, I am deeply grateful to my supervisors, Prof. Youguang Guo, A/Prof. Gang Lei, and Prof. Jianguo Zhu, for their invaluable guidance during my research. Prof. Youguang Guo provided inspiring ideas for my topics and offered constant encouragement during difficult times. I wish to express my heartfelt appreciation to A/Prof. Gang Lei, who provided valuable advice on experimental design, research direction, and manuscript preparation. Their kindness, patience, and profound knowledge have always motivated me in my work. I am also thankful to Prof. Jianguo Zhu for his guidance, foresight, and wisdom in scientific research. Their comments, suggestions, and support were fundamental to achieving the objectives of my Ph.D. project.

Secondly, I would like to thank A/Prof. Ricardo P. Aguilera for inspiring me to explore more advanced methods in my research. I am also grateful to Mr. Brett Lowder for his technical support with prototype testing, especially for his help in ordering the torque sensor and implementing dSPACE. Thanks to Prof. Xinhua Guo for his kind help and recommendation, I can continue my further study. My appreciation is beyond expression. My sincere thanks also go to our group members, friends, and laboratory partners for their help and assistance in building the test bench and control system, particularly Yachao, Bingkuan, Wenbo, and Shuaiwen.

Moreover, I am very thankful to my friends at UTS for their friendship and support, including Yimin Liu, Wenbo Xu, Zixu Zhang, Ying Wang, Rodrigo H. Cuzmar, Ignacio Torres Herrera, Haoran Jiang, Tianling Shi, etc. Special thanks also go to my friends Jiaqing Dai, Xiaodong Wang, and Jingsheng Wang, whose concern and greetings from afar always reminded me that I was not alone. A bosom friend afar brings a distant land near.

Most importantly, I am profoundly grateful to my parents and family, who have always supported me unconditionally. Thanks to my parents for their endless love and encouragement. I am also thankful to my sisters Li and Qiannan, my brother-in-law Binbin, and my smart nephew Tinghao, for their unwavering love, support, and inspiration.

Kai Xu

February 2026

Sydney, Australia

List of Publications

Journal Publications

1. **K. Xu**, Y. Guo, G. Lei, and J. Zhu. Sensorless Control of High-Speed PMSM Based on Cascade High-Order Extended State Observer for Flywheel Energy Storage System. *IEEE Transactions on Industrial Electronics*, Early Access , DOI: 10.1109/TIE.2025.3598193.

2. **K. Xu**, Y. Guo, G. Lei, X. Sun, and J. Zhu. Electromagnetic Performance Analysis of a Bearingless Permanent Magnet Synchronous Motor by Model Order Reduction. *IEEE Transactions on Magnetics*, vol. 59, no. 11, pp. 1-5, Nov. 2023.

3. **K. Xu**, Y. Guo, G. Lei, and J. Zhu. A Review of Flywheel Energy Storage System Technologies. *Energies*, 16(18):6462, 2023.

4. **K. Xu**, Y. Guo, G. Lei, and J. Zhu. Estimation of Iron Loss in Permanent Magnet Synchronous Motors Based on Particle Swarm Optimization and a Recurrent Neural Network. *Magnetism*, 3(4):327-342, 2023.

Conference Publications

1. **K. Xu**, Y. Guo, G. Lei, L. Liu, and J. Zhu. Calculation of Iron Loss in Permanent Magnet Synchronous Motors Based on PSO-RNN. 2023 IEEE International Magnetic Conference - Short Papers (INTERMAG Short Papers), Sendai, Japan, pp. 1-2, 2023.

2. **K. Xu**, Y. Guo, G. Lei, and J. Zhu. A Data-Driven Method for Iron Loss Estimation in Bearingless Permanent Magnet Synchronous Motors. 2023 IEEE International Future Energy Electronics Conference (IFEEC), Sydney, Australia, pp. 98-102, 2023.

Under Review

1. **K. Xu**, Y. Guo, G. Lei, and J. Zhu. Improved Sensorless Control of High-Speed SPMSMs Based on SOGI High-Order Extended State Observer in the Flux-Weakening Region for Flywheel Energy Storage Systems. Submitted to *Transactions on Industrial Electronics.*

Collaborative Publications

1. Y. Zhu, **K. Xu**, B. Wan, G. Lei and J. Zhu. Kolmogorov-Arnold Network for Solving 2-D Magnetostatic Problems. *IEEE Transactions on Magnetics*, vol. 61, no. 9, pp. 1-5, Sept. 2025.

2. Q. Teng, X. Wang, and **K. Xu**, (2025), Model-Free Adaptive Super-Twisting Sliding Mode Speed Control Based on RBFNN Estimator for PMLSM Drive Systems. *IET Electr. Power Appl*, 19: e70048.

List of Figures

List of Tables

Acronyms & Abbreviations

ADRC	Active Disturbance Rejection Control
LADRC	Linear Active Disturbance Rejection Contro
ALADRC	Adaptive Linear Active Disturbance Rejection Contro
BEMF	Back Electromotive Force
BPF	Band-Pass Filter
CNC	Computer Numerical Control
CVCP	Constant-Voltage-Constant-Power
EMI	electromagnetic Interference
EV	Electric Vehicle
ESO	Extended State Observer
2S-ESO	Double-Stage ESO
ASHESO	Adaptive Switching High-Order ESO
STESO	Third-Order Super-Twisting ESO
ENOR	Enhanced Nodal-Order Reduction
EKF	Extended Kalman Filter
FLL	Frequency-Locked Loop

FLC	Fuzzy Logic Controller
FEA	Finite Element Analysis
FEM	Finite Element Method
FESS	Flywheel Energy Storage System
LESO	Linear Extended State Observer
HESO	High-Order Extended State Observer
CHESO	Cascade High-Order Extended State Observer
LPF	Low-Pass Filter
LSEF	Linear State Error Feedback
LTI	linear Time-Invariant
FW	Flux-Weakening
FOC	Field-Oriented Control
ILC	Iterative Learning Controller
MOR	Model Order Reduction
MTPA	Maximum Torque Per Ampere
MTPV	Maximum Torque Per Volt
MRAS	Model Reference Adaptive Syste
PM	Permanent Magnet
PMSM	Permanent Magnet Synchronous Motor
IPMSM	interior PMSM
BPMSM	Bearingless PMSM
SPMSM	Surface-Mounted PMSM

HSPMSM High-Speed PMSM

POD Proper Orthogonal Decomposition

PLL Phase-Locked Loop

QPLL Quadrature PLL

PTC Predictive Torque Control

SOGI Second-Order Generalized Integrator

SVD Singular Value Decomposition

SMO Sliding Mode Observer

THD Total Harmonic Distortion

TD Tracking Differentiator

Nomenclature

	General Notations
$(\hat{\ })$	Estimated value of a variable
$(\dot{\ })$	Differential operator
A	Magnetic vector potential
B	Damping factor of PMSM
B_r	Remanent flux density of PM
c_1	The adaptation gain of ALADRC
e_α, e_β	Equivalent BEMF in the α, β-frame
e_{11},e_{12},e_{13}	State error of first level CHESO
e_{21},e_{22},e_{23}	State error of second level CHESO
e_f, e_h	The fundamental and $(1 \pm 6k)$-order harmonics of the BEMFs
E_1, $E_{6k\pm1}$	The BEMFs amplitude of fundamental and $(1 \pm 6k)$-order harmonics
F_x, F_y	Levitation forces along the $x-$ and $y-$axis of BPMSM
i_q,i_d	The $q-$ and $d-$axis currents
i_α,i_β	Stator current in the α, β-frame
i_q^*	The reference q-axis currentc
$i_{\alpha f}$, $i_{\alpha h}$	The fundamental and $(1 \pm 6k)$-order harmonics of i_α
$i_{\beta f}$, $i_{\beta h}$	The fundamental and $(1 \pm 6k)$-order harmonics of i_β
I_L	Levitation winding current of BPMSM
I_{Tp}	Equivalent current that consists of the torque winding current and PM equivalent current
J	Moment of inertia of PMSM
J_0	Applied density current source

k_s	The gain coefficient of the SOGI
K_t	The torque constant of PMSM
K_p, K_i	Gains of PI controller
l_1, l_2	Gains of the LESO
L_s	Inductance of SPMSM
p_n	Pole pairs of PMSM
R_s	Stator resistance of PMSM
T_e,T_L	Electromagnetic torque and the load torque of PMSM
u_α, u_β	Stator voltage in the α, β-frame
u_d, u_q, i_d, i_q	The voltages and currents in the $dq-$frame
$U_{s,\max}$,$I_{s,\max}$	The the voltage limit and the current limit of PMSM
U_{dc}	DC bus voltage
ω_e,ω_m	Rotor electrical angular velocity and the mechanical angular velocity
ω'_c	The adaptive bandwidth of ALADRC
ω_{cmin}, ω_{cmax}	The minimum and maximum observer bandwidths in the adaptive controller
ω_m^*	The reference speed value
ψ_f	The PM flux linkage of PMSM
θ_e	Rotor position angle of PMSM
θ_{e1}, $\theta_{e(6k\pm1)}$	The initial estimated rotor position of fundamental and $(1 \pm 6k)$-order harmonics
θ_T, θ_L	Electrical angles of the levitation winding current and the torque winding current of BPMSM
β_{11}, β_{12}, β_{13}	Gains of first level CHESO
β_{21}, β_{22}, β_{23}	Gains of second level CHESO
β_{r1}, β_{r2}	The observer gains of LESO

Contents

Chapter 1

Introduction

1.1 Background

In recent years, permanent magnet synchronous motors (PMSMs) have become one of the most important classes of electrical machines, offering a combination of high efficiency, compact design, and superior dynamic performance compared with induction or synchronous machines [1, 2]. Their ability to achieve high power density with reduced energy losses has enabled their integration into diverse application areas, ranging from electric vehicles (EVs) [3] and high-speed trains [4] to precision industrial automation [5, 6] and renewable energy storage systems [7, 8]. As the global economy transitions toward sustainability and electrification, the demand for reliable and high-performance PMSM drives is rapidly increasing.

The electrification of transportation is one of the most significant global engineering challenges, driven by sustainability targets and strong policy support. PMSMs are widely used in EVs because of their high efficiency, compact size, and ability to deliver high torque over wide speed ranges. As shown in Fig. 1.1, leading manufacturers such as Tesla, BYD, and Huawei have adopted advanced PMSMs and high-speed PMSMs (HSPMSMs) drive systems in their platforms to balance efficiency with fast acceleration and extended driving range [9]. In addition to EVs, PMSMs are increasingly applied in industrial automation and precision machinery, including high-speed computer numerical control (CNC) machines. These applications demand motors that combine high precision, reliability, and energy savings.

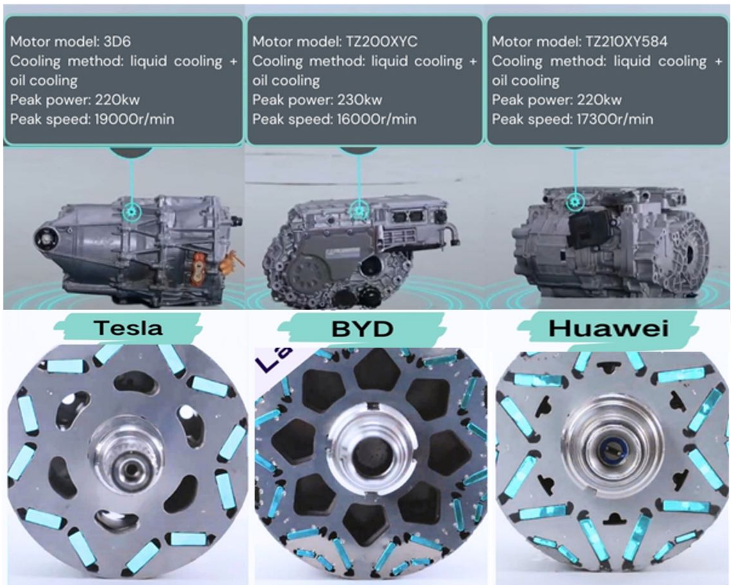

Fig. 1.1: PMSMs application in electric vehicles [9].

The demands for environmental protection and the promotion of low-carbon development have led to a gradual increase in the proportion of renewable energy sources in the power grid, primarily wind and solar. Wind and solar energy have become the primary research subjects because the energy system has been more actively targeting these two energy sources. In Fig.1.2, the statistics show that global power generation from wind and solar sources has grown from 1,086 TWh in 2015 to 4,632 TWh in 2024 [10]. The installed annual capacity for wind and solar energy is shown in Fig.1.3. The installed wind and solar capacity increased from 643 GW in 2015 to 2,998 GW in 2024, which is equivalent to an average annual growth rate of 36% [10]. In the next ten years, the anticipated installation capacity of wind and solar energy will increase at an average annual rate of 14% and 18%, respectively.

However, their inherent intermittency and variability introduce challenges to grid stability, including frequency fluctuations, voltage instability, and mismatched supply and demand [11–13]. Flywheel energy storage systems (FESS), powered by HSPMSMs, provide an attractive solution for grid frequency regulation and short-term energy buffering [14]. FESSs offer high efficiency, long cycle life, and the ability to deliver rapid power injections or absorptions, making them well-suited for stabilizing grids with high renewable penetration[15–17]. Megawatt-scale FESS installations have already been deployed to support frequency regulation in power systems [18–20].

HSPMSMs are also increasingly adopted in traction systems for high-speed rail, where weight

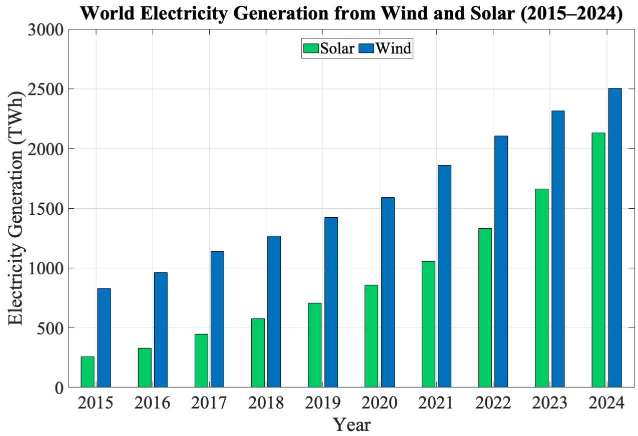

Fig. 1.2: Wind and solar electricity generation in the past decade.

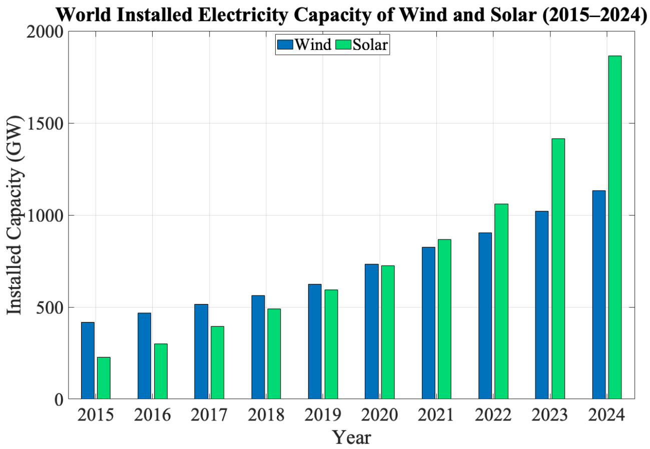

Fig. 1.3: Wind and solar installed capacity in the past decade.

reduction, energy efficiency, and reliability are paramount. For example, the CR450 high-speed train prototype, introduced in 2025, operates at a speed class of 400 km/h and utilizes PMSM-based traction motors [21]. Compared to conventional asynchronous traction motors, such as the YQ-365, PMSM traction motors achieve a 35% reduction in weight, an increase in efficiency by more than 3%, and an energy-saving effect exceeding 10%. These benefits translate into higher passenger capacity, reduced operating costs, and improved sustainability of rail transport systems. However, the operating conditions of high-speed trains impose severe technical challenges. The motors must withstand sudden load changes caused by acceleration, braking, or gradients, all of which introduce large disturbances. Moreover, inverter nonlinearities such as voltage ripple and harmonic distortion degrade motor performance and complicate control accuracy.

In summary, PMSMs, as well as HSPMSMs, face significant challenges despite their efficiency and

Fig. 1.4: Future of High-Speed Rail: CR450 EMU Prototype [21].

compactness. In EVs and industrial automation, PMSMs must endure frequent load transients, wide speed variations, and long operating hours in harsh environments, which impose strict reliability and robustness demands. In renewable energy systems, their integration is complicated by the intermittency and variability of wind and solar power, which introduce issues such as frequency fluctuations, voltage instability, and mismatched supply and demand. FESSs, although promising for grid stability, require motors capable of operating at extreme rotational speeds, which leads to high iron and copper losses, severe thermal stress, and elevated mechanical demands on rotor designs. Therefore, their deployment still faces three major challenges:

1. The first challenge lies in reliability and efficiency, as accurate evaluation of electromagnetic performance is essential for control and optimization. While finite element analysis (FEA) offers high accuracy, it is computationally expensive, and conventional analytical models lack precision for complex topologies.

2. The second challenge is sensorless accuracy at high speeds and in flux-weakening (FW) regions. Since mechanical sensors are often impractical in high-speed environments, improving estimation accuracy is critical. Conventional observers suffer from bandwidth limits, phase lag, and noise sensitivity, while inverter nonlinearities and harmonics further degrade estimation.

3. The third challenge is robustness, as PMSMs must tolerate disturbances, parameter variations, and nonlinear effects. Existing control strategies are insufficient for fast dynamics in high-speed conditions, resulting in limited disturbance rejection and transient response. Robust solutions must therefore combine adaptive bandwidth adjustment with strong noise suppression to ensure stable and reliable operation.

1.2 Objectives

This thesis aims to enhance the efficiency, accuracy, and robustness of PMSM systems, with a particular focus on high-speed surface-mounted PMSMs (SPMSMs). The specific objectives are as follows:

1. Developing an advanced fundamental analysis method by proposing a proper orthogonal decomposition (POD)-based model order reduction (MOR) for electromagnetic performance evaluation of bearingless PMSMs (BPMSMs), thereby reducing computation time while maintaining high accuracy under complex flux and frequency conditions. These fast and accurate models are also essential for robust control design, as they provide the basis for dynamic analysis under demanding operating conditions.

2. Designing improved sensorless control strategies through a cascade high-order extended state observer (CHESO) for precise back electromotive force (BEMF) and disturbance estimation in high-speed, and a second-order generalized integrator (SOGI) high-order extended state observer (HESO)-based framework to suppress noise, attenuate harmonics, and extend estimation bandwidth in the FW region.

3. Developing robust control schemes that integrate adaptive feedforward torque compensation with adaptive linear active disturbance rejection control (ALADRC), aiming to enhance torque and speed dynamics, improve disturbance rejection, and maintain stability under parameter mismatches and load variations.

1.3 Thesis Structure

This thesis investigates the modeling, sensorless estimation, and robust control of PMSMs, with a focus on high-speed SPMSMs. It addresses the three major challenges of reliability and efficiency, sensorless accuracy, and robustness under disturbances and parameter variations, forming a complete technical framework for advanced PMSM applications. The organization of this research is as follows:

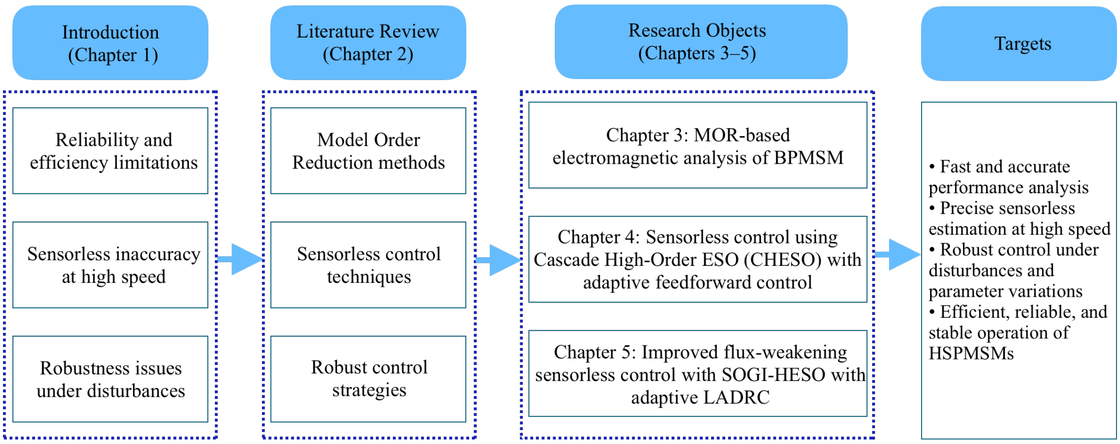

Fig. 1.5: The structure of the thesis.

Chapter 2 reviews the state-of-the-art in electromagnetic performance analysis and control of BPMSM and PMSMs. Existing approaches for MOR modeling are analyzed, highlighting the trade-off between computational efficiency and accuracy in conventional FEA. The review also examines conventional sensorless control methods, including linear extended state observers (LESOs), and their limitations in high-speed and FW conditions due to bandwidth and noise sensitivity. Furthermore, the robustness of conventional control strategies such as active disturbance rejection control (ADRC) and linear ADRC (LADRC) is discussed, showing their inadequacy for fast dynamics and parameter mismatches in HSPMSMs. These insights identify clear research gaps that motivate the contributions of this thesis.

In Chapter 3, an electromagnetic performance analysis method for fast dynamic simulation of a BPMSM based on MOR is presented. The electromagnetic characteristics and dynamic behavior model of the rotating machine are constructed by using the MOR based on POD. First, the $q-$ and $d-$axis currents and rotor angle of the motor are scanned to construct the magnetic field distribution snapshot matrix. Then, the singular value decomposition (SVD) of the snapshot matrix is used to calculate the basis vectors. Finally, the order of the system is reduced by selecting an appropriate truncation order of the basis vectors. Compared with the finite element method (FEM), the calculation time of MOR for the BPMSM is significantly reduced. At the same time, it can provide accurate results of motor magnetic field distribution, electromagnetic force, levitation force, and dynamic response calculations, and achieve fast and accurate state feedback. Through analysis and comparison, the results of the proposed method match well with the FEM simulations.

In Chapter 4, a CHESO is proposed for enhanced position estimation and speed control of HSPMSMs. The effectiveness of the CHESO in extending the observation bandwidth and improving control accuracy is demonstrated. In the proposed two-level CHESO architecture, the BEMF is accurately estimated at the first level, while position, load torque, and uncertain disturbances are concurrently estimated at the second level. Subsequently, the estimated disturbances and load torque are employed in an adaptive feedforward control strategy to enhance the dynamic performance and anti-disturbance capability of the high-speed SPMSMs control system.

In Chapter 5, a SOGI-HESO is proposed, which effectively attenuates current harmonics and measurement noise. In the proposed scheme, the SOGI enhances the input signal quality to the HESO, resulting in improved BEMF estimation accuracy and noise immunity. A phase-locked loop (PLL) is then employed to extract rotor position from the estimated BEMF. Finally, an ALADRC strategy is implemented in the speed loop to improve dynamic response and disturbance rejection capability in the FW region, ensuring robust performance under high-speed operating conditions. Finally, Chapter 6 concludes this thesis and provides suggestions for future research directions.

Therefore, motivated by the challenges identified in reliability and efficiency, sensorless accuracy at high speed, and robustness under disturbances, this thesis develops a coherent framework that integrates advanced modelling and control techniques for high-speed SPMSMs drive systems. The literature review in Chapter 2 clarifies the limitations of existing electromagnetic modelling, sensorless estimation, and robust control approaches, thereby defining the research gaps addressed in this work. These gaps are first tackled through a MOR methodology for a BPMSM in Chapter 3, which establishes efficient and accurate electromagnetic modelling foundations. Building on this modelling framework, the subsequent Chapters 4 and 5 focus on high-speed SPMSMs, where enhanced sensorless estimation and robust control strategies are developed and experimentally validated.

Chapter 2

Literature Review

2.1 Introduction

This chapter reviews the existing studies related to BPMSMs and high-speed PMSMs, focusing on modeling, sensorless estimation, and robust control. The review is organised around the three challenges identified in Chapter 1: (i) reliable and efficient performance evaluation, (ii) high-speed sensorless accuracy, including flux-weakening operation, and (iii) robustness under disturbances and parameter variations. Each subsection concludes by summarising the key limitation in existing work and explaining how it motivates the methods developed in subsequent chapters.

The discussion begins with electromagnetic performance analysis of BPMSMs, where MOR techniques are introduced to overcome the computational burden of FEA while maintaining high accuracy. These reduced-order models provide the foundation for efficient performance evaluation and control development in high-speed applications.

Then, this chapter reviews the evolution of sensorless and robust control strategies for HSPMSMs. Conventional sensorless methods and extended state observer (ESO)-based approaches are compared in terms of estimation accuracy, bandwidth, and noise robustness, especially under high-speed and FW conditions. Further, studies on FW control and ADRCs are analyzed to assess their capabilities in improving torque, speed response, and system stability under parameter mismatches and inverter nonlinearities. The literature review concludes by identifying the key research gaps, forming the basis for the methods developed in subsequent chapters.

2.2 Electromagnetic Performance Analysis of Bearingless PMSM

At present, in the electromagnetic analysis and design of electric machines, the FEM is usually used to calculate the electromagnetic field. When performing finite element analysis for electrical machines, the solution of large systems needs a large storage space and becomes time-consuming. Due to the high computational cost, dynamic finite element analysis is challenging to apply and implement for fast dynamic simulation and control systems of electric machines.

2.2.1 Model Order Reduction Methods

MOR techniques aim to reduce the computational complexity of large-scale dynamical systems while preserving their dominant physical characteristics. These methods are widely used in mechanics, fluid dynamics, and electromagnetics to accelerate simulation and control design. For PMSM analysis, MOR provides an efficient alternative to time-consuming FEA, enabling faster evaluation of electromagnetic performance and facilitating the development of real-time control [22]. Several MOR approaches have been proposed, among which the center manifold, Lyapunov–Schmidt, Galerkin, modal synthesis, and POD methods are the most representative [23–29].

The center manifold method simplifies nonlinear systems by exploiting the invariance of low-dimensional manifolds near equilibrium points [24]. The method projects the full-order model onto the manifold that captures the system's essential local dynamics, eliminating fast-decaying modes while retaining the slow ones. Because it is derived from the system's Jacobian matrix, the technique provides accurate local behavior around steady states and has been widely applied in nonlinear vibration and stability studies [30]. However, its applicability to high-dimensional electromagnetic systems is limited, since deriving explicit manifold expressions for large parameter spaces is mathematically demanding.

The Lyapunov–Schmidt method follows a similar reduction principle but reformulates the equilibrium equations as operator equations, decomposing the solution space into critical and complementary subspaces [25, 31]. It is particularly effective for bifurcation and qualitative analyses where the primary interest lies in identifying stability transitions. Although this approach offers rigorous theoretical insight, it is unsuitable for real-time or transient electromagnetic simulations because it does not provide a straightforward reduced-order numerical model for time-domain computation.

The Galerkin method is one of the most established MOR techniques in engineering analysis. It constructs a reduced-order model by projecting the governing partial differential equations onto a set of chosen basis functions, typically derived from the system's eigenmodes or polynomial approximations [27, 32, 33]. The accuracy of the Galerkin method strongly depends on the completeness and orthogonality of the selected basis. For electromagnetic field problems, the Galerkin approach can yield high fidelity but often requires problem-specific basis functions, leading to limited generality and relatively high pre-processing effort.

The modal synthesis method divides the global system into several substructures or modal subspaces and then couples their individual dynamic characteristics into a global reduced model [28, 34, 35]. This method is particularly useful for large, weakly coupled systems, as it allows parallel computation and preserves physical interpretability. Nevertheless, modal synthesis may suffer from reduced accuracy when nonlinear coupling effects dominate, and determining appropriate interface modes remains challenging for systems with complex electromagnetic interactions.

Among the reviewed approaches, the POD method has gained increasing attention for its data-driven adaptability and computational efficiency. POD extracts dominant spatial or temporal modes directly from snapshot data obtained via high-fidelity simulations or experiments, using SVD to identify the most energetic modes [29, 36, 37]. The resulting reduced basis captures the principal dynamics of the system with minimal loss of accuracy. Compared with analytical or mode-based approaches, POD is straightforward to implement, independent of problem geometry, and easily combined with numerical solvers or finite-element codes.

In electromagnetic applications, POD-based MOR can accurately reproduce flux-density distributions, torque ripple, and dynamic responses while reducing computational time by several orders of magnitude. This makes it especially suitable for iterative PMSM design optimization, real-time control development, and high-speed PMSMs performance analysis. A summary of the model order reduction methods is listed in Table 2.1.

Table 2.1: Summary of model order reduction methods

Method	Main principle	Advantages	Limitations	Typical applications
Center manifold method	Reduces nonlinear systems near equilibrium by retaining slow modes and eliminating fast-decaying ones through manifold invariance.	Provides rigorous insight into local nonlinear dynamics and stability behavior.	Applicable only near equilibrium; difficult to apply to high-dimensional or time-varying systems.	Nonlinear vibration, bifurcation, and stability analysis of small-scale systems.
Lyapunov–Schmidt method	Decomposes equilibrium equations into critical and complementary subspaces for bifurcation and stability analysis.	Offers strong theoretical foundation for analyzing qualitative behavior and stability transitions.	Not suitable for large-scale numerical simulation; limited to local static analysis.	Analytical studies of nonlinear bifurcations and steady-state stability.
Galerkin method	Projects governing equations onto a reduced subspace using predefined basis functions.	Well-established, physically interpretable, and accurate for problems with well-defined modes.	Accuracy depends on basis selection; limited generality for complex geometries.	Structural dynamics, fluid flow, and electromagnetic field modeling.
Modal synthesis method	Combines modal substructures or components into a global reduced model through dynamic coupling.	Enables parallel computation, modular modeling, and clear physical interpretation.	Accuracy degrades for strong nonlinear couplings; interface mode selection is complex.	Large structural systems, coupled multi-domain dynamics.
Proper Orthogonal Decomposition	Extracts dominant modes directly from data snapshots via singular value decomposition.	Data-driven, efficient, and geometry-independent; achieves high accuracy with minimal modes.	Requires high-quality data; reduced model may lose accuracy for highly nonlinear dynamics.	Electromagnetic field analysis, real-time PMSM control, design optimization.

2.2.2 Model Order Reduction for Electromagnetic Analysis

The field of applied mathematics that focuses on MOR for partial differential equations is currently a vibrant area of research [38]. Projection-based MOR methods have been applied to reduce computational complexity significantly [39, 40]. The MOR has an extensive range of applicability and has been successfully used in the research of signal identification, turbulence characteristics, and model identification [41, 42]. Currently, this method is mainly used in fluid mechanics research, particularly in analyzing the vibration behavior of airframes affected by airflow in the aerospace industry [43–45].

In recent years, MOR techniques have been increasingly applied in the field of computational electromagnetics to address the challenges of high computational costs associated with large-scale finite element models. MOR enables the approximation of complex electromagnetic systems with lower-dimensional models that retain essential physical behavior, allowing for faster simulation and design optimization. The applications of MOR have expanded across multiple domains, including the calculation of magnetic field distributions in transformers and rotating machines, the analysis of eddy current problems, the optimization of radio-frequency antennas, the modeling of hysteresis in magnetic materials, and the management of heat conduction in semiconductor equipment [46–50]. These advancements demonstrate that MOR has become an essential tool for efficiently analyzing both linear and nonlinear electromagnetic systems while maintaining acceptable accuracy.

In the field of electromagnetic devices, the broadband enhanced nodal-order reduction (ENOR) methodology demonstrates the effectiveness of model order reduction in handling large-scale three-dimensional transient field problems. By significantly decreasing computational time while maintaining high accuracy, ENOR validates the potential of reduced-order modeling for complex multiphysics systems. This approach highlights the feasibility of applying MOR techniques to electromagnetic and thermal analyses of power electronic devices [46].

In piezoelectric actuators applications, the study demonstrates the use of model reduction to optimize online compensation of hysteresis and creep in piezoelectric actuators [47]. By identifying model parameters directly from experimental data, the approach achieves an effective balance between modeling accuracy and computational efficiency. The results confirm that reduced-order models can meet circuit performance requirements while enabling real-time compensation in smart actuator systems.

For magnetoquasi-static field problems, the combination of the POD and Arnoldi-based Krylov methods demonstrates an efficient approach for reducing finite-element models of magnetoquasi-static problems [48], achieving a good balance between computational speed and accuracy. Meanwhile, the adaptive quadratic–bilinear model-order reduction algorithm extends MOR capabilities to nonlinear eddy current problems by incorporating error control and directly handling system nonlinearities [49]. Together, these methods highlight the growing effectiveness of MOR in improving the efficiency and precision of complex electromagnetic simulations.

Furthermore, in the area of multiphysics modeling, the MOR was applied to derive a compact yet accurate thermal model of SiC MOSFET power modules using a Krylov subspace approach [50]. The reduced-order model maintains the fidelity of the original FEA while significantly decreasing computational cost. This demonstrates the effectiveness of MOR in enabling efficient and precise thermal analysis for high-power electronic devices.

2.2.3 Proper Orthogonal Decomposition Based Model Order Reduction

Although the symmetrical geometry of electrical machines can often be utilized to simplify analytical models and reduce computational time, real-world deviations often disrupt this symmetry, including manufacturing tolerances, material nonuniformity, and structural asymmetry. These factors necessitate solving the full-scale model, resulting in significant computational demands. To overcome this limitation, recent studies have extended MOR to rotating electrical machines, where the magnetic field distribution is inherently more complex due to the influence of rotor motion and spatial harmonics. The development of MOR techniques based on POD has shown considerable promise in this area.

POD-based MOR techniques extract dominant spatial or temporal modes directly from high-fidelity simulation data using SVD. This data-driven approach allows reduced models to accurately represent dynamic field variations caused by rotor position changes while achieving a dramatic reduction in computational cost. A simplified MOR technique based on POD is developed for the fast dynamic simulation of electric motors. By combining singular value decomposition and dynamic mode decomposition, the method efficiently interpolates magnetic field distributions across varying currents and rotor positions [40]. This approach enables rapid and accurate electromagnetic analysis, greatly reducing computation time for motor performance evaluation.

The POD combined with discrete empirical interpolation methods provides an efficient means to estimate electrical machine behavior, enabling accurate computation of key quantities such as torque and iron losses with reduced computational effort [51]. In linear finite element models of induction machines, POD-based MOR effectively reproduces machine performance over the full operating range, significantly accelerating simulations while maintaining fidelity to full-order results [52]. Furthermore, the integration of POD with a posteriori error control facilitates robust optimization under parameter uncertainties, achieving reliable and fast design optimization of permanent magnet synchronous machines governed by nonlinear partial differential equations[53].

Although the FEM is capable of accurately computing the power loss and torque ripple of electrical machines, it suffers from the disadvantage of requiring extensive computational resources when real-time data from electrical machines is needed [54]. Okamoto et al. [55] utilized a simplified POD-based MOR method to compute the loss and torque for electrical machines, achieving a computation error of less than 0.6%. A block MOR approach was introduced for analyzing the torque and loss of electrical machines, which demonstrates a significantly greater speedup ratio compared to conventional FEM techniques [56]. By taking into account the rotation of the rotor, the electromagnetic field was solved using the POD-based MOR method, and the computational efficiency and accuracy of the approach were evaluated [57, 58].

2.2.4 Model Order Reduction of Bearingless PMSM

Utilizing MOR for electrical machines analysis can significantly reduce computational costs compared to FEM, and the POD-based MOR is proven to be an effective method for magnetic field analysis. However, current research on MOR analysis for electrical machines is primarily focused on the electromagnetic field and torque computation, with very few studies on the dynamic behavior of electrical machines, which is essential for motor control performance.

BPMSMs have broad application prospects in high-speed, high-precision equipment, flywheel energy storage systems, and centrifugal compressors [59, 60]. Bearingless PMSMs differ from traditional electrical machines in that they have additional suspension force windings located within the stator. The two sets of windings, one for torque and one for suspension force, are used to generate torque and suspension force, respectively, allowing for simultaneous motor rotation and suspension. This type of motor not only reduces axial volume and weight but also surpasses the limitations of ultrahigh speed and maximum power, and offers advantages such as no lubrication, no wear, and no mechanical noise of magnetic bearings [61, 62]. By developing the MOR technique for BPMSMs, it is possible to calculate the magnetic field distribution, electromagnetic torque, and radial levitation force of the motor in real-time quickly and accurately. This results in improved torque control and better levitation operation effects.

To conclusion, the literature shows that while POD-based MOR can greatly accelerate electromagnetic simulation, existing work on electrical machines is still predominantly focused on field or torque prediction, with limited emphasis on dynamic behaviour modelling suitable for control development, especially for BPMSMs with coupled torque and suspension-force windings. To address this gap, Chapter 3 develops a POD-based MOR framework for BPMSMs that enables fast yet accurate dynamic performance evaluation, providing a modelling foundation for the high-speed sensorless estimation and robust control designs introduced in Chapters 4 and 5.

2.3 Sensorless Control of High-Speed PMSMs

2.3.1 Conventional Sensorless Control Methods

The PMSM drive system mainly realizes high-performance vector control by installing position sensors, which increases the system cost and installation complexity [63], but in some special scenarios, the installation of sensors is restricted by the space conditions and fixing methods of the motor. Moreover, the position or speed sensor has become one of the main sources of fault in the drive system, and the sensor failure will seriously affect the performance of the drive system and even cause damage to the drive system [64]. The sensorless control strategy of PMSMs can not only reduce the system cost but also reduce the risk caused by sensor failure, which has broad application prospects in many fields [65, 66].

In PMSM sensorless control, rotor position is inferred by integrating motor voltage and current signals with control theory and signal processing techniques. This process primarily encompasses two methodological approaches. The first is a fundamental-frequency model-based method that employs the motor's BEMF or flux-linkage model to estimate the rotor position via an observer. The second approach utilizes a high-frequency model, wherein high-frequency voltage injection is used to track the motor's salient pole, thereby facilitating rotor position detection [67–69].

High-frequency signal injection methods are primarily employed in zero- and low-speed operational regions, leveraging the anisotropic characteristics of the rotor to facilitate position estimation [70]. Conversely, fundamental-frequency model-based methods encounter limitations at low speeds due to the diminished magnitude and reduced accuracy of the BEMF [63], thus demonstrating superior performance in medium- and high-speed regions. Presently, observers incorporating advanced control theories, including the extended Kalman filter (EKF) [71], model reference adaptive system (MRAS) [72], sliding mode observer (SMO) [65], and ESO, are widely applied in sensorless techniques to improve rotor position estimation accuracy and system performance. A comparison of observer-based sensorless control methods is listed in Table 2.2.

Table 2.2: Comparison of observer-based sensorless control methods for PMSMs.

Method	Main principle	Advantages	Limitations	Applications	Accuracy	Computational Complexity	Noise sensitivity	Parameter robustness
EKF	Statistical estimation using recursive state-space model and noise covariance.	High estimation accuracy; adaptive to noise and variations.	Complex tuning; high computation load.	High-speed, noise-sensitive drives.	★★★ (High)	★★★ (High)	★ (Low)	★★ (Medium)
MRAS	Adaptive model matching between reference and adjustable models.	Simple structure; easy to implement; low cost.	Poor low-speed accuracy; parameter dependent.	Medium- or high-speed industrial drives.	★★ (Medium)	★ (Low)	★★ (Medium)	★ (Low)
SMO	Nonlinear switching observer with discontinuous feedback law.	Strong robustness; fast dynamic response.	Chattering; phase delay from filtering.	Variable-load or uncertain drives.	★★ (Medium)	★★ (Medium)	★★ (Medium)	★★★ (High)
ESO	Augmented observer estimating states and total disturbances.	Excellent disturbance rejection; simple design.	Sensitive to bandwidth tuning; noise amplification at high gains.	High-speed, robust control.	★★ (Medium)	★★ (Medium)	★★ (Medium)	★★★ (High)

2.3.2 High-Speed SPMSM Sensorless Control Methods

For sensorless control of high-speed PMSMs, various strategies have been proposed to improve estimation accuracy and control performance. Prediction and adaptive compensation strategies based on SMOs have been developed to mitigate position estimation errors.

A prediction-based full-speed-range sensorless control strategy is proposed to achieve precise high-speed operation of PMSMs [73]. By generating a position-related error current and correlating predicted and measured currents, the method ensures accurate rotor position estimation across the entire speed range. It effectively reduces startup fluctuations and enhances anti-interference capability without additional sensors, ensuring smooth high-speed performance.

A high-precision sensorless control approach for high-speed PMSMs integrates a continuous variable boundary-layer SMO with position error feedforward compensation [74]. This combination suppresses chattering and compensates for inverter nonlinearities and system delays, maintaining stable and accurate control at high rotational speeds.

An adaptive compensation method is proposed for high-speed SPMSM sensorless drives to enhance BEMF-based position estimation accuracy[75]. By combining an SMO and a PLL with adaptive synchronous frequency filters, the method effectively suppresses harmonic errors in rotor position estimation.

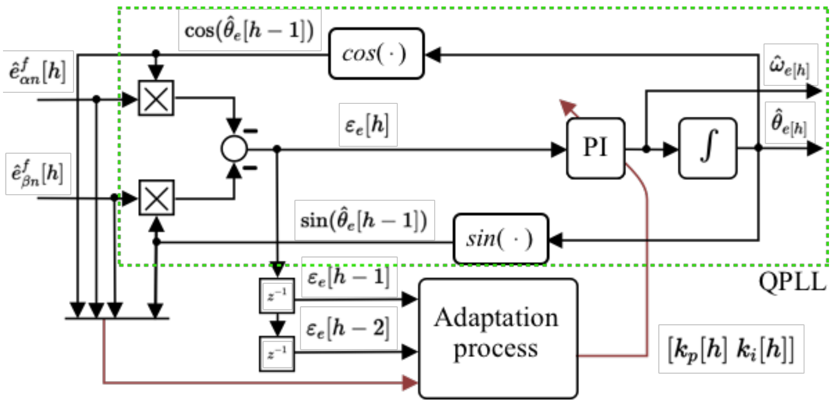

Fig. 2.1: Block diagram of the designed adaptive quadrature PLL [76].

Recent advances in high-speed PMSM sensorless control have focused on improving dynamic response and estimation accuracy. An adaptive quadrature PLL enables real-time bandwidth adjustment, reducing phase delay and achieving 25% faster acceleration with less than 3° steady-state error at 100 kr/min [76], as shown in Fig. 2.1. Meanwhile, an HESO-based approach integrates PWM effects and delay compensation for precise BEMF estimation, eliminating the need for PI current control[77].

Furthermore, recent studies on parameter identification for high-speed PMSM sensorless control have emphasized improving accuracy and robustness under inverter nonlinearities and dynamic conditions. A PWM current ripple-based inductance identification method utilizes inherent inverter ripple for online estimation without injecting extra signals, effectively eliminating position estimation errors during operation [78]. Similarly, a first-order model with least-squares identification enhances robustness by decoupling inductance estimation from flux, position, and dead-time errors, ensuring stable high-speed performance [79]. Moreover, a multifrequency disturbance injection technique enables simultaneous resistance and inductance identification, modeling dead-time effects as equivalent resistances to improve accuracy[80]. Verified up to 60,000 r/min, these methods collectively advance reliable, high-speed PMSM sensorless drives with precise parameter adaptation and improved real-time control stability.

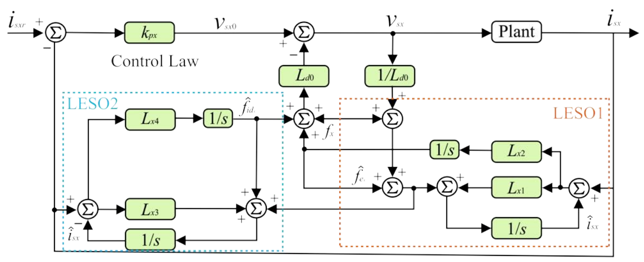

Fig. 2.2: Block diagram of the plant controlled by the enhanced LADRC scheme [81].

2.3.3 Sensorless Control Based on Extended State Observer

Recent advancements in ESO-based sensorless control have focused on improving robustness, accuracy, and dynamic performance in PMSM and SPMSM drives. In Fig. 2.2, an enhanced LADRC integrates two LESOs, one for BEMF estimation used in rotor position detection and another for compensating internal disturbances, which improves current regulation and position estimation without phase delay and chattering[81]. A flux-linkage observer with an ESO-based compensation strategy effectively removes DC offset and drift errors, ensuring accurate rotor position tracking in both steady and transient states [82]. In addition, an adaptive ESO combined with an improved quadrature PLL (QPLL) achieves online bandwidth tuning and dynamic compensation for torque transients, enhancing robustness under wide speed and heavy load conditions [83].

Currently, LESO is predominantly favored over the nonlinear ESO, primarily due to its simplified parameter tuning process and straightforward stability analysis. In [84], a frequency-adaptive LESO was introduced to effectively eliminate steady-state position estimation errors without requiring additional phase compensation, demonstrating superior harmonic attenuation compared to the conventional LESO. To reveal the connection between bandwidth and position, and speed tracking performance, the guidelines of bandwidth determination of the third-LESO were presented in [85].

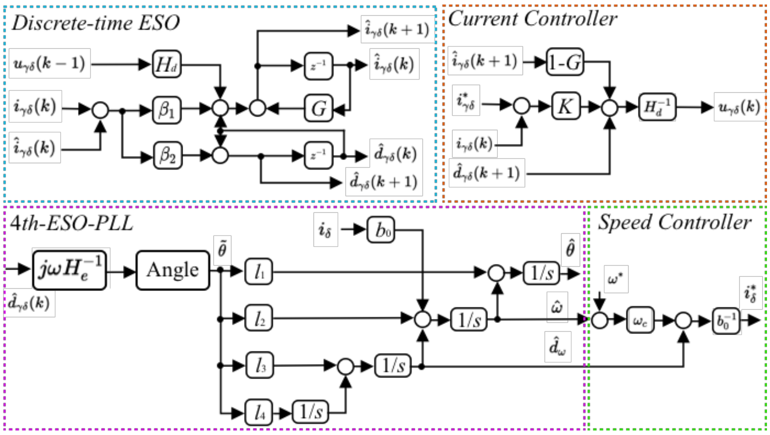

Fig. 2.3: System block with the proposed sensorless control scheme [77].

In [85], various ESO-based approaches have been successfully applied to rotor position and speed estimation in low- and medium-speed PMSM applications. Although an ESO-based method for HSPMSM was proposed in [77], which primarily focuses on optimizing PLL performance using a high-order ESO, while the BEMF observer remains a second-order LESO, as shown in Fig. 2.3.

These approaches significantly advance high-performance and reliable sensorless control for PMSM systems, maintaining stability and precision during rapid acceleration and load disturbances. Currently, there is limited research addressing rotor position estimation and disturbance rejection using HESO for sensorless control of HSPMSMs.

Therefore, the reviewed high-speed sensorless methods improve estimation accuracy but still face a fundamental limitation in balancing estimation bandwidth and noise/harmonic sensitivity, particularly when inverter non-idealities distort the BEMF. In addition, there remains limited work on using high-order ESO structures to simultaneously estimate BEMF and lumped disturbances for high-speed PMSMs. These gaps motivate Chapter 4, which proposes a cascade high-order ESO (CHESO) architecture to improve BEMF and disturbance estimation and to support accurate position/speed estimation and robust speed regulation at high speed.

2.4 Sensorless Control of High-Speed SPMSM in the Flux-Weakening

2.4.1 High-Speed PMSM Control in the Flux-Weakening Region

FW control is essential for extending the operating speed range of PMSMs, particularly in high-speed applications such as EVs, FESS, and industrial drives. In the FW region, the voltage constraint requires coordinated control of the i_d and i_q currents rather than independent regulation as in the base-speed region. To address this coupling, recent studies have analyzed and optimized current control strategies and system stability to achieve high efficiency and torque capability under voltage and current limits.

Further enhancements have been achieved through voltage feedback-based FW strategies. A method utilizing $q-$axis voltage feedback simplifies the nonlinear FW loop into a linear model with adaptive gain tuning and feedforward decoupling, reducing voltage deviation by approximately 45% and improving robustness against load disturbances [86]. To mitigate current harmonics at high speeds, an active damping-based FW control with voltage angle regulation introduces a $d-$axis current compensation mechanism, improving harmonic suppression and enhancing control adaptability under varying load and speed conditions [87].

In addition, several works have focused on integrating maximum torque per volt (MTPV) strategies within FW control to maximize the torque output under voltage and power constraints. By introducing a unified MTPV-FW algorithm, these methods calculate optimal i_d and i_q current references to minimize total current magnitude while respecting system limits. Such unified algorithms eliminate the need for switching between FW and MTPV modes, enabling smooth operation from standstill to maximum speed and expanding the achievable maximum speed region [88, 89].

Overall, research on high-speed PMSM control in the FW region demonstrates continuous progress toward higher accuracy, better dynamic response, and enhanced robustness. Through coupling current optimization, adaptive voltage feedback, active damping, and integrated MTPV-FW strategies, recent developments have significantly improved the stability and efficiency of high-speed PMSM drives across wide-speed ranges, providing a strong foundation for advanced sensorless and robust control designs.

2.4.2 Sensorless Control in the Flux-Weakening Region

For high-speed SPMSMs operating in the FW region, achieving accurate sensorless control becomes increasingly challenging. As the speed rises, inverter nonlinearities and other non-ideal effects introduce current harmonics that compromise the accuracy of BEMF estimation, thereby leading to rotor position estimation errors [90]. This issue is particularly critical in FESSs, where extending the operational speed range is essential to maximize energy storage capacity and system efficiency. In high-speed and low-torque conditions, the weak saliency and high electrical frequency of PMSMs significantly affect observer performance and control stability. Consequently, numerous methods have been proposed to enhance estimation accuracy, restart capability, and dynamic robustness during FW operation.

In railway traction systems, restarting PMSMs in the FW region after power interruptions poses severe difficulties for sensorless drives. To address this, a sensorless restart strategy combining a single zero-voltage vector and a cascade ESO has been developed [91], as shown in Fig. 2.4. By extracting initial position and speed information from the current response to the zero-voltage vector, this method ensures rapid convergence and reliable re-synchronization.

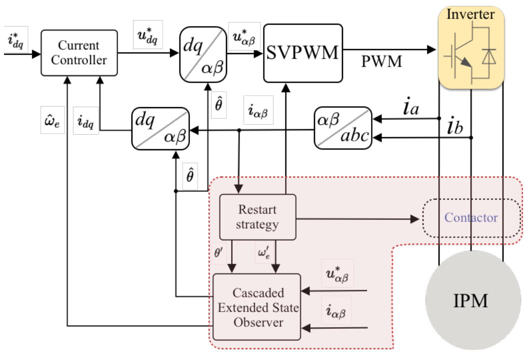

Fig. 2.4: Restart control block diagram based on a single zero-voltage vector and CESO [91].

Beyond restart strategies, predictive and adaptive algorithms have been explored to enhance FW control under sensorless operation. A predictive torque control (PTC) framework integrated with a speed-adaptive flux observer was proposed to overcome flux estimation degradation in induction motor drives under FW conditions [92]. The approach introduces flux and torque scaling factors in the PTC algorithm to compensate for estimation errors, achieving stable speed tracking up to 3.5 times the base speed. Although demonstrated on induction machines, this concept provides valuable insights for PMSM applications requiring high-speed operation with adaptive flux estimation.

In the context of electric vehicles, sliding-mode variable structure control has been employed in combination with voltage-feedback-based FW control to enhance stability during high-speed and low-torque conditions [93]. The use of an improved exponential and variable-rate reaching law mitigates chattering while preserving fast dynamic response, resulting in better anti-disturbance capability and stable operation across a wide speed range. Similarly, to suppress estimation noise and chattering in sensorless systems, a low-pass filter with variable cutoff frequency and an iterative SMO (I-SMO) have been proposed [94]. The adaptive filter effectively minimizes phase delay across both low- and high-speed regions, while the I-SMO reduces chattering and current ripple without the need for high-end processors, ensuring smooth estimation of BEMF and rotor position during FW operation.

In summary, existing research demonstrates significant progress in addressing the sensorless control challenges of PMSMs in the FW region. Restart strategies enhance operational reliability after power loss, predictive torque and flux observers improve dynamic tracking and accuracy, while sliding mode and adaptive observer designs strengthen robustness against nonlinearities and disturbances. These developments collectively establish a foundation for high-performance, wide-speed-range sensorless control essential for advanced PMSM applications in transportation, electric vehicles, and high-speed industrial systems.

2.4.3 SOGI-based Sensorless Control

Accurate rotor position estimation remains a central challenge in sensorless control of PMSMs, particularly under high-speed and FW conditions where BEMF signals become distorted by harmonics and inverter nonlinearities. Conventional LESOs often suffer from phase lag, limited observer bandwidth, and inadequate harmonic suppression, which can degrade estimation accuracy and dynamic response [81]. To address these issues, SOGI-based structures have gained increasing attention in PMSM sensorless control due to their tunable band-pass characteristics and strong noise attenuation capability.

In recent studies, feedforward flux observers employing SOGI current extractors have demonstrated significant improvements in flux and rotor position estimation [95]. By effectively eliminating DC offsets and suppressing harmonics without introducing phase distortion, these methods enhance flux accuracy and dynamic performance. When combined with PLL tracking, SOGI-based current extraction allows for high-fidelity rotor angle and speed estimation even under nonlinear and transient conditions.

Complementary to these developments, dual SOGI frequency-locked loop (FLL) structures have been incorporated into SMO frameworks to address phase delay and chattering issues inherent to conventional SMOs [96]. As shown in Fig. 2.5, the dual SOGI-FLL effectively extracts the fundamental BEMF component while rejecting high-order harmonics, leading to more precise position and speed estimation. Moreover, the integration of a fuzzy logic controller (FLC) further enhances adaptive performance by tuning SMO parameters in real time, reducing chattering and improving robustness against parameter uncertainties.

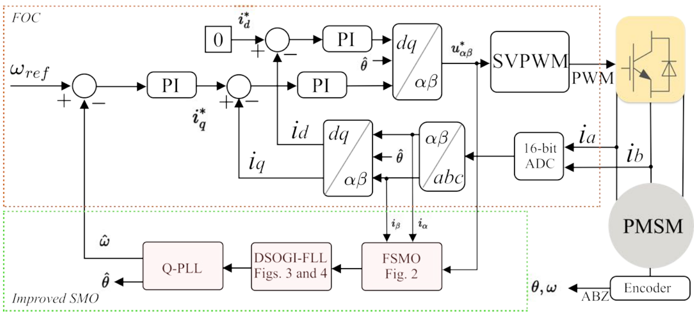

Fig. 2.5: Block of the improved SMO senseless control system of PMSM [96].

For high-speed and low-switching-frequency drives, such as current source converter-fed PMSM systems, a discrete-time SMO with adaptive filtering has been proposed to improve estimation precision near resonant frequencies [97]. As shown in Fig. 2.6, the multiple SOGI-based selected EMF harmonic elimination method is adopted to filter the low-order harmonics. These approaches demonstrate that integrating SOGI-based filtering and observer adaptation can overcome challenges associated with limited sampling rates and high-frequency noise in high-speed PMSM drives.

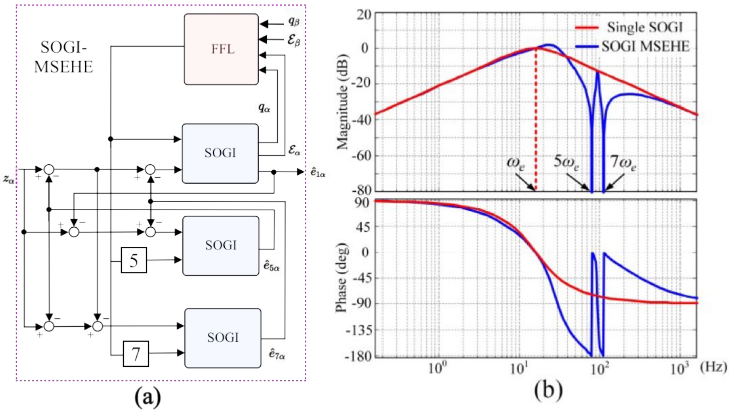

Fig. 2.6: Multiple SOGI-MSEHE. (a) Block diagram. (b) Bode diagram of single SOGI and SOGI-MSEHE [97].

In summary, recent research highlights that combining SOGI-based filters or observers with adaptive control and disturbance rejection mechanisms offers an effective solution for enhancing the precision and robustness of sensorless PMSM drives. These hybrid structures successfully mitigate DC offset, harmonic distortion, and phase lag, making them particularly suitable for high-speed and FW operations where conventional LESOs and PLLs face inherent limitations.

In the FW region, the literature consistently reports degraded sensorless accuracy due to harmonic distortion, inverter nonlinearities, and measurement noise, while conventional LESO/PLL schemes suffer from phase lag and limited harmonic attenuation. Although SOGI-based filtering improves signal quality, there is limited work that tightly integrates SOGI-based conditioning with high-order ESO estimation and a robust outer-loop controller specifically for high-speed SPMSMs in flux-weakening operation. This gap motivates Chapter 5, where a SOGI-enhanced HESO framework is developed to suppress harmonics and noise and to extend estimation bandwidth in flux-weakening, together with an ALADRC-based strategy for robust speed control.

2.5 Sensorless Robust Control of High-speed SPMSM

2.5.1 Sensorless Robust Control Methods

Robust sensorless control of PMSMs is a critical research direction for ensuring stable and accurate operation under modeling uncertainties, load disturbances, and sensor faults, particularly in high-speed and FW regions. Conventional observer-based sensorless control schemes often face performance degradation due to fixed observer parameters, limited adaptability, and poor disturbance rejection, motivating the development of adaptive, nonlinear, and fault-tolerant strategies for improved robustness and dynamic performance.

Recent progress has been made through adaptive bandwidth PLL-based methods. An adaptive QPLL has been proposed to overcome the trade-off between anti-disturbance performance and phase delay inherent to conventional fixed-bandwidth PLLs [76]. By automatically adjusting its bandwidth according to the motor's dynamic condition, the adaptive QPLL minimizes rotor position estimation error and enhances torque utilization. Implemented with a full-order observer, this approach achieves precise field-oriented control (FOC) up to 100 kr/min, improving acceleration by 25 % and maintaining position estimation errors below 3°, thereby enabling reliable high-speed sensorless operation without the need for complex tuning procedures.

To further enhance robustness against modeling uncertainties, an extended observer-based nonlinear control framework combining a continuous SMO and an extended high-gain observer has been developed [98]. The cascaded observer structure suppresses chattering and improves disturbance rejection by compensating for the finite boundary layer of conventional SMOs. Integrated with an integral sliding mode controller, this system achieves fast and accurate speed tracking under bounded uncertainties and load variations, offering high robustness and stability across varying operating conditions.

For wide-speed range operation, a dual-mode sensorless control scheme has been introduced with distinct control strategies for low- and high-speed regions [99]. At low speeds, a voltage tuning approach maintains stable operation when rotor position estimation is unreliable, while at high speeds, an SMO controller pair provides accurate current and speed tracking. The proposed smooth switching algorithm between the two modes ensures continuous operation and high control precision, eliminating torque and current transients during mode transitions.

In addition, fault-tolerant observer designs have been proposed to address sensor failures in PMSM drives, as shown in Fig. 2.7. A PLL-based third-order steady-state linear Kalman filter observer reconstructs rotor position and speed using only stator voltage and current information, thereby maintaining control continuity in the absence of speed sensors [100].

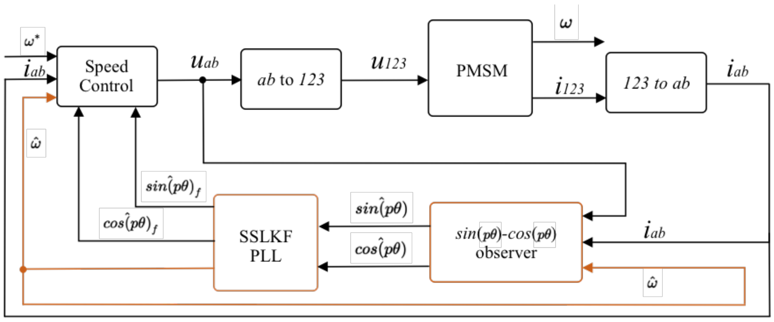

Fig. 2.7: Block scheme for the new sensorless control strategy [100].

2.5.2 ESO for PMSMs Robust Control

ESOs have been widely adopted in ADRC systems for PMSMs due to their ability to estimate and compensate for total disturbances, including model uncertainties, external load variations, and inverter nonlinearities, without requiring an accurate mathematical model. In recent years, several advanced ESO structures have been proposed to enhance disturbance estimation precision, speed tracking accuracy, and dynamic robustness. These include double-stage ESOs (2S-ESOs) [101], adaptive switching high-order ESOs (ASHESOs) [102], and third-order super-twisting ESOs (STESOs) [103].

The double-stage ESO (2S-ESO) structure introduces a cascaded observer framework to improve the disturbance estimation bandwidth and steady-state accuracy of ADRC systems, as shown in Fig. 2.8. Conventional LESOs exhibit limited disturbance rejection capability due to the constraint between observer bandwidth and noise attenuation. To overcome this, the 2S-ESO integrates the advantages of both cascaded ESOs and quasi-resonant control, forming a two-layer configuration. The first stage enhances the estimation order of the disturbance model, improving precision in aperiodic disturbance rejection. The second stage embeds a quasi-resonant compensator to accurately estimate and attenuate periodic disturbances caused by inverter harmonics or torque ripple [101].

Building upon this concept, an ASHESO has been developed to further improve estimation accuracy under time-varying disturbance conditions. Conventional ESOs suffer from degraded performance when confronted with rapidly changing disturbances or measurement noise. The ASHESO addresses this limitation through a frequency-domain analytical design, optimizing the observer gain and pole locations to balance noise suppression with fast response. Furthermore, an adaptive switching gain mechanism dynamically tunes the observer gain based on real-time tracking error,

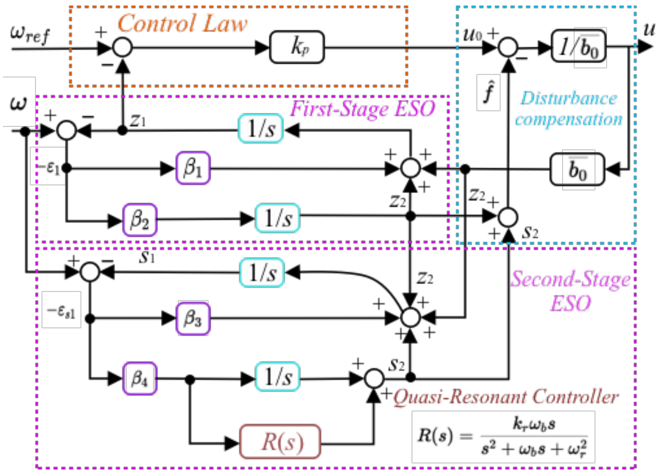

Fig. 2.8: Block diagram of the proposed 2S-ESO-ADRC [101].

ensuring high responsiveness during transient conditions and low sensitivity to noise in steady-state operation [102].

For scenarios involving rapid dynamic variations, a STESO has been proposed to enhance the dynamic performance of position and speed estimation, particularly in interior PMSM (IPMSM) drives [103]. This method extends the conventional second-order LESO by incorporating a super-twisting algorithm, which provides finite-time convergence and strong robustness against matched and unmatched disturbances. The third-order structure enables faster estimation of mechanical states (position, speed, and disturbance torque) and electrical variables, significantly improving transient performance under sudden load or speed changes.

However, most ESO-based PMSM control methods have been experimentally validated only in low- to medium-speed regions, which typically range between 600 r/min and 3,000 r/min, corresponding to electrical frequencies of 50–200 Hz [84, 85, 101–103]. These observers are primarily designed for low-speed operating conditions, where signal magnitudes are weak and the influence of noise is more pronounced. In such cases, conventional LESOs behave as second-order low-pass filters, introducing phase lag between the estimated and actual BEMF. While increasing the observer bandwidth can reduce this lag, it simultaneously amplifies high-frequency noise, degrading overall system stability [81].

In contrast, HSPMSMs, which typically operate above 10,000 r/min, require observers with higher bandwidth and faster dynamic response to track rapid state variations and compensate for strong nonlinearities. The conventional low- and medium-speed ESOs cannot adequately balance noise suppression and estimation speed in such environments. Therefore, developing advanced ESO structures is essential to extend robust sensorless control into the high-speed domain.

In summary, recent progress in ESO-based robust control demonstrates significant advancements in disturbance rejection, adaptive gain tuning, and dynamic performance enhancement. Nevertheless, the extension of these methods to high-speed PMSMs remains limited, highlighting the need for new observer designs that achieve high-bandwidth estimation with effective noise suppression, enabling precise and stable control across wide operating ranges.

2.5.3 Robust Control in the Flux-Weakening Region

In high-speed operation, PMSMs enter the FW region where voltage constraints and nonlinear dynamics significantly affect control performance. Traditional fixed-bandwidth controllers struggle to maintain stability and fast response under varying load and parameter conditions. Thus, adaptive and robust control strategies have been developed to ensure smooth transitions, precise current regulation, and strong disturbance rejection in FW operation.

A bandwidth-based adaptive FW control method introduces nonlinear voltage compensation and real-time speed-dependent bandwidth tuning [104]. The scheme requires only one manually set bandwidth parameter and includes a $q-$axis current compensator to reduce voltage overshoot and improve transient response. Experimental results verify the method's simplicity, stability, and adaptability under wide-speed operation.

To improve dynamic performance, a parameter-optimized FW controller based on the adaptive velocity particle swarm optimization algorithm was proposed [105]. It optimizes the anti-windup PI controller gains to prevent saturation and minimize errors without relying on motor transfer functions. The resulting control system enables fast transitions and high steady-state accuracy between torque and FW regions.

An online adaptive current vector adjustment method further enhances deep FW control for IPMSMs [106]. The approach uses a flexible current vector algorithm and an adaptive torque-angle loop to improve dynamic stability and nonlinear compensation, as shown in Fig. 2.9. It ensures smooth transitions across maximum torque per ampere (MTPA), FW, and deep FW regions, suitable for high-speed EV drives.

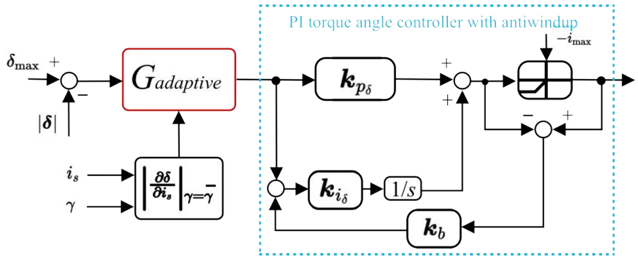

Fig. 2.9: Block diagram of the proposed adaptive torque angle control loop with the antiwindup structure [106].

For enhanced robustness, a one-degree-of-freedom ADRC combined with a sampled-data iterative learning controller (ILC) suppresses both periodic and aperiodic disturbances [107]. The ILC improves disturbance rejection beyond conventional ADRC, achieving smooth speed output and accurate tracking under fluctuating loads.

A variable structure ADRC introduces a two-stage variable structure ESO to enhance both disturbance rejection and noise suppression [108], as shown in Fig. 2.10. The proposed observer achieves faster convergence at low frequencies and stronger high-frequency attenuation. Experimental validation confirms improved robustness and noise immunity in PMSM speed control under FW conditions.

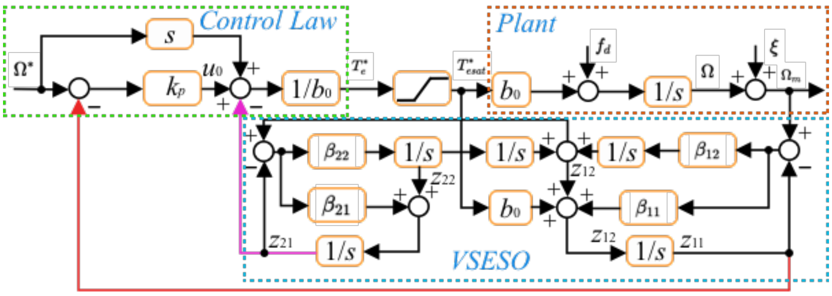

Fig. 2.10: Schematic diagram of the variable structure ADRC based on variable structure ESO [108].

Overall, recent advancements in robust FW control emphasize adaptive bandwidth tuning, intelligent optimization, and ADRC-based disturbance rejection. These methods achieve higher precision, faster response, and stronger robustness, paving the way for reliable high-speed SPMSM operation under complex nonlinear FW environments.

While ADRC-based robust control provides disturbance rejection, the reviewed studies indicate that fixed-bandwidth observer designs struggle to simultaneously achieve fast high-speed dynamics and strong noise immunity, especially under parameter mismatches and inverter nonlinearities. Moreover, robust control and sensorless estimation are often treated separately, reducing achievable performance in high-speed SPMSM drives. These limitations motivate the integrated sensorless and robust control frameworks developed in Chapters 4 and 5, where disturbance estimation is explicitly leveraged for control compensation, and adaptive robustness is strengthened for high-speed and FW operation.

2.6 Summary

This chapter reviewed existing research on modeling, sensorless control, and robust operation of PMSMs and HSPMSMs. For electromagnetic performance analysis, conventional FEA offers high accuracy but is computationally expensive, motivating reduced-order methods such as POD-based MOR. In sensorless control, conventional approaches and linear ESOs suffer from bandwidth limits, phase lag, and noise sensitivity, especially in high-speed and FW regions. FW operation introduces additional challenges due to inverter nonlinearities and harmonics. Robust control methods, including ESO and LADRC, provide disturbance rejection but lack adaptive bandwidth for fast high-speed dynamics.

The literature highlights three main gaps that directly motivate the contributions of this thesis. (i) Efficient modelling: FEA remains too computationally expensive for iterative analysis and control-oriented studies, while existing MOR applications in electrical machines are still limited in dynamic modelling for BPMSMs; this motivates the POD-based MOR framework developed in Chapter 3. (ii) High-speed sensorless accuracy: conventional observers and LESO-based methods face bandwidth limitations, phase lag, and sensitivity to noise and inverter harmonics; this motivates the cascade high-order ESO (CHESO) sensorless strategy in Chapter 4. (iii) Flux-weakening robustness: estimation accuracy further degrades in FW due to harmonics and nonlinearities, and existing methods insufficiently integrate harmonic suppression with high-bandwidth estimation and robust speed control; this motivates the SOGI-HESO and ALADRC framework in Chapter 5. Together, these chapters form a coherent modelling-to-control pathway toward reliable, high-performance high-speed SPMSM drives.

Chapter 3

Modeling, Analysis, and Control System of PMSMs

3.1 Introduction

This chapter addresses the research gap in fast and accurate electromagnetic modelling required for advanced sensorless and robust control of high-speed PMSM systems. A bearingless PMSM is adopted as a representative case study to develop and validate POD-based MOR framework that enables efficient dynamic performance evaluation. The modelling principles and reduced-order representations established in this chapter provide the computational foundation for the sensorless estimation and robust control strategies implemented and experimentally validated on a high-speed SPMSM in the subsequent chapters.

With the improvement of the digitalization of electrical machines and their drive systems, it is an inevitable trend to realize accurate and fast physical simulation and behavior modeling methods. The realization of digitalization is also helpful to the calculation of performance and coupling analysis in other systems. It is of great significance to monitor and control system operating conditions.

This chapter presents an electromagnetic performance analysis method for fast dynamic simulation of a BPMSM based on MOR. The electromagnetic characteristics and dynamic behavior model of the rotating machine are constructed by using the MOR based on POD. First, the $q-$ and $d-$axis currents and rotor angle of the motor are scanned to construct the magnetic field distribution snapshot matrix. Then, the singular value decomposition of the snapshot matrix is used to calculate the basis vectors. Finally, the order of the system is reduced by selecting an appropriate truncation order of the basis vectors. Compared with the FEM, the calculation time of MOR for the BPMSM is significantly reduced. At the same time, it can provide accurate results of motor magnetic field distribution, electromagnetic force, levitation force, and dynamic response calculations, and achieve fast and accurate state feedback. Through analysis and comparison, the results of the proposed method match well with the FEM simulations.

The proposed MOR model is validated using a two-stage approach. First, the fidelity of the underlying electromagnetic reference model is confirmed experimentally by comparing predicted cogging torque with prototype measurements, establishing FEM as a reliable benchmark for the studied machine. Second, because comprehensive experimental measurements are not available for all operating conditions, the MOR results are primarily validated against FEM across a wide set of current and rotor-angle snapshots. This FEM-referenced validation is therefore adopted to rigorously quantify MOR accuracy while maintaining practical experimental effort.

3.2 Modeling of PMSM and BPMSM

3.2.1 Mathematical Model of PMSM

The electrical dynamic equations for PMSM and HSPMSM are in the stationary $\alpha\beta$-coordinate system and can be expressed as

$$\begin{cases} \dot{i}_\alpha = -(1/L_s)R_s i_\alpha + (1/L_s)u_\alpha - (1/L_s)e_\alpha \\ \dot{i}_\beta = -(1/L_s)R_s i_\beta + (1/L_s)u_\beta - (1/L_s)e_\beta \end{cases} \tag{3.1}$$

with e_α and e_β as

$$\begin{cases} e_\alpha = -\omega_e \psi_f \sin(\theta_e) \\ e_\beta = \omega_e \psi_f \cos(\theta_e) \end{cases} \tag{3.2}$$

where $(\dot{\ })$ is the differential operator, i_α, i_β, u_α, u_β and e_α, e_β are the stator current, stator voltage and equivalent BEMF in the α, β-frame, respectively. R_s is the stator resistance, L_s is the inductance, ω_e is the rotor electrical speed, ψ_f is the PM flux linkage, θ_e is the rotor position angle.

The mechanical dynamic equation is

$$\dot{\omega}_m = \frac{1}{J}(T_e - T_L - B\omega_m) \tag{3.3}$$

where ω_m is the mechanical angular velocity, T_e is the electromagnetic torque, T_L is the load torque, J is the moment of inertia, B is the damping factor.

The electromagnetic torque equation is

$$T_e = \frac{3}{2}p_n\psi_f i_q \tag{3.4}$$

where p_n is the pole pairs, and i_q is the $q-$axis current.

3.2.2 Mathematical Model of BPMSM

In this study, the electromagnetic 2-D modeling of the motor is considered. The physics model of differential equation employed in this study is denoted by [59]

$$\nabla \cdot \left(\left(\frac{1}{\mu}\nabla A\right)\right) = -J_0 + \nabla \times \left(\frac{B_r}{\mu}\right) \tag{3.5}$$

where J_0 is the applied density current source, B_r is the remanent flux density of PM, A is the magnetic vector potential, and μ represents the permeability.

For the BPMSMs, their levitation force can be expressed as follows using the Maxwell stress tensor approach [60]

$$\mathrm{d}F(\theta) = \frac{B^2(\theta,t)}{2\mu_0}ds = \frac{B^2(\theta,t)}{2\mu_0}lrd\theta \tag{3.6}$$

where $B(\theta, t)$ is the flux density in the air gap, s denotes the area of the rotor surface, l is the length of the armature, μ_0 is permeability in the vacuum, and r represents the radius of the air gap.

The expression for the levitation force can be obtained by solving (3.6) and then decomposing it into its $x-$ and $y-$axis components [60]

$$\begin{cases} F_x = k_a I_L I_{\mathrm{Tp}} \cos(\theta_T - \theta_L) + k_b x \\ F_y = k_a I_L I_{\mathrm{Tp}} \sin(\theta_T - \theta_L) + k_b y \end{cases} \tag{3.7}$$

where the levitation forces along the $x-$ and $y-$axis are denoted as F_x and F_y, respectively. The electrical angles of the levitation winding current and the torque winding current are represented by θ_T and θ_L, respectively. Meanwhile, x and y represent the radial displacement along the $x-$ and $y-$axis, respectively. The levitation winding current is denoted as I_L, and the equivalent current that consists of the torque winding current and PM equivalent current is represented by I_{Tp}. Moreover, k_a and k_b are two parameters that are related to the structure of the BPMSM.

3.3 Model Order Reduction for BPMSMs

3.3.1 Proper Orthogonal Decomposition Based MOR

To obtain MOR results for assessing the electromagnetic performance of a BPMSM, the following steps, as shown in Fig. 3.1, can be followed.

Step 1 is to construct the magnetic field distribution snapshot matrix. According to the finite element variational principle, by constructing an interpolation function, the vector magnetic potential distribution at any point in the magnetic field space is a function of coordinates, and the magnetic vector potential at a node point is directly obtained by solving linear or nonlinear equations. In the grid, the internal vector magnetic potential is obtained by interpolation. Therefore, the 2-D nonlinear finite element model can be expressed as the following form:

$$SX = F \tag{3.8}$$

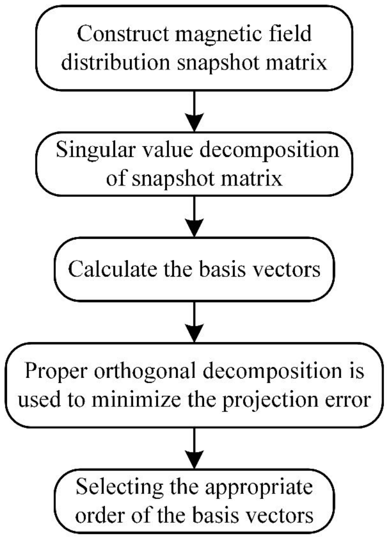

Fig. 3.1: Basic process of building the MOR.

where X is the vector magnetic potential matrix that needs to be solved, which size is $n \times 1$, and n is the number of grid points. F is the input matrix calculated from the current source density, and its size is $n \times 1$. S is the stiffness matrix, which is assembled by the stiffness matrix corresponding to each grid point in a certain order. The form and size of the stiffness matrix are related to the degree of freedom of the vector magnetic potential matrix.

FEM is utilized to compute the magnetic fields at a mechanical angle θ for different $d-$ and $q-$axis currents. The resulting fields are used to construct a snapshot matrix. When establishing the snapshot matrix, we can assume that the number of system working conditions is n and the number of sample points under each working condition is m, and usually m>n. Thus, the snapshot matrix of m rows and n columns can be constructed, and each column is recorded as $x_i, i = 1, 2, \ldots, n$. Assume that the snapshot matrix is $X = [x_1, x_2, \ldots, x_n] \in R^{n \times m}$.

$$X = \begin{bmatrix} x_{11} & \cdots & x_{1n} \\ \vdots & \ddots & \vdots \\ x_{m1} & \cdots & x_{mn} \end{bmatrix} \tag{3.9}$$

Step 2 is the singular value decomposition of the snapshot matrix. By performing singular value decomposition, we can obtain

$$X = U\mathrm{diag}\{\Sigma_r, 0\}V^T \tag{3.10}$$

where U and V are the left and right singular matrices obtained by POD, respectively.

Step 3 is to calculate the basis vectors. According to the above formula, we can decompose a matrix into a multiplication of three matrices. If the column vectors of the matrix diag $\{\Sigma_r, 0\}U^T$ are represented by $d_1, d_2, \ldots, d_m$ respectively, then each column element in the snapshot matrix can be represented by the linear superposition of this set of column vectors, which is a set of orthogonal basis vectors for the system.

Step 4 is POD to minimize the projection error. The goal of MOR is to accelerate the simulation of (3.8) by reducing computational complexity. Since the discretization of (3.5) leads to an extensive linear system that needs to be solved for every angular position, the rotation simulation is computationally expensive. The magnitude of the magnetic vector potential in the 2-D magnetic field can be considered as the superposition of magnetic fields in different modes. By using POD, each magnetic field can be calculated using the basis vector obtained from a set of previously computed snapshots.

To minimize the mean projection error of selecting basis vectors, the POD basis

$$\begin{aligned} &\min_{\psi_1,\ldots,\psi_N \in R^N} \sum_{k\in K} \left| x^k - \sum_{i=1}^{\mathcal{N}} \langle x^k, \psi_i\rangle_W \psi_i \right|_W^2 \\ &\text{s.t.} \left\langle \psi_i, \psi_j \right\rangle_W = \delta_{ij}, \quad \text{for} 1 \le i, j \le \mathcal{N}., \end{aligned} \tag{3.11}$$

For a fixed angle, let $X \in R^N$ be the solution to (3.5). K is an index set with elements in N.$\langle\cdot,\cdot\rangle_W$ stands for the weighted inner product in R^N, a symmetric matrix

Step 5 is selecting the appropriate order of basis vectors. By solving the optimization problem in (3.11), a POD basis $\{\psi_i\}_{i=1}^{l}$ is calculated from these snapshots. Assuming that the projection matrix composed of basis vectors obtained by the POD method is ψ, the magnetic flux density distribution $\mathbf{X}$ of the original system can be approximated by a low-dimensional $\mathbf{X}_r$

$$\mathbf{X}_r = \mathbf{X}\psi \tag{3.12}$$

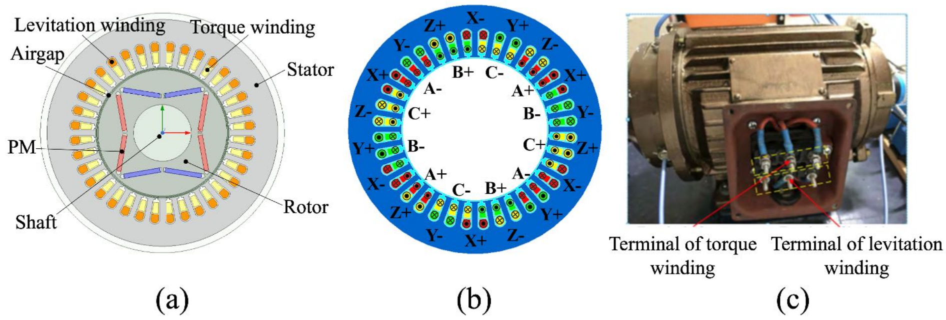

Fig. 3.2: Studied BPMSM. (a) Structure. (b) Winding layout. (c) Photograph of the prototype.

The subscript r is the dimension that we want to reduce.

3.3.2 Case Study of BPMSM

While the general principles of POD–based MOR are well established in computational mechanics and electromagnetics, their direct application to bearingless PMSMs presents nontrivial challenges due to the coupled torque–levitation dynamics and the dependence on multiple electrical and mechanical states. The original contribution of this chapter lies in the formulation of a control-oriented MOR framework tailored for BPMSMs, including the systematic construction of snapshot matrices over combined $d-$ and $q-$ axis current and rotor-angle operating spaces, the integration of levitation-force computation within the reduced-order model.

This case study validates the proposed MOR model using FEM as the main benchmark and uses limited prototype measurements to confirm the FEM reference model. Fig. 3.2(a) and (b) display a 2-D model of the BPMSM created using Ansys Maxwell, along with the winding layout of the BPMSM. The model comprises a stator with slots and windings denoted as A, B, and C. The rotor is positioned at the center of the stator and is equipped with permanent magnets (PMs). The levitation windings, denoted as X, Y, and Z, are placed inside the stator. In Fig. 3.2(c), the physical prototype of the BPMSM is shown. Table 3.1 lists the major dimensions and parameters of the model.

The initial analysis is concentrated on the local flux density distribution, which is critical as it serves as the basis for the subsequent processing of torque. FEM simulation results are used to compare the flux density distribution with those obtained using the full and reduced models, and

Table 3.1: Parameters of the BPMSM.

Parameter	Unit	Value
Outer radius of stator	mm	52
Outer radius of rotor	mm	29
Number of stator slots	-	36
No. of pole pairs of torque winding	-	2
No. of pole pairs of levitation winding	-	3
Length of airgap	mm	1
Length of stator	mm	75
Material of PM	-	NdFeB-35
Material of stator and rotor core	-	DW350-50
Coercive force of PM	kA/m	900

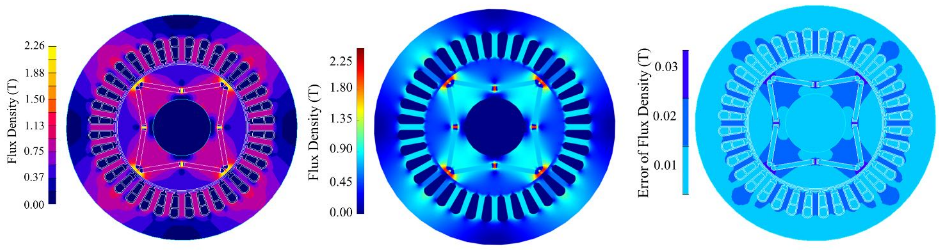

(a) (b) (c)

Fig. 3.3: Comparison of results. (a) Reference flux density by FEM. (b) Calculated flux density by POD. (c) Maximum error between reference and calculation.

the deviation between the two models' solutions is illustrated in Fig. 3.3. It is noticeable that the result of MOR calculation matches the FEM simulation very well, and the maximum and average relative errors are only 1.32% and 0.51%, respectively. Cogging torque is a distinctive problem of permanent magnetic motors, and it must be considered and addressed during the design of BPMSM. Fig. 3.4 compares the FEM-predicted cogging torque with prototype measurements, showing close agreement and thereby validating the FEM model as an accurate reference for this machine. Because experimental measurements are limited for other quantities, MOR is validated primarily against FEM for flux density, levitation forces, torque, and dynamic responses, as reported in Figs. 3.3 and 3.6–3.11.

The chart of the energy proportion of the orthogonal basis corresponding to each singular value changing with the number of singular values is shown in Fig. 3.5. It can be seen that for this snapshot matrix, the energy proportion decreases significantly with the singular value. The majority of the energy is captured by the first few singular values, with the first three singular values accounting

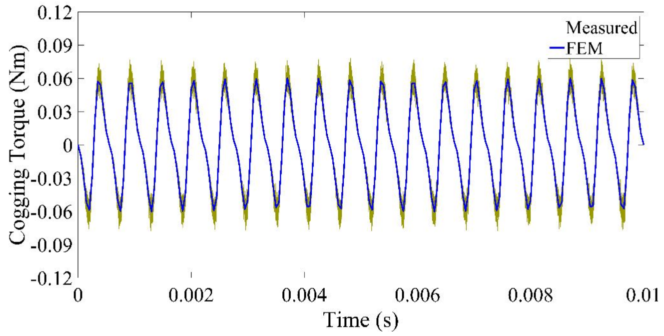

Fig. 3.4: Comparison between measured and FEM results.

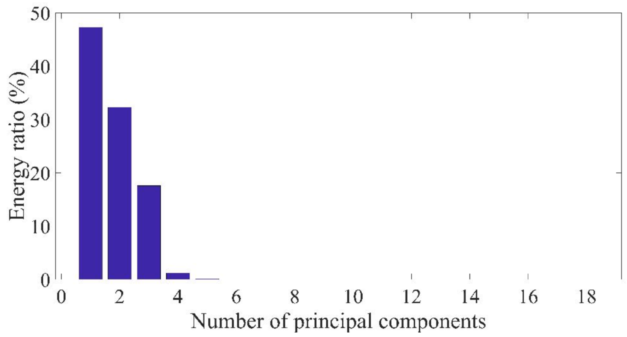

Fig. 3.5: Relation between energy and the number of principal components.

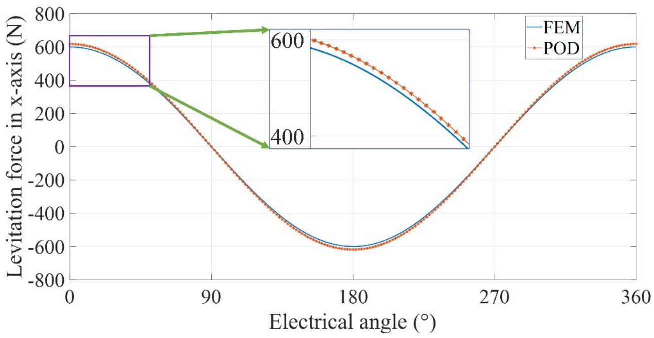

Fig. 3.6: FEM and MOR calculation of levitation force in the $x-$axis.

for over 97% of the energy. Subsequent singular values exhibit relatively minor changes.

According to (3.7), the FEM and MOR calculation results of levitation force in x- and y-axes are shown in Figs. 3.6 and 3.7, respectively. The results show that the proposed MOR results match well with the FEM simulations for the levitation force of BPMSM. To obtain the results in Figs. 3.6 and 3.7, the FEM simulation spends 720 s with the CPU model Intel Xeon Gold, and the total number of CPU processors is 64, while the MOR calculation takes only 0.15 s.

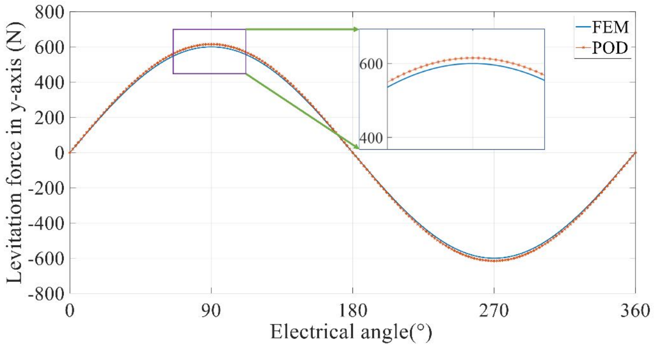

Fig. 3.7: FEM and MOR calculation of levitation force in the $y-$axis.

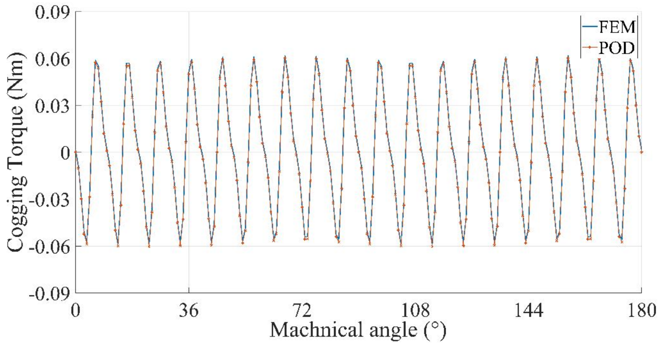

Fig. 3.8: FEM and MOR calculations of cogging torque.

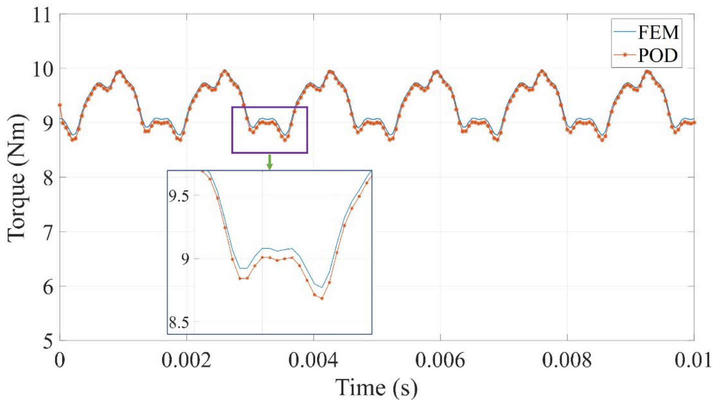

Fig. 3.9: FEM and MOR calculations of the waveform of output torque.

As illustrated in Fig. 3.8, one cogging torque cycle covers a mechanical angle of 10°, which agrees with the initial design. In Fig. 3.9, the torque performance of the proposed BPMSM is depicted when a current of 5 A is supplied to the torque winding. The results demonstrate that the proposed MOR method produces torque values that closely align with the full FEM simulation.

A step rise of the load is used to test the dynamic behavior of the BPMSM. In this case, a 2 Nm torque load is added at a time of 0.5 s, and the changes in the speed of the BPMSM are presented and

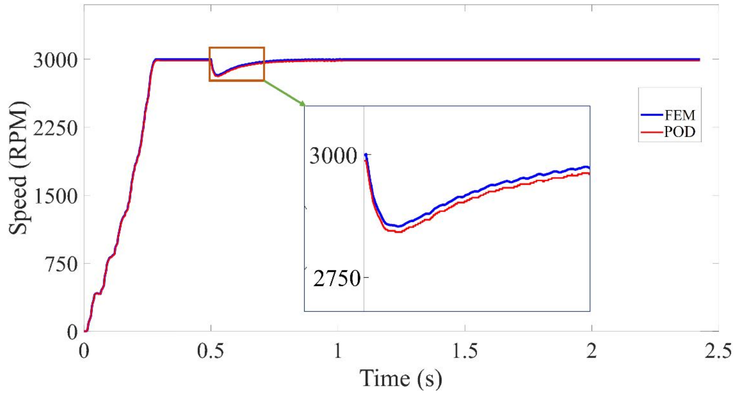

Fig. 3.10: Speed response of FEM and MOR results with changing load.

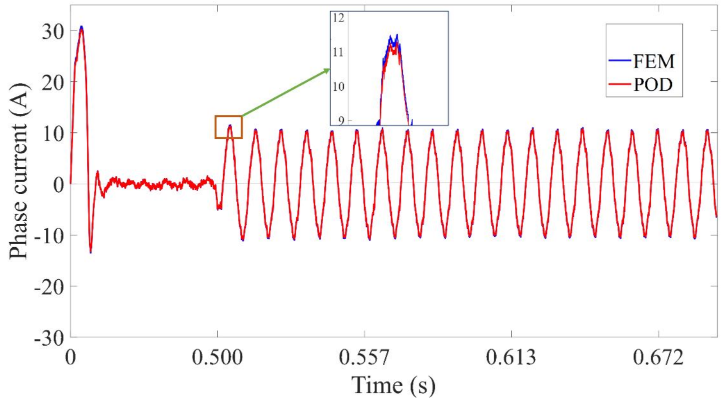

Fig. 3.11: Phase current comparison of FEM and MOR results with changing load.

compared in Fig. 3.10. As shown in Fig. 3.11, the one-phase current results of MOR calculation are well matched with full FEM model simulation. The proposed BPMSM MOR model can reflect the dynamic behavior of the motor fast and accurately.

The maximum and mean error between FEM simulation and MOR calculation for different characteristics of BPMSM are shown in Table 3.2, the maximum difference is less than 2%, and the mean error is less than 0.7%. According to the analysis results, it can be concluded that the proposed MOR model of BPMSM exhibits comparable electromagnetic characteristics in terms of flux density, levitation force, torque, and speed compared to the FEM simulation.

In summary, this case study presents a POD-based MOR method for analyzing BPMSMs and computes the flux density, levitation force, torque, and speed response using the proposed method. The numerical results demonstrate that the MOR method can efficiently provide solutions with significantly reduced simulation time for the electromagnetic characteristics and dynamic behavior

Table 3.2: Error between the FEM simulation and MOR calculation

Name	Maximum(%)	Mean(%)
Flux density	1.32	0.51
Levitation force in the $x-$axis	1.83	0.68
Levitation force in the $y-$axis	1.85	0.67
Cogging torque	0.83	0.39
Torque	1.77	0.61
Speed	0.79	0.56

of BPMSMs compared to the FEM simulation. Moreover, the MOR method achieves comparable accuracy, with a maximum torque difference of less than 2%.

In terms of validation, prototype cogging torque measurements are used to confirm the accuracy of the FEM reference model, while MOR performance is quantitatively assessed against FEM for flux density, levitation force, torque, and dynamic responses due to the limited availability of comprehensive experimental measurements across the full operating space. This two-stage validation strategy provides both experimental grounding and rigorous accuracy evaluation for the proposed MOR framework.

3.4 Summary

This chapter proposed a POD-based MOR method for the electromagnetic performance analysis of BPMSMs. The MOR approach significantly reduces computation time while maintaining high accuracy in flux density, torque, levitation force, and dynamic responses, making it more practical than conventional FEM for iterative studies. The motivation for this analysis is that high-speed sensorless and robust control strategies require fast and accurate motor performance evaluation, and MOR provides the necessary foundation by enabling rapid modeling without sacrificing precision. A case study and experimental validation confirmed that the MOR method achieved errors below 2% compared with FEM while drastically improving efficiency. In addition, the development of the experimental testbench and control platform established the basis for implementing and validating the advanced sensorless and robust control strategies presented in later chapters.

Beyond numerical acceleration, the key original contribution of this chapter is the development of a reduced-order electromagnetic model that is explicitly suited for control-oriented analysis of bearingless PMSMs. By incorporating torque and levitation-force dynamics within a unified POD-based MOR framework and validating both steady-state and transient behaviours, the proposed modelling approach bridges the gap between high-fidelity FEM analysis and real-time sensorless and robust control design. Building on this modelling foundation, Chapter 4 develops high-bandwidth sensorless estimation strategies for high-speed SPMSMs, while Chapter 5 further integrates harmonic suppression and robust control techniques to ensure stable operation in flux-weakening and disturbance conditions.

Chapter 4

Sensorless Control of High-speed SPMSMs Based on Cascade High-Order ESO

4.1 Introduction

This chapter addresses the research gap in accurate and high-bandwidth sensorless estimation for high-speed surface-mounted PMSMs (SPMSMs), where conventional observer-based methods suffer from bandwidth limitations, phase lag, and sensitivity to disturbances. Based on the MOR strategy established in Chapter 3, a cascade high-order extended state observer (CHESO) is developed to enable accurate sensorless estimation for high-speed SPMSMs. The proposed sensorless framework establishes the estimation basis required for the robust control strategies introduced in the following chapter.

In this chapter, a CHESO is proposed to enhance position estimation and speed control for high-speed SPMSMs. In the proposed two-level CHESO architecture, the BEMF is accurately estimated at the first level, while rotor position, load torque, and uncertain disturbances are concurrently estimated at the second level. Furthermore, an adaptive torque feedforward control strategy utilizing the estimated disturbances and load torque is employed to improve dynamic performance and disturbance rejection capabilities. Owing to the two-level cascade structure, each observer level can be independently tuned with suitable observer gains, enabling accurate estimation of rapid motor dynamics without excessively amplifying measurement noise, thus achieving superior performance in sensorless control of high-speed SPMSMs.

4.2 Drive System of High-Speed SPMSM

The experimental platform introduced in this chapter is primarily used to verify the proposed sensorless estimation and robust control strategies, while the same hardware platform is employed in Chapters 4 and 5. A detailed description of the experimental setup is therefore consolidated in Chapter 4 for clarity and consistency.

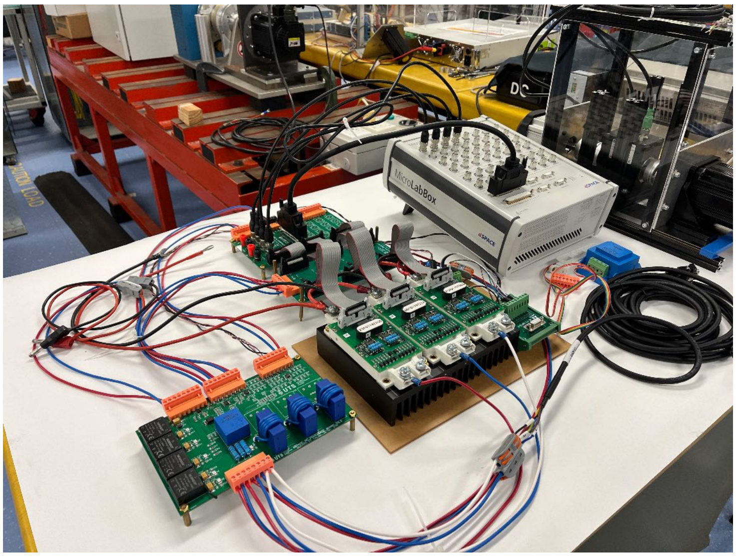

Fig. 4.1: Overview of testbench and drive system setup for high-speed SPMSM.

The experimental platform for the high-speed SPMSM consists of a three-phase inverter, a dSPACE control system, and a sensor interface board for current and voltage acquisition, as shown in Figs. 4.1–4.4.

As shown in Fig. 4.2, the three-phase inverter employs 2SP0115T2C0 IGBT intelligent power modules configured in a half-bridge topology for each phase, and the modules of IGBT are the FF600R12ME4_B72. This design provides high switching capability and low conduction loss, making it suitable for high-speed operation and dynamic testing. Each phase leg integrates isolated gate drivers and protection circuits to ensure reliable switching and short-circuit protection during

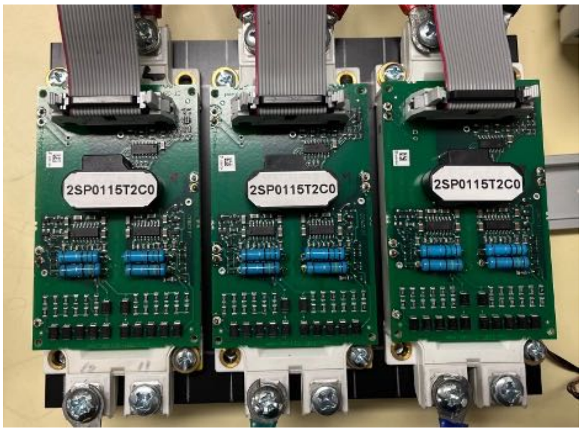

Fig. 4.2: Three-phase inverter for HSPMSM.

high-frequency modulation. The gate driver is supplied through a DC–DC power supply board, which also supports voltage and current measurement circuits.

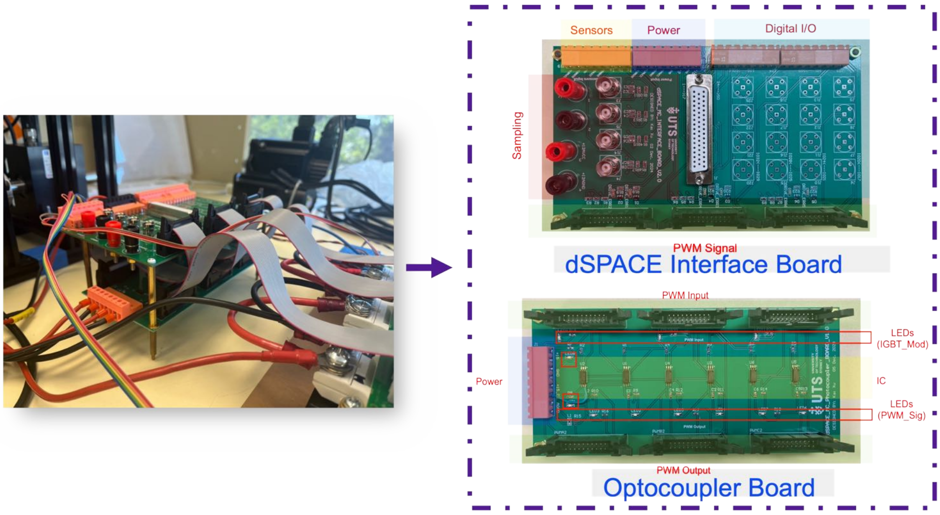

Fig. 4.3: The dSAPCE interface board and PWM optocoupler board.

The dSPACE control system serves as the core of the real-time control platform. It performs PWM generation, data acquisition, and execution of advanced control algorithms. The dSPACE controller generates PWM control signals, then its transmitted through a dSPACE interface board that manages sampling, power, and digital I/O. These signals are subsequently passed through a PWM optocoupler board, which ensures galvanic isolation between the low-voltage control electronics and the high-voltage inverter stage. The optocoupler board transmits isolated PWM signals to the inverter's gate driver units, providing both signal integrity and protection against electromagnetic interference, as shown in Fig. 4.3.

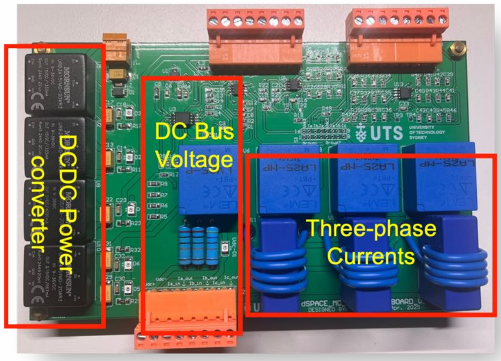

Fig. 4.4: DC power supply, voltage and current sensors.

A DC measurement board integrates a compact DC–DC power supply, a DC bus voltage sensor, and three-phase current transducers. The bus voltage sensor monitors up to 500 V with high precision, while the LEM current sensors measure up to 25 ARMS, providing isolated and linear current feedback. The measured analog signals are transmitted back to the dSPACE system through high-speed ADC channels for real-time control, monitoring, and data logging.

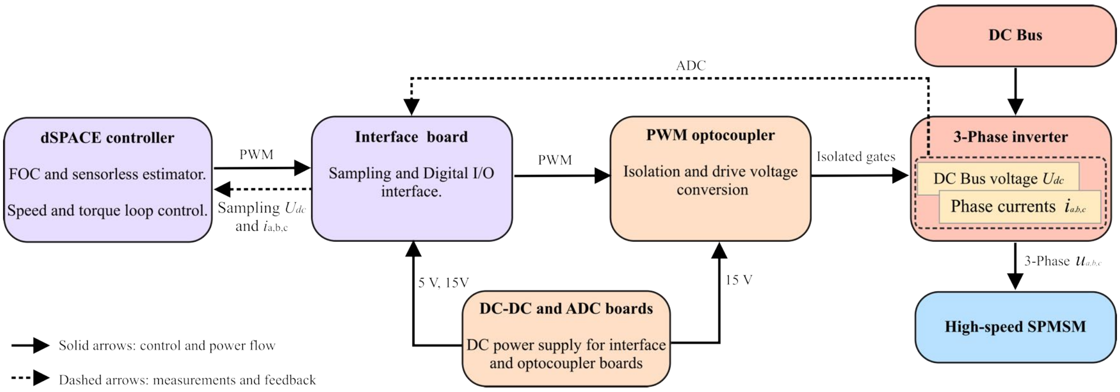

Fig. 4.5: The overall hardware system architecture.

The overall control system architecture is illustrated in Fig. 4.5. The signal flow begins with the dSPACE controller executing FOC, FW, and sensorless estimation algorithms. PWM commands are then sent through the interface and optocoupler boards to the inverter, which drives the high-speed SPMSM. Motor phase currents and DC bus voltage are measured by the sensor board and fed back to the dSPACE unit, closing the control loop. This integrated hardware and control system enables high-bandwidth current control, precise speed regulation, and robust sensorless operation of the high-speed SPMSM, supporting experimental validation under both steady-state and transient conditions.

4.3 Conventional ESO Sensorless Control of High-speed SPMSMs

4.3.1 Conventional ESO for sensorless control

For a typical first-order system, if the unknown interference is extended as a state, the system is equal to a second-order system. The equation of state of the system can be expressed as

$$\begin{cases} \dot{x}_1 = x_2 + b_0 u_0 + f(t) \\ \dot{x}_2 = \dot{f}(t) \\ y = x_1 \end{cases} \tag{4.1}$$

where x_1 and x_2 are the state variable, $f(t)$ is the total external and internal disturbance of the system, u_0 is the input of the system and b_0 is the coefficient of the system input, y is the output of the system.

The linear extended state observer (LESO) equation containing the estimated state and total perturbation can be expressed as

$$\begin{cases} e_1 = \hat{x}_1 - x_1 \\ \dot{\hat{x}}_1 = \hat{x}_2 + b_0 u_0 + \hat{x}_1 - l_1 \cdot e_1 \\ \dot{\hat{x}}_2 = -l_2 \cdot e_1 \end{cases} \tag{4.2}$$

where $(\hat{\ })$ represents the estimated value of a variable. e_1 is the estimation error of x_1, l_1 and l_2 are the gains of the LESO.

Then, according to (4.1), (3.1) can be expressed as

$$\dot{\boldsymbol{x}}_1 = -\mu \boldsymbol{x}_1 + b_0 \boldsymbol{u}_0 + \boldsymbol{x}_2 \tag{4.3}$$

where $\boldsymbol{x}_1 = [i_\alpha, i_\beta]^T$, $\boldsymbol{x}_2 = [-e_\alpha/L_s, -e_\beta/L_s]^T$, $\boldsymbol{u}_0 = [u_\alpha, u_\beta]^T$, $b_0 = 1/L_s$, $\mu = R_s/L_s$.

According to (4.2) and (4.3), the conventional LESO for the BEMF estimation can be expressed as

$$\begin{cases} \boldsymbol{e}_1 = \hat{\boldsymbol{x}}_1 - \boldsymbol{x}_1 \\ \hat{\boldsymbol{x}}_1 = \hat{\boldsymbol{x}}_2 + b_0 \boldsymbol{u}_0 + u\hat{\boldsymbol{x}}_1 - l_1 \cdot \boldsymbol{e}_1 \\ \hat{\boldsymbol{x}}_2 = -l_2 \cdot \boldsymbol{e}_1 \end{cases} \tag{4.4}$$

According to (4.3) and (4.4), the characteristic equation and transfer function of ESO can be obtained. Then, the transfer function of ESO can be expressed as

$$G_{\text{ESO}}(s) = \frac{\hat{E}_{\alpha,\beta}(s)}{E_{\alpha,\beta}(s)} = \frac{\omega^2}{s^2 + 2\omega s + \omega^2}. \tag{4.5}$$

where ω is the bandwidth of the LESO. According to (4.5), the conventional LESO exhibits a second-order lowpass characteristic, the phase delay and amplitude error of the estimated BEMF increase with the increment of the fundamental frequency. [83, 84, 109].

Moreover, for a low- or medium-speed PMSM, the LESO parameter often selects a lower bandwidth to adapt to the situation where the signal is weak and the noise is greatly affected. However, for high-speed PMSM, the dynamic change of the motor is fast, the amplitude of the BEMF is large, and it is difficult for the low-bandwidth observer to track the fast dynamic change, resulting in phase lag, estimation delay, and even instability. To overcome this issue, a new CHESO for high-speed SPMSM is proposed.

4.4 Proposed CHESO for High-speed SPMSMs

4.4.1 High-order ESO for BEMF Estimation

Conventional LESO only estimates the BEMF e_α and e_β, assuming that its dynamics change more slowly (i.e. $\dot{e}_\alpha \approx 0$ and $\dot{e}_\beta \approx 0$). The first-order derivatives of the BEMF e_α and e_β reflect the changing trend of BEMF. By estimating these derivatives, high-order ESO can respond faster to changes in the BEMF, thereby reducing the phase delay.

Compared to the conventional LESO, high-order extended state observer (HESO) increases the state variables of $\dot{e}_\alpha$ and $\dot{e}_\beta$, which enables a more accurate description of the dynamic change

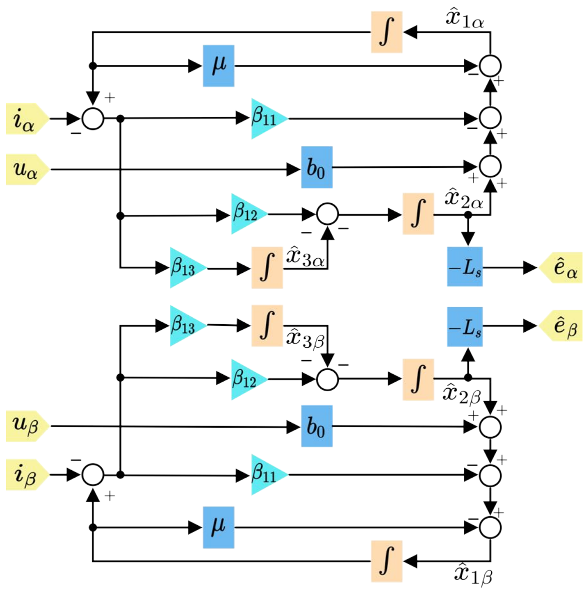

Fig. 4.6: The diagram of the first level HESO..

in BEMF, especially in scenarios with high speed and rapid dynamic change. By performing derivative operations on (3.2), the first-order derivative $\dot{e}_\alpha$ and $\dot{e}_\beta$ of the BEMF can be expressed as:

$$\begin{cases} \dot{e}_\alpha = -\dot{\omega}_e \psi_f \sin(\theta_e) - \omega_e^2 \psi_f \cos(\theta_e) \\ \dot{e}_\beta = \dot{\omega}_e \psi_f \cos(\theta_e) - \omega_e^2 \psi_f \sin(\theta_e) \end{cases} \tag{4.6}$$

By extending the order of (4.4), the HESO can be expressed as

$$\begin{cases} \boldsymbol{e}_{11} = \hat{\boldsymbol{x}}_1 - \boldsymbol{x}_1 \\ \dot{\hat{\boldsymbol{x}}}_1 = \hat{\boldsymbol{x}}_2 + b_0 \boldsymbol{u}_0 + u\hat{\boldsymbol{x}}_1 - \beta_{11} \cdot \boldsymbol{e}_{11} \\ \dot{\hat{\boldsymbol{x}}}_2 = \hat{\boldsymbol{x}}_3 - \beta_{12} \cdot \boldsymbol{e}_{11} \\ \dot{\hat{\boldsymbol{x}}}_3 = -\beta_{13} \cdot \boldsymbol{e}_{11} \end{cases} \tag{4.7}$$

where $\boldsymbol{x}_3 = [\dot{e}_\alpha, \dot{e}_\beta]$, β_{11}, β_{12} and β_{13} are the gains of observer. The structure diagram of the proposed HESO for BEMF estimation is shown in Fig. 4.6, where the ($\int$) represents the integral operator.

Rotor position can be calculated by using a quadrature PLL within the first level. The normalized $\hat{e}_\alpha$ and $\hat{e}_\beta$ are the inputs, and the output of PLL is the estimated rotor position. The diagram of

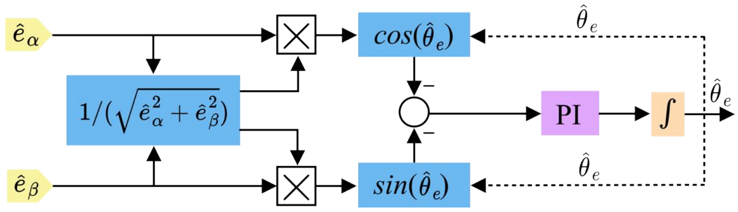

Fig. 4.7: The diagram of a normalized quadrature phase-locked loop.

normalized quadrature PLL is shown in Fig. 4.7. The error of the phase detector can be expressed as

$$e_{PLL} = -\hat{e}_\alpha \cos\hat{\theta}_e - \hat{e}_\beta \sin\hat{\theta}_e \tag{4.8}$$

At high-speed regions, the PLL is critical for accurate position estimation, primarily due to its robust phase-tracking and filtering capabilities. Although ESO or other direct estimation methods can effectively capture the fundamental characteristics of BEMF, these approaches inherently exhibit sensitivity to measurement noise and harmonic distortions, especially under high-speed conditions. As speed increases, even slight phase lag or estimation error becomes significantly magnified, adversely affecting control precision and stability. Therefore, the PLL remains essential in High-speed SPMSM sensorless control.

4.4.2 CHESO for High-speed SPMSM Sensorless Control

In this section, a two-level CHESO architecture is proposed for high-speed SPMSM sensorless control, so the estimation task is divided into two parts. At the first level, the ESO is dedicated to estimating the fast-changing BEMF with a high bandwidth. At the second level, the ESO uses the first-level output to estimate the rotor position, speed, and disturbances.

According to the (3.3), the mathematical model of second-level HESO can be expressed as follows:

$$\begin{cases} e_{21} = \hat{\theta}_e - \theta_e \\ \dot{\hat{\theta}}_e = \hat{\omega}_e + \beta_{21} e_{21} \\ \dot{\hat{\omega}}_e = (P_n/J)\left(T_e - \hat{T}_L - B\omega_e\right) + \beta_{22} e_{21} \\ \dot{\hat{T}}_L = (J/P_n)\,\beta_{23} e_{21} \end{cases} \tag{4.9}$$

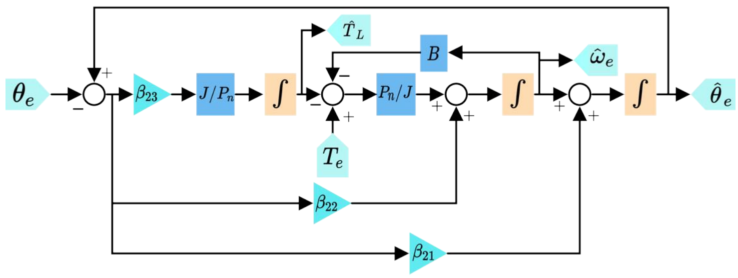

Fig. 4.8: The diagram of second level HESO for estimations.

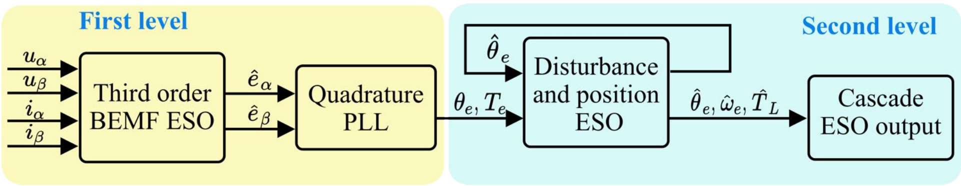

Fig. 4.9: Structure of two-level cascade high-order ESO.

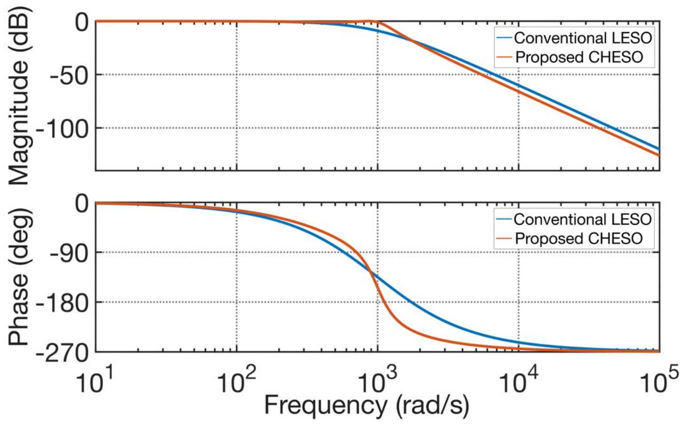

Fig. 4.10: Comparison of Bode diagram between conventional ESO and Cascade high-order ESO.

where e_{21} is the estimation error of θ_e. P_n is the number of pole pairs. β_{21}, β_{22} and β_{23} are the gains of observer. The diagram of the second level HESO is shown in Fig. 4.8. The structure of a two-level CHESO is shown in Fig. 4.9.

Although increasing the observer bandwidth can enhance dynamic tracking performance, it raises sensitivity to sampling noise and high-frequency disturbances. The proposed CHESO structure effectively manages this trade-off through a multilayered approach. By independently tuning each observer's bandwidth and leveraging the cascade design, the system achieves both high estimation accuracy and strong noise immunity across the full operating range. The Bode diagram of conventional LESO and CHESO is presented in Fig. 4.10. Compared with the conventional LESO, the HESO is superior in the high-frequency region both in bandwidth and roll-off speed.

Table 4.1: Summary of Different Roles of PLL and HESO.

Level of Estimation	Methodology	Primary Role	Estimation Focus	Dynamics Speed
first-level	PLL	accurate electrical angle tracking	electrical angle, noise suppression	fast electrical dynamics
second-level	HESO	mechanical dynamics estimation, disturbance rejection	mechanical angle, speed, load torque, disturbances	slower mechanical dynamics

In the two-level CHESO structure, the PLL in the first level and the HESO in the second level serve fundamentally distinct but complementary roles in the rotor position estimation process. The roles of the PLL at the first level are accurately tracking the instantaneous electrical phase of BEMF, and filtering out high-frequency noise and harmonic disturbances to provide continuous electrical angle. Moreover, the PLL outputs a precise and robust electrical angle which serves as a stable reference for subsequent processes.

The second-level HESO focuses on estimating the mechanical angular velocity, mechanical angle, and load torque based on the input provided by the first-level PLL. The slower mechanical dynamics can be captured effectively, which enhances system robustness. The second-level HESO provides estimated load torque and mechanical speed for adaptive feedforward control strategies, improving speed-loop accuracy and torque-loop performance through feedforward compensation. A comparison of the roles is shown in the Table 4.1.

Therefore, the HESO and PLL at the first level ensure accurate, high-speed tracking of electrical angles, crucial at high speeds. The HESO in the second level is dedicated to accurately estimating slower mechanical states and load torque dynamics, significantly enhancing robustness and disturbance rejection. This functional division enhances high-performance position estimation and control accuracy, especially in HSPMSM sensorless control systems.

4.4.3 Adaptive Feedforward Control

To enhance the robust performance of high-speed SPMSM for load mutations, a feedforward compensation control is employed, combined with real-time observation and load compensation through the second-level HESO to achieve speed fluctuation suppression.

The load torque feedforward compensation is to add the estimated load torque T_L to the electromagnetic torque reference $T_{e,\mathrm{ref}}$ and use the corrected reference T_e^* as the input of current controller, which can be expressed as

$$T_e^* = T_{e,\mathrm{ref}} + T_L \tag{4.10}$$

However, for the direct compensation method, the value of load torque is fixed, and it may lead to a poor dynamic response in scenarios where the load changes rapidly. Therefore, to adapt to the application scenarios of high-speed SPMSM, such as FESS, it is necessary to combine the adaptive feedforward compensation control strategy to dynamically adjust the compensation amount through adaptive law to quickly respond to load changes, thereby improving the dynamic performance of the system.

Feedforward compensation based on adaptive adjustment can be expressed as

$$T_e^* = T_{e,\mathrm{ref}} + \hat{T}_L + \Delta T_L \tag{4.11}$$

According to (3.3), the adaptive feedforward compensation amount needs to be designed so that the system can quickly track the reference speed and maintain stability and good dynamic performance when the load torque changes. The estimation error of torque load can be defined as

$$e_T = \hat{T}_L - T_L \tag{4.12}$$

To ensure the stability of the adaptive compensation system, define a Lyapunov function as a positive definite function of the error

$$V = \frac{1}{2} e_T^2 \tag{4.13}$$

Calculate the time derivative of the Lyapunov function

$$\dot{V} = e_T \dot{e}_T \tag{4.14}$$

Considering that the real load torque T_L is unknown but typically slow-varying in a short period. To ensure the stability and convergence of the system, define $\dot{\hat{T}}_L$ as:

$$\dot{\hat{T}}_L = -\gamma e_\omega \tag{4.15}$$

Thus,

$$\dot{e}_T = -\gamma e_\omega \tag{4.16}$$

where γ is the adaptive gain, and $e_\omega = \omega_r - \omega_{ref}$ is the speed error.

Substitute (4.16) into (4.14), then it can be expressed as

$$\dot{V} = e_T \dot{e}_T = e_T(-\gamma e_\omega) = -\gamma e_T e_\omega \tag{4.17}$$

From the adaptive law, the compensation adjustment ΔT_L can be expressed as the integral of the adaptive law

$$\Delta T_L = \int \dot{\hat{T}}_L dt = -\gamma \int e_\omega dt \tag{4.18}$$

Thus, the adaptive compensation for the load torque is dynamically updated based on the integrated speed error:

$$T_e^* = T_{e,ref} + \hat{T}_L - \gamma \int e_\omega dt \tag{4.19}$$

The control diagram of the proposed CHESO with adaptive feedforward compensation is presented in Fig. 4.11, where K_t is the torque constant. The performance metrics used throughout Chapters 4 and 5 are defined in Table 4.2 to ensure consistent benchmarking.

4.5 Stability and Robustness Analysis of CHESO

In CHESO architecture, the stability analysis involves two stages which are individual level analysis and cascade system analysis.

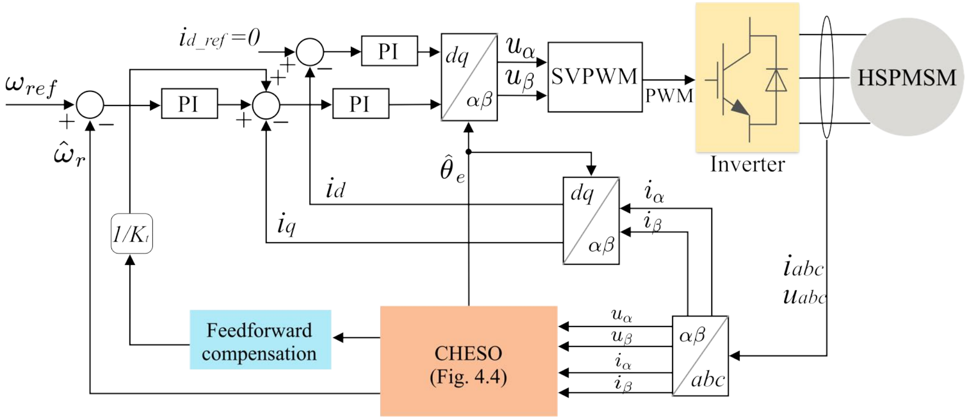

Fig. 4.11: Control diagram of sensorless HSPMSM control based on the proposed CHESO.

Table 4.2: Benchmarking metrics and operating conditions used throughout Chapters 4–5.

Category	Metric	Definition	Unit	Reference tables
Sensorless accuracy	Average rotor position error	Mean absolute position error over steady-state operation	rad	Tables 4.7, 5.4
	Peak rotor position error	Maximum instantaneous position deviation	rad	Tables 4.7, 5.4
Speed performance	Speed error	Steady-state speed deviation from reference	r/min	Tables 4.7, 5.5
	Speed overshoot	Maximum transient speed deviation after load step	r/min	Table 5.5
Harmonic quality	BEMF error amplitude	Peak BEMF estimation error	Volts	Tables 4.7, 5.4
	Harmonic distortion	BEMF or phase current THD	%	Tables 5.4, 5.5
Robustness tests	Parameter mismatch	R_s, L_s, ψ_f variation relative to nominal	%	Table 4.4
Operating region	FW operating point	Speed and control mode (MTPA / FW)	r/min	Tables 5.4 5.5
Current ripple	Peak-to-peak i_d	$max(i_d) - min(i_d)$ evaluated in steady state	A	Table 5.5
	Peak-to-peak i_q	$max(i_q) - min(i_q)$ evaluated in steady state	A	Table 5.5

4.5.1 Individual Stability of HESO and PLL

First, the stability analysis of the individual HESO is presented. According to (4.7), the error and HESO equations in the frequency domain can be expressed as

$$E_{11}(s) = \hat{X}_1(s) - X_1(s) \tag{4.20}$$

$$\begin{cases} s\hat{X}_1(s) = \hat{X}_2(s) + b_0 U_\alpha(s) + \mu X_1(s) - \beta_{11} E_{11}(s) \\ s\hat{X}_2(s) = \hat{X}_3(s) - \beta_{12} E_{11}(s) \\ s\hat{X}_3(s) = -\beta_{13} E_{11}(s) \end{cases} \tag{4.21}$$

The third equation of (4.21), can be expressed as

$$\hat{X}_3(s) = -\frac{\beta_3}{s} E_1(s) \tag{4.22}$$

Substitute (4.22) into second equation of (4.21), then it can be expressed as

$$\hat{X}_2(s) = -\frac{\beta_2 s + \beta_3}{s^2} E_1(s) \tag{4.23}$$

From Fig.4.6, the definition of BEMF can be expressed as

$$\hat{E}_\alpha(s) = -L_s \hat{X}_2(s) = \frac{L_s(\beta_2 s + \beta_3)}{s^2} E_1(s) \tag{4.24}$$

Then,

$$\frac{\hat{E}_\alpha(s)}{E_1(s)} = \frac{L_s(\beta_2 s + \beta_3)}{s^2} \tag{4.25}$$

The input-output relation for the first equation of (4.21) is

$$E_1(s) = \frac{1}{s + \mu + \beta_1}(\hat{X}_2(s) - E_\alpha(s)/L_s) \tag{4.26}$$

Then, substitute (4.23) into (4.26), it can be expressed as

$$E_1(s) = \frac{1}{s + \mu + \beta_1}\left(-\frac{\beta_2 s + \beta_3}{s^2} E_1(s) - \frac{E_\alpha(s)}{L_s}\right) \tag{4.27}$$

Thus,

$$\frac{E_1(s)}{E_\alpha(s)} = -\frac{s^2}{L_s(s^3 + (\mu + \beta_1)s^2 + \beta_2 s + \beta_3)} \tag{4.28}$$

Then, the desired transfer function is derived as

$$\frac{\hat{E}_\alpha(s)}{E_\alpha(s)} = \frac{\hat{E}_\alpha(s)}{E_1(s)} \cdot \frac{E_1(s)}{E_\alpha(s)} \tag{4.29}$$

According to (4.3) and (4.7), the transfer function of HESO can be obtained as

$$G_{\mathrm{HESO}}(s) = \frac{\hat{E}_\alpha(s)}{E_\alpha(s)} = -\frac{\beta_{12}s + \beta_{13}}{s^3 + (\mu + \beta_{11})s^2 + \beta_{12}s + \beta_{13}} \tag{4.30}$$

The stability of this system can be analyzed by inspecting the characteristic polynomial from the denominator of the transfer function. The characteristic polynomial can be expressed as

$$D(s) = s^3 + (\mu + \beta_{11})s^2 + \beta_{12}s + \beta_{13} \tag{4.31}$$

let $a_1 = \mu + \beta_{11}$, $a_2 = \beta_{12}$, $a_0 = \beta_{13}$, then the polynomial can be rewrite as

$$D(s) = s^3 + a_2 s^2 + a_1 s + a_0 \tag{4.32}$$

According to the Routh–Hurwitz criterion, the generalized Routh array for (4.32) is shown in Table 4.3.

Table 4.3: Routh Array for First-level HESO Polynomial.

s^3	1	β_{12}
s^2	$\mu + \beta_{11}$	β_{13}
s^1	$\frac{(\mu+\beta_{11})\beta_{12}-\beta_{13}}{\mu+\beta_{11}}$	0
s^1	β_{13}	0

The stability condition is the elements in the first column of the Routh table must be positive. Thus, the stability condition can be expressed as

$$\mu + \beta_{11} > 0, \beta_{13} > 0, (\mu + \beta_{11})\beta_{12} > \beta_{13}. \tag{4.33}$$

where μ, β_{11}, β_{13} are positive guaranteed. In other words, if the condition of $\beta_{11}\beta_{12} > \beta_{13}$ is satisfied, the characteristic polynomial explicitly has all poles in the left half-plane and the ESO is stable. According to the high-order ESO gains selection principle in [70, 102, 110, 111], and combined the results of theoretical analysis and actual testing, the following gain parameters are finally designed as

$$\beta_{11} = 3\omega_0, \beta_{12} = 3{\omega_0}^2, \beta_{13} = {\omega_0}^3. \tag{4.34}$$

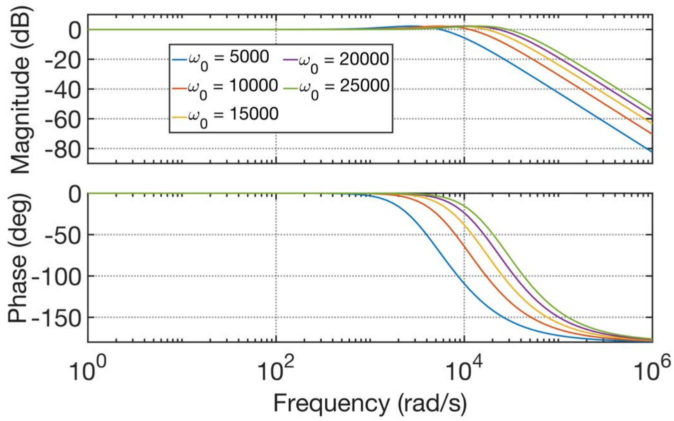

Fig. 4.12: Comparison of Bode diagram for different ω_0.

The frequency response of (5.23) for different observer bandwidths is illustrated in Fig. 4.12, As ω_0 increases from 1,000 rad/s to 5,000 rad/s, the bandwidth of the observer widens, shifting the magnitude and phase curves to higher frequencies indicating more accurate estimation at high-speed operating conditions.

Similarly, the second-level HESO can be analyzed using the same method. Define error variables explicitly as follows:

$$\begin{cases} e_{21} = \hat{\theta}_e - \theta_e \\ e_{22} = \hat{\omega}_e - \omega_e \\ e_{23} = \hat{T}_L - T_L \end{cases} \tag{4.35}$$

According to (4.9), the second-level HESO state-space error can be expressed as

$$\begin{cases} \dot{e_{21}} = e_{22} + \beta_{21}e_{21} \\ \dot{e_{22}} = (P_n/J)\,(-e_{23} - Be_{22}) + \beta_{22}e_{21} \\ \dot{e_{23}} = (J/P_n)\,\beta_{23}e_{21} \end{cases} \tag{4.36}$$

Define state error vector as $E_{HESO2} = [e_{21}, e_{22}, e_{23}]$, and the state-space form of the error dynamics can be expressed as:

$$\dot{E}_{HESO2} = A_{HESO2}E_{HESO2} \tag{4.37}$$

where the state matrix A_{HESO2} can be express as:

$$A_{HESO2} = \begin{bmatrix} \beta_{21} & 1 & 0 \\ \beta_{22} & -(P_nB)/J & -P_n/J \\ (J/P_n)\beta_{23} & 0 & 0 \end{bmatrix} \tag{4.38}$$

By calculating the characteristic polynomial of (4.38), the characteristic equation can be expressed as

$$D(s) = s^3 + a_{22}s^2 + a_{21}s + a_{20} \tag{4.39}$$

where the coefficients are $a_{22} = (P_nB)/J - \beta_{21}$, $a_{21} = -\beta_{21}(P_nB)/J - \beta_{22}$, $a_{20} = \beta_{23}$. According to the Routh–Hurwitz criterion, the generalized Routh array and stability condition for (4.39) can be obtained. Then, the following gain parameters are finally designed as

$$\beta_{21} = 2\omega_1, \beta_{22} = 2{\omega_1}^2, \beta_{23} = {\omega_1}^3. \tag{4.40}$$

where the ω_1 is the observer bandwidth of second-level HESO.

The PLL uses a PI controller to update the position estimate. In the linearized model, the closed-loop dynamics of PLL can be expressed as a second-order system. The characteristic polynomial can be obtained as

$$s^2 + K_p s + K_i = 0 \tag{4.41}$$

where K_p and K_i are the PI controller gains, For the PLL to be stable, both roots of the characteristic polynomial must have negative real parts. The stable conditions are $K_p > 0$ and $K_i > 0$.

The PI controller gains in the PLL determine its bandwidth and have a direct impact on the accuracy of rotor position estimation. To achieve precise and stable estimation, the gains K_p and K_i should be selected based on a desired natural frequency ω_n of the PLL, thereby balancing the trade-off between rapid dynamic response and effective noise suppression. Under practical conditions, if phase tracking exhibits noticeable lag, increasing ω_n can improve responsiveness. Conversely, if the system is overly sensitive to noise, reducing ω_n helps mitigate this effect by lowering the controller gains accordingly.

4.5.2 Cascade Stability Analysis

According to (4.7), define the error of the HESO for BEMF estimation

$$\begin{cases} e_{11} = \hat{x}_1 - x_1 \\ e_{12} = \hat{x}_2 - x_2 \\ e_{13} = \hat{x}_3 - x_3 \end{cases} \tag{4.42}$$

Considering the second-level HESO error dynamics, the errors can be defined as

$$\begin{cases} e_{21} = \hat{\theta}_e - \theta_e \\ e_{22} = \hat{\omega}_e - \omega_e \\ e_{23} = \hat{T}_L - T_L \end{cases} \tag{4.43}$$

Then, a global state error vector combining both levels can be expressed as

$$e_{global} = [e_{11}, e_{12}, e_{13}, e_{PLL}, e_{21}, e_{22}, e_{23}]^T \tag{4.44}$$

According to ESO theory [112], the cascade stability can be guaranteed when each stage in the cascade holds the input-to-output state stable, and the entire cascaded system is stable. While each stage of stability has been proven in individual stability analyses.

4.5.3 Parameter Robustness Analysis

To demonstrate the parameter robustness of the proposed CHESO, a response surface analysis under parameter mismatch conditions is conducted. Figs. 4.13–4.15 present simulation results illustrating the impact of parameter deviations on the average position estimation error across different operating speeds. The ranges of mismatch settings are listed in Table 4.4.

Table 4.4: Parameter mismatch ranges setting.

Parameters	Lower boundary (Ratio to nominal)	Upper boundary (Ratio to nominal)
Resistance (R_s)	80%	120%
Inductance (L_s)	80%	120%
Flux linkage (ψ_f)	80%	120%

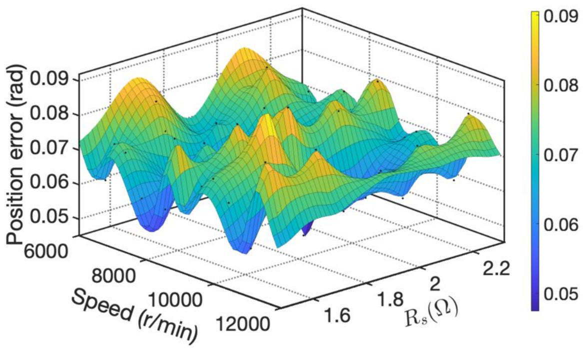

Fig. 4.13: Simulation results of resistance mismatch for the position estimation error at different speeds.

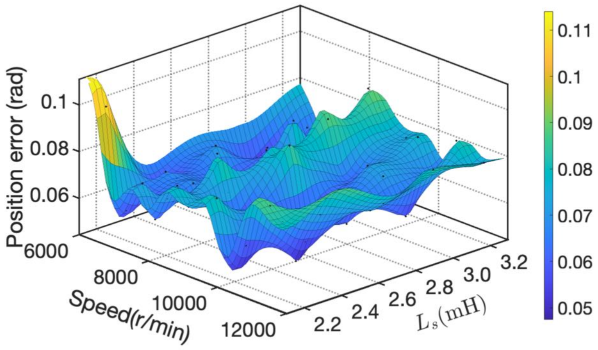

Fig. 4.14: Simulation results of inductance mismatch for the position estimation error at different speeds.

The parameter values used in the simulation correspond to those of the tested high-speed SPMSM described in Section 4.6. In Figs. 4.13, 4.14, and 4.15, the stator resistance R_s, inductance L_s, and flux linkage ψ_f are varied from 80% to 120% of their nominal values. As shown in Fig. 4.13, the position estimation error remains quite small across all speeds when resistance is varied, indicating strong robustness of the CHESO to resistance mismatch. Figs. 4.14 and 4.15 illustrate the performance under inductance and flux linkage mismatches, respectively, further confirming that the proposed CHESO maintains robust performance across a range of parameter mismatches.

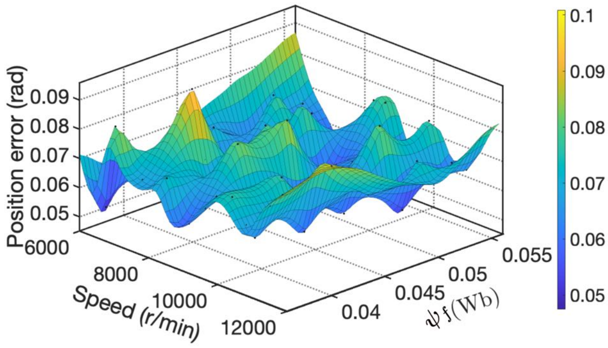

Fig. 4.15: Simulation results of flux linkage mismatch for the position estimation error at different speeds.

4.6 Experimental Test and Results

An overview of the experimental test platform is shown in Fig. 4.16. A small-scale HSPMSM test setup is built, consisting of a dSPACE MicroLabBox, interface boards, a three-phase inverter utilizing Infineon FF600R12ME4 modules, and a high-speed SPMSM test bench. To evaluate the real-time applicability of the proposed CHESO sensorless control method, the algorithm was implemented on a dSPACE MicroLabBox (DS1202), which integrates a Freescale P5020 dual-core PowerPC processor (2.0 GHz). All control tasks were executed at a switching frequency of 10 kHz. Runtime profiling using dSPACE ControlDesk revealed a task execution time of 69 µs per cycle, which is well within the 100 µs control deadline. The proposed observers and controllers are computationally lightweight and do not impose significant computing power constraints, making them suitable for real-time implementation on standard DSP and dSPACE platforms. Detailed specifications of the tested high-speed SPMSM are listed in Table 4.5, and the associated observer gains are summarized in Table 4.6.

In this section, the LESO is designed using a bandwidth-based tuning rule, with the observer bandwidth selected as a conservative multiple of the electrical fundamental frequency to balance estimation speed and noise sensitivity. The PI speed controller is tuned using conventional frequency-domain guidelines to ensure stable operation, adequate phase margin, and acceptable transient response over the tested speed range. This baseline configuration aligns with common practice in PI-based sensorless PMSM control and provides a fair and realistic reference for evaluating the conventional LESO and the proposed CHESO.

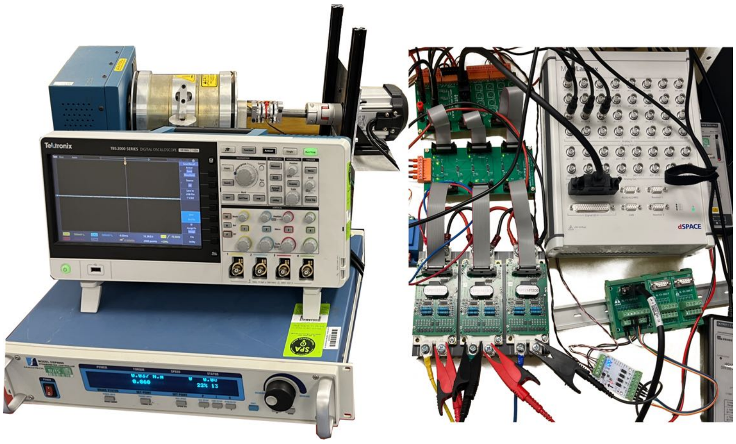

Fig. 4.16: Overview of testbench and drive system setup.

Table 4.5: Parameters of high-speed SPMSM System

Parameters	Unit	Value
Rated Speed	r/min	12,000
Rated torque	N.m	0.375
Rated Power	kW	0.45
Rated voltage	V	311
Rated current	A	3.5
No. of pole pairs	-	3
Stator resistance	Ω	1.9
d-axis inductance (L_s)	mH	2.7
q-axis inductance(L_s)	mH	2.7
Magnet flux linkage	Wb	0.045

Table 4.6: Observer Parameters of ESO

Parameters	Value	Parameters	Value
l_1	4.01e+04	l_2	8.38e+08
β_{11}	3.07e+04	β_{21}	9.29e+03
β_{12}	7.10e+08	β_{21}	5.01e+07
β_{13}	6.69e+12	β_{21}	1.25e+11

4.6.1 Position Estimation Results

In this section, the rotor position estimation performance of the conventional LESO and the proposed HESO are comparatively evaluated. Initially, the high-speed SPMSM operates under speed control mode without load conditions. Figs. 4.17-4.26 illustrate the actual and estimated

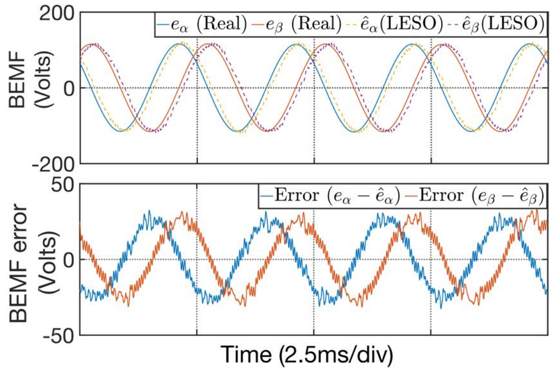

Fig. 4.17: BEMF estimation of conventional LESO at 8,000 r/min without load.

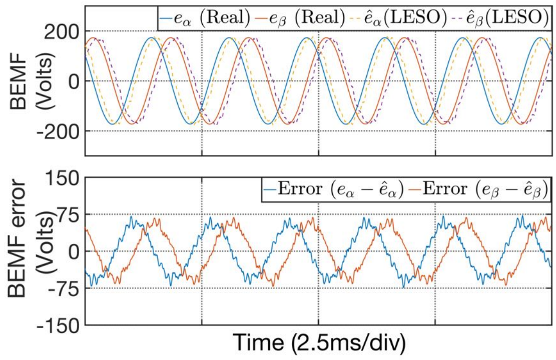

Fig. 4.18: BEMF estimation of conventional LESO at 12,000 r/min without load.

BEMF waveforms, rotor positions with corresponding estimation errors, and the BEMF harmonics obtained using the conventional LESO and the proposed HESO at speeds of 8,000 and 12,000 r/min, respectively.

In Figs. 4.17 and 4.18, the actual and estimated BEMF waveforms obtained using the conventional LESO are illustrated at 8,000 and 12,000 r/min, respectively. It is evident that the mean amplitude of BEMF estimation error increases with motor speed, reaching approximately 36 V at 8,000 r/min and 73 V at 12,000 r/min.

Conversely, as shown in Figs. 4.19 and 4.20, the proposed HESO significantly reduces the mean amplitude of BEMF estimation error to approximately 12.5 V and 28 V at 8,000 and 12,000 r/min, respectively. Thus, the BEMF estimation errors at these speeds are reduced by about 65% and 62%, respectively.

Regarding rotor position estimation, as demonstrated in Figs. 4.21 and 4.22, the position estimation error using the conventional LESO increases with motor speed, yielding mean errors of 0.33 rad

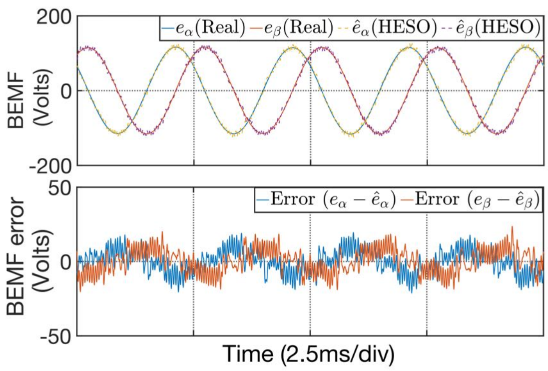

Fig. 4.19: BEMF estimation of HESO at 8,000 r/min without load.

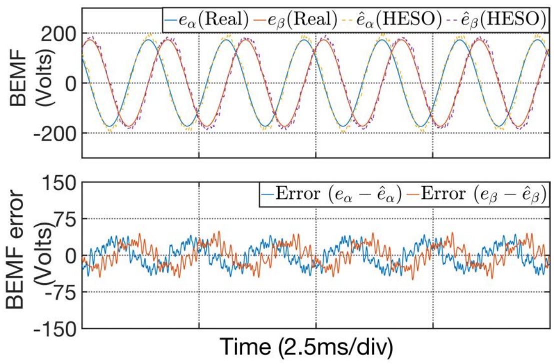

Fig. 4.20: BEMF estimation of HESO at 12,000 r/min without load.

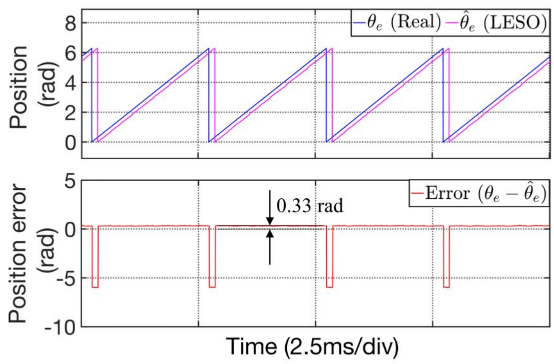

Fig. 4.21: Position estimation and position error of conventional LESO at 8,000 r/min without load.

at 8,000 r/min and 0.42 rad at 12,000 r/min. However, as depicted in Figs. 4.23 and 4.24, the proposed HESO significantly decreases the mean position estimation errors to 0.11 rad and 0.15 rad at the same respective speeds. Consequently, the rotor position estimation errors are reduced by approximately 66% at 8,000 r/min and 64% at 12,000 r/min. These rotor position estimation outcomes are consistent with the improvements observed in BEMF estimation accuracy.

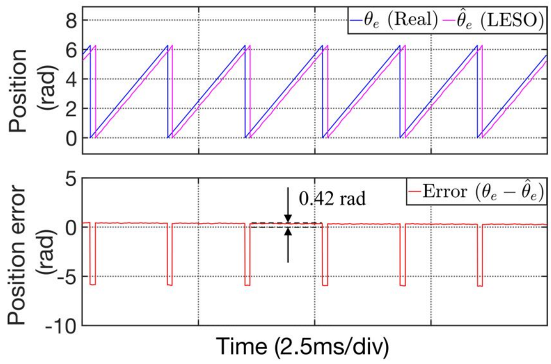

Fig. 4.22: Position estimation and position error of conventional LESO at 12,000 r/min without load.

Hence, compared with the conventional LESO, the proposed HESO substantially enhances position estimation accuracy in the sensorless control of high-speed SPMSMs.

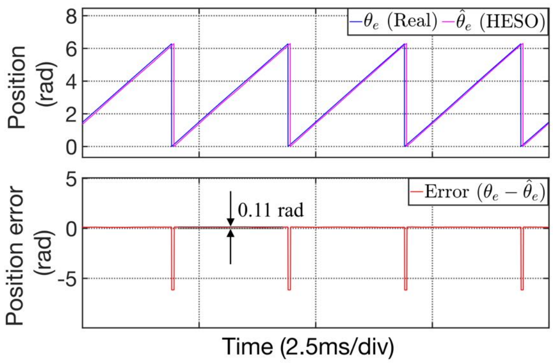

Fig. 4.23: Position estimation and position error of HESO at 8,000 r/min without load.

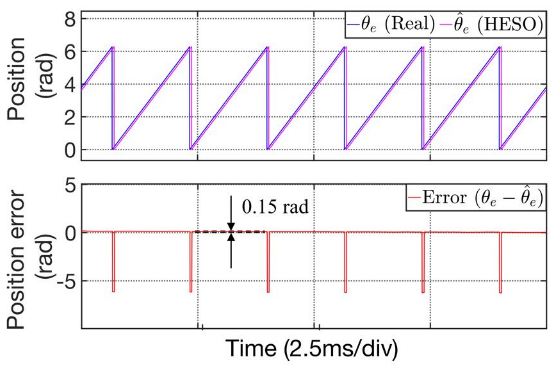

Fig. 4.24: Position estimation and position error of HESO at 12,000 r/min without load.

Additionally, Figs. 4.25 and 4.26 present a harmonic analysis of the α-axis BEMF estimated by the proposed HESO at 8,000 and 12,000 r/min, respectively. Compared with the conventional

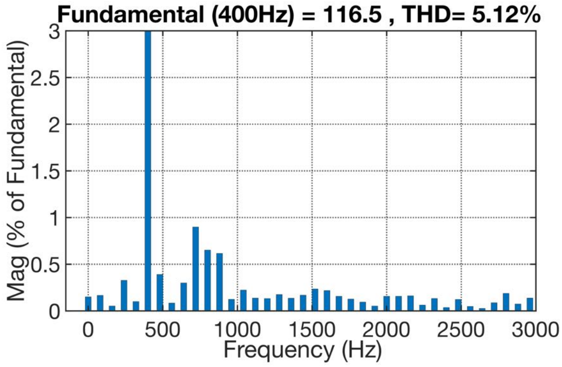

Fig. 4.25: FFT harmonic analysis of HESO at 8,000 r/min without load.

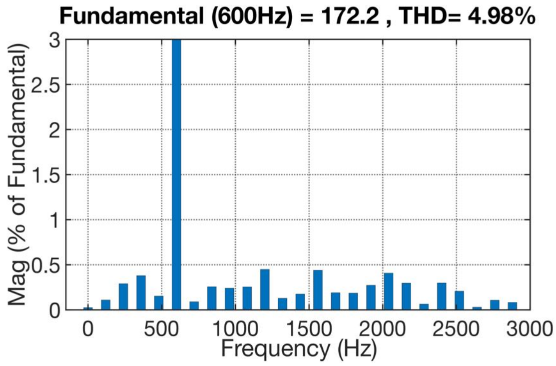

Fig. 4.26: FFT harmonic analysis of HESO at 12,000 r/min without load.

LESO results shown in Figs. 4.27 and 4.28, the total harmonic distortion (THD) values with the proposed HESO increased by approximately 1.28% at 8,000 r/min and 1.05% at 12,000 r/min. As indicated by the derivation equations presented in 4.6, the inclusion of second-order terms introduces additional nonlinearities, leading to increased harmonic components under high-speed operating conditions.

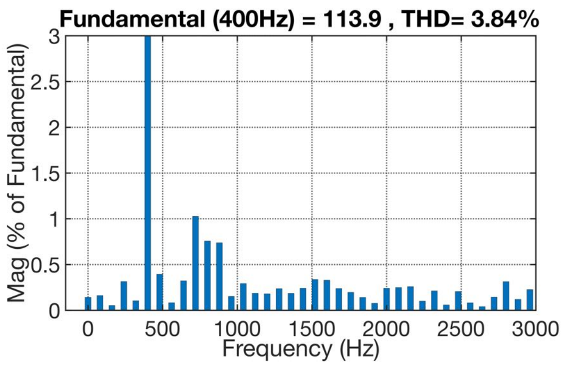

Fig. 4.27: FFT harmonic analysis of conventional LESO at 8,000 r/min without load.

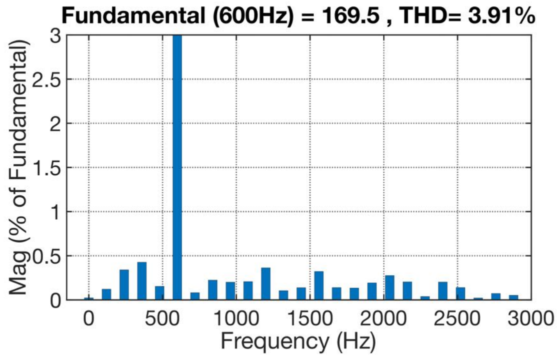

Fig. 4.28: FFT harmonic analysis of conventional LESO at 12,000 r/min without load.

Therefore, the enhanced accuracy achieved by the proposed HESO is accompanied by a slight increase in harmonic distortion due to heightened sensitivity to measurement noise and internal system nonlinearities. Nevertheless, compared with the conventional LESO, the proposed HESO considerably improves dynamic accuracy and reduces rotor position estimation errors by more effectively capturing rapid dynamic changes. The issues associated with measurement noise and internal nonlinearities can be mitigated through the disturbance estimation and feedforward control strategies discussed in the subsequent section.

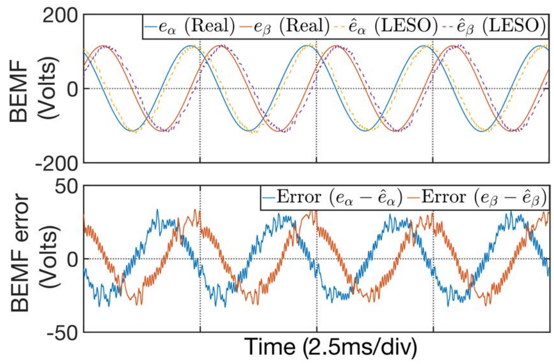

Fig. 4.29: BEMF estimation of conventional LESO at 8,000 r/min with rated load.

Secondly, the performance of the high-speed SPMSM is evaluated under speed control mode at the rated load. Figs. 4.29-4.38 illustrate the actual and estimated BEMF waveforms, rotor position with estimation errors, and speed estimation along with corresponding errors for the conventional LESO and the proposed HESO at 8,000 and 12,000 r/min, respectively. As shown in Figs. 4.29-4.32, and 4.33-4.36, the proposed HESO demonstrates superior BEMF and position estimation

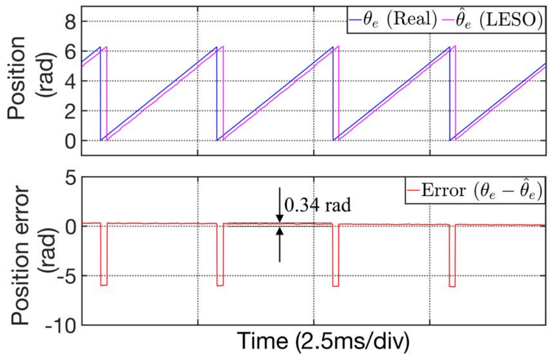

Fig. 4.30: Position estimation and position error of conventional LESO at 8,000 r/min with rated load.

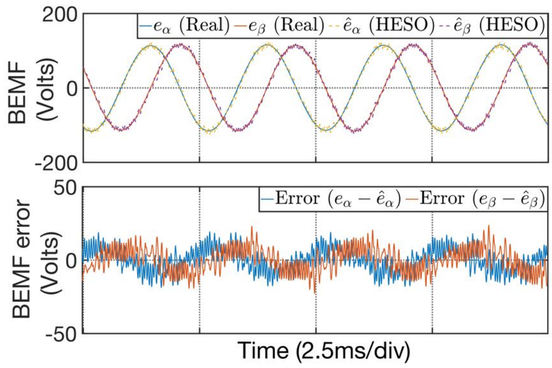

Fig. 4.31: BEMF estimation of HESO at 8,000 r/min with rated load.

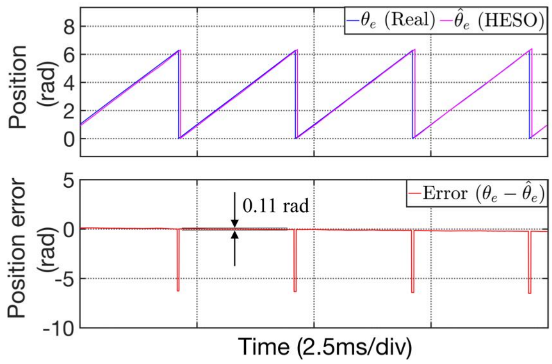

Fig. 4.32: Position estimation and position error of HESO at 8,000 r/min with rated load.

performance compared to the conventional LESO, consistent with the no-load results discussed previously. Hence, detailed analysis of these specific results is omitted here for conciseness.

Moreover, as depicted in Figs. 4.37 and 4.38, the speed estimation errors of the conventional LESO increase significantly with motor speed, exhibiting amplitudes of approximately 190 r/min and 355

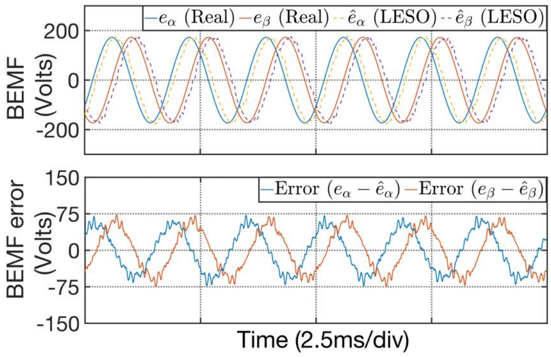

Fig. 4.33: BEMF estimation of conventional LESO at 12,000 r/min with rated load.

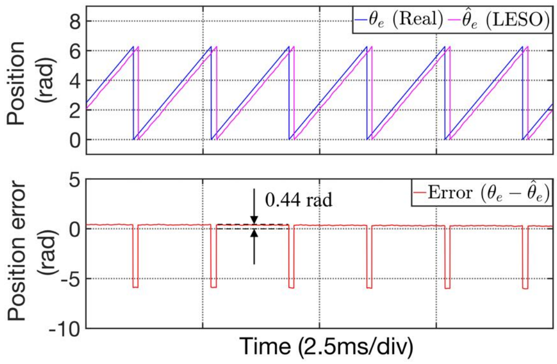

Fig. 4.34: Position estimation and position error of conventional LESO at 12,000 r/min with rated load.

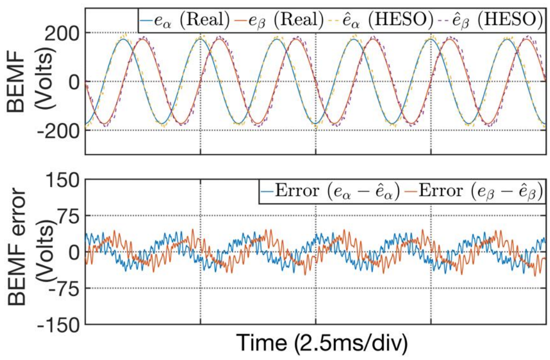

Fig. 4.35: BEMF estimation of HESO at 12,000 r/min with rated load.

r/min at 8,000 and 12,000 r/min, respectively. Conversely, the proposed HESO, as shown in Figs. 4.39 and 4.40, substantially reduces the amplitudes of speed estimation errors to around 40 r/min at 8,000 r/min and 55 r/min at 12,000 r/min.

Compared to the conventional LESO, the speed estimation noise with the proposed HESO is

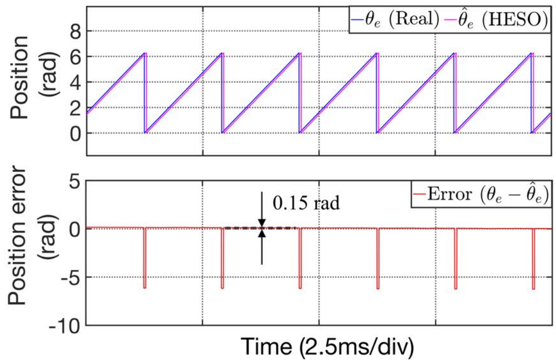

Fig. 4.36: Position estimation and position error of HESO at 12,000 r/min with rated load.

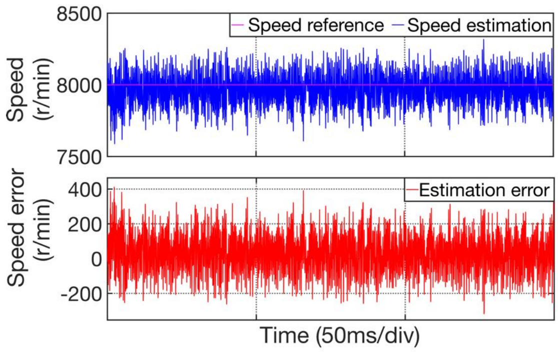

Fig. 4.37: Speed estimation and speed error of conventional LESO at 8,000 r/min with rated load.

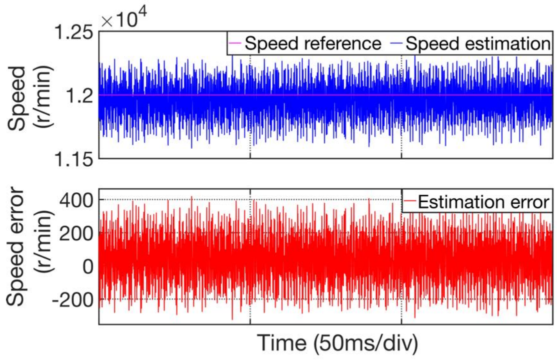

Fig. 4.38: Speed estimation and speed error of conventional LESO at 12,000 r/min with rated load.

effectively diminished due to its two-level cascade structure. This architecture allows independent tuning of each observer level with appropriate observer gains, ensuring accurate tracking of fast motor dynamics without excessively amplifying measurement noise, thereby achieving an optimal balance between estimation accuracy and noise suppression. The results comparison for the conventional LESO and the proposed HESO is listed in Table 4.7. The metrics reported here

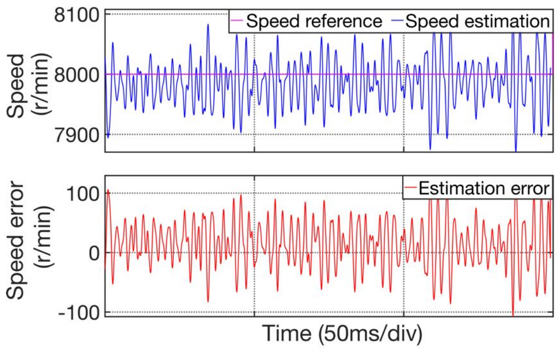

Fig. 4.39: Speed estimation and speed error of HESO at 8,000 r/min with rated load.

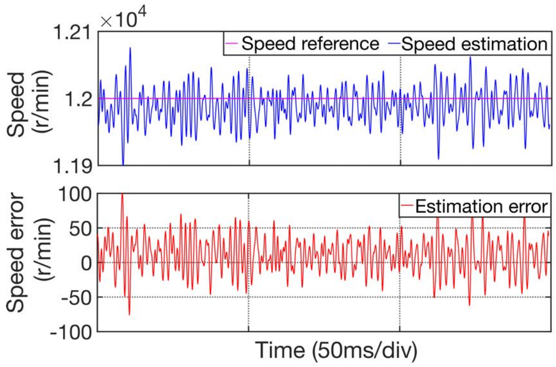

Fig. 4.40: Speed estimation and speed error of HESO at 12,000 r/min with rated load.

correspond to the sensorless accuracy and speed performance definitions in Table 4.2.

Under identical operating conditions, the HESO reduces the average rotor position error by approximately 64–66% and the steady-state speed error by more than 75% compared with the conventional LESO, as summarised in Table 4.7.

Table 4.7: The comparison for different observer methods.

Speed (r/min)	Items	LESO	HESO
8,000	BEMF error amplitude (Volts)	36	12.5 (↓ 65%)
8,000	Average rotor position errors (rad)	0.33	0.11 (↓ 66%)
8,000	Speed error (r/min)	190	40
12,000	BEMF error amplitude (Volts)	73	28 (↓ 63%)
12,000	Average rotor position errors (rad)	0.42	0.15 (↓ 64%)
12,000	Speed error (r/min)	355	55

4.6.2 Transient Process and Parameter Mismatch Analysis

In this section, the transient performance of the conventional LESO and the proposed CHESO is comparatively evaluated through a speed step-change test conducted under rated load conditions. Furthermore, the parameter robustness of the proposed method is evaluated under varying load conditions.

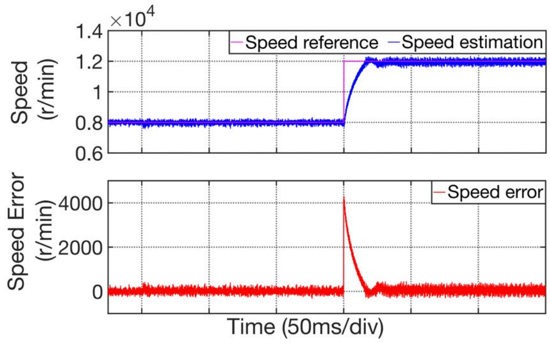

Fig. 4.41: Speed estimation and speed error of conventional LESO at speed step-change test.

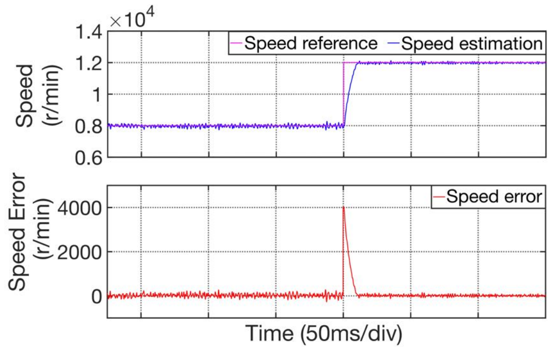

Fig. 4.42: Speed estimation and speed error of HESO at speed step-change test.

In Fig. 4.41, the reference speed, estimated speed, and speed estimation error for the conventional ESO are presented. Compared to the conventional LESO, the proposed CHESO demonstrates superior performance in both steady-state and transient conditions, exhibiting a faster response, reduced speed estimation errors, and diminished oscillations, as illustrated in Fig. 4.42.

Additionally, Figs. 4.43 and 4.44 show the d- and q-axis currents and three-phase currents for the conventional LESO, respectively. In Figs. 4.45 and 4.46, the d- and q-axis currents of the conventional LESO and the proposed CHESO are compared. The results clearly indicate

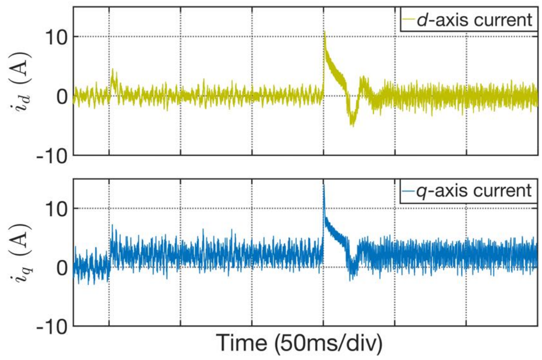

Fig. 4.43: The d- and q-axis currents of the conventional LESO at speed step-change test.

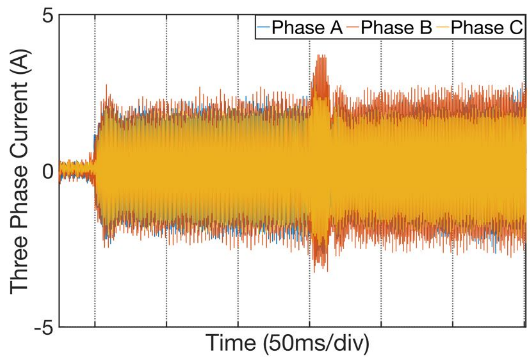

Fig. 4.44: Three-phase currents of conventional LESO at speed step-change test.

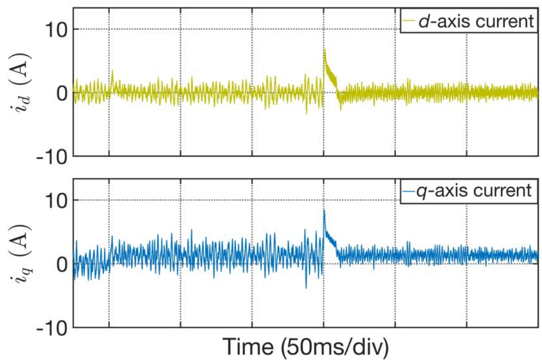

Fig. 4.45: The d- and q-axis currents of the HESO at speed step-change test.

that, compared to the conventional LESO, the proposed CHESO achieves enhanced accuracy and reduced current noise, attributed to its improved position estimation.

Furthermore, as depicted in Fig. 4.44, the three-phase currents exhibit pronounced oscillations during load changes and speed step variations when controlled by the conventional LESO, whereas these oscillations are significantly reduced with the proposed CHESO, as shown in Fig. 4.46.

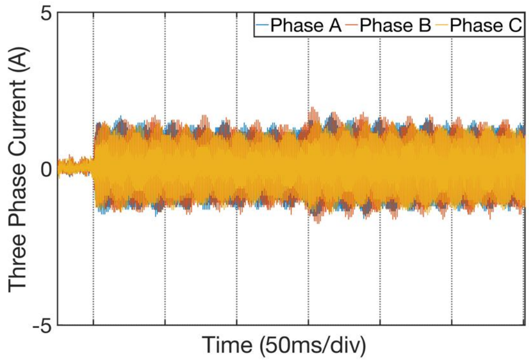

Fig. 4.46: Three-phase currents of conventional LESO at speed step-change test.

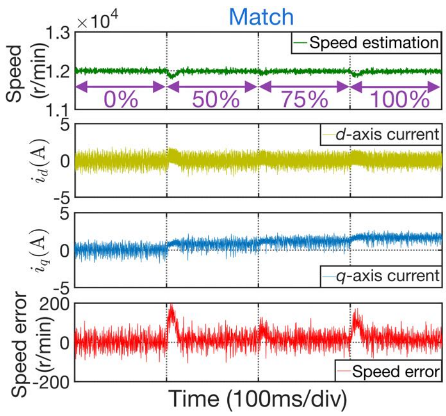

Fig. 4.47: The match of parameters under varying load torque.

Moreover, due to the higher position estimation errors associated with the conventional ESO, the amplitude of the three-phase currents is noticeably larger compared to that obtained with the proposed CHESO.

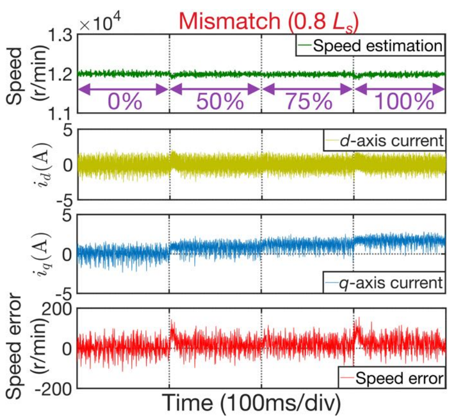

Fig. 4.48: The mismatch 0.8 L_s under varying load torque.

The parameter mismatch tests are presented in Figs. 4.47-4.52 . In Figs. 4.48-4.52, the proposed method maintains stable operation under various parameter mismatch scenarios, including $L_{so} = 0.8L_s$, $L_{so} = 1.2L_s$, $R_{so} = 0.8R_s$, $R_{so} = 1.2R_s$, and $\psi_{fo} = 0.8\psi_f$, even as the load torque increases from 0 to 100% of rated torque. These results indicate that parameter mismatches have little impact on the performance of the proposed CHESO. Furthermore, the proposed method demonstrates a rapid dynamic response to abrupt load variations, effectively tracking sudden torque commands. Compared to the conventional LESO shown in Fig. 4.38, the proposed CHESO results in smaller speed errors, even under variable load conditions.

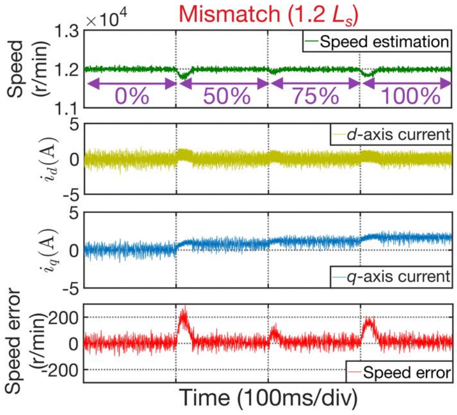

Fig. 4.49: The mismatch 1.2 L_s under varying load torque.

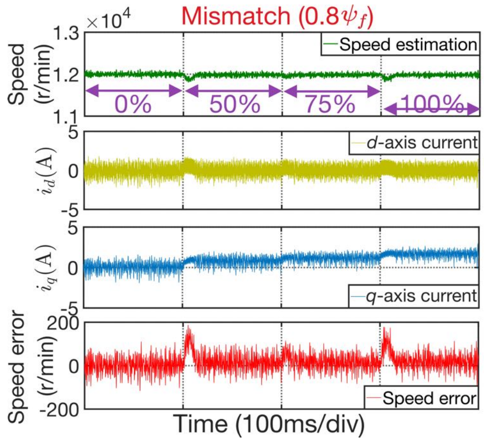

Fig. 4.50: The mismatch 0.8 ψ_f under varying load torque.

To validate the operational speed range, the proposed method was evaluated starting from a low-speed condition, with the corresponding estimation performance included. The relative speed estimation error, defined as the deviation between the estimated speed and the reference speed, normalized to the reference, is used to assess estimation accuracy across different speeds. As shown in Fig. 4.53, the lowest tested speed in the experiment is 2000 r/min. The results indicate that

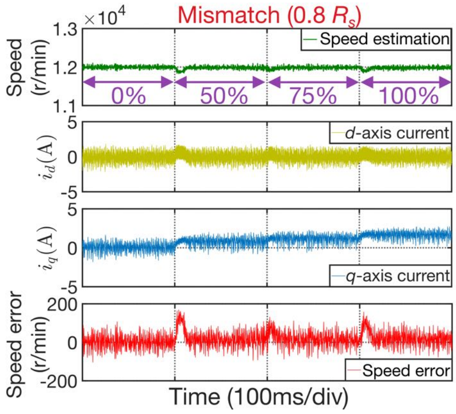

Fig. 4.51: The mismatch 0.8 R_s under varying load torque.

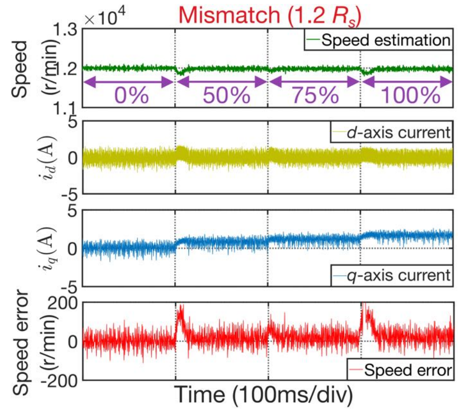

Fig. 4.52: The mismatch 1.2 R_s under varying load torque.

the relative speed estimation error is highest at low speeds and decreases as the motor accelerates, which is consistent with the characteristics of HESO-based sensorless control. While the proposed method is optimized for high-speed operation, it remains functional in the lower-speed region.

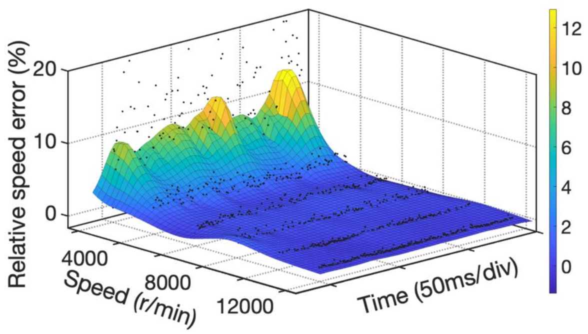

Fig. 4.53: Performance analysis of the relative speed estimation error across a range of operating speeds.

4.6.3 Adaptive Compensation and Load Estimation

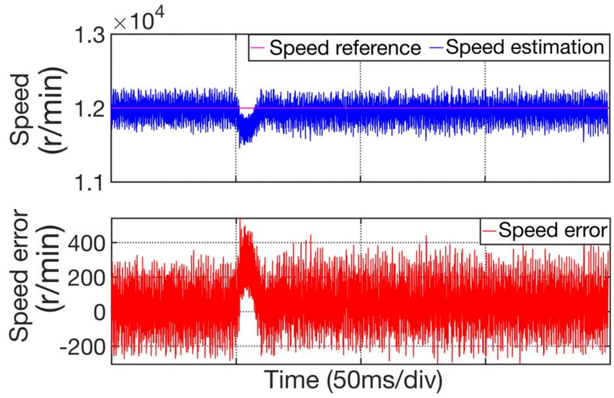

Fig. 4.54: Speed response of conventional LESO at load disturbance.

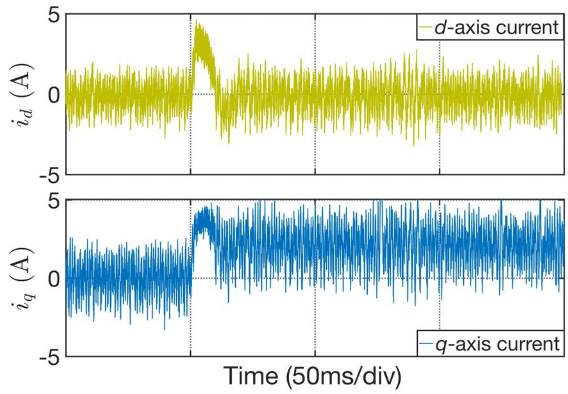

Fig. 4.55: Speed response of CHESO with feedforward control at load disturbance.

In this section, adaptive feedforward compensation and load torque estimation performance are evaluated under conditions of rated load applied at 12,000 r/min. Fig. 4.54 shows the speed reference, estimated speed, and speed estimation error for the conventional LESO, indicating a maximum speed error of approximately 490 r/min upon the application of rated load. Consistent with the results presented earlier, the conventional LESO exhibits significant noise in both speed estimation and the d- and q-axis currents as shown in Fig. 4.55, primarily due to the high observer gains. This issue highlights a critical drawback of the conventional LESO when applied to high-speed SPMSM control.

In comparison, as illustrated in Fig. 4.56, the proposed control strategy demonstrates a faster response to load disturbances and substantially reduced speed deviations. Additionally, Fig. 4.57

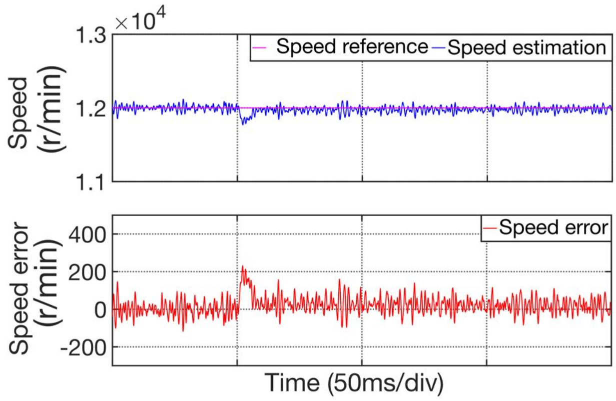

Fig. 4.56: The d- and q-axis currents of the conventional LESO at load disturbance.

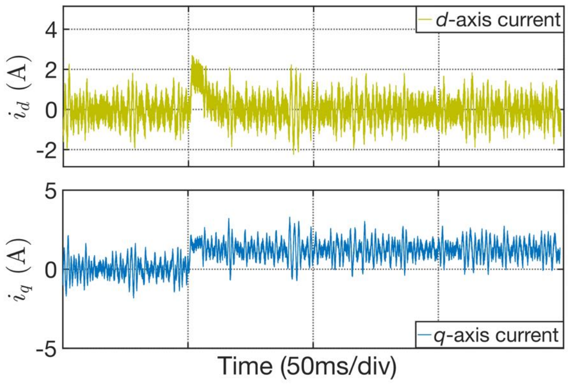

Fig. 4.57: The d- and q-axis currents of the CHESO with feedforward control at load disturbance.

illustrates that the proposed control strategy effectively reduces noise in the $d-$ and $q-$axis currents, while also lowering their amplitudes due to improved accuracy in rotor position estimation.

4.7 Summary

In this chapter, a cascade high-order extended state observer (CHESO) was proposed to enhance rotor position estimation accuracy and improve the speed control performance of sensorless high-speed SPMSM drives. The detailed design procedures of the two-level CHESO, along with its performance characteristics, individual-level stability, and cascade system stability analyses, were presented. Compared with the conventional LESO, the proposed CHESO significantly reduced rotor position estimation errors and improved speed estimation accuracy in wide-range speed estimation. Furthermore, an adaptive feedforward control strategy was employed to enhance the dynamic response and disturbance rejection capabilities of the high-speed SPMSM drive system. Experimental validation, including steady-state rotor position estimation, transient performance evaluation, and adaptive feedforward compensation tests, demonstrated the effectiveness and improvements offered by the proposed sensorless control strategy for high-speed SPMSMs.

Chapter 5

Improved Sensorless Control of High-speed SPMSMs Based on SOGI-HESO in the FW Region

5.1 Introduction

This chapter addresses the remaining challenges of robustness and estimation accuracy for high-speed SPMSM drives operating in the flux-weakening (FW) region, where inverter nonlinearities, current harmonics, and measurement noise degrade sensorless performance. Building on the sensorless estimation framework developed in Chapter 4, a second-order generalized integrator (SOGI)–high-order extended state observer (HESO) is proposed to suppress harmonics and extend estimation bandwidth. An adaptive linear active disturbance rejection control (ALADRC) strategy is then integrated to improve dynamic response and disturbance rejection, completing a robust sensorless control framework for wide-speed-range operation.

The proposed SOGI-HESO-based method is tailored for FW operation, where reduced flux linkage and stronger harmonics challenge conventional sensorless methods. To maintain a fair baseline, the conventional constant-voltage-constant-power (CVCP) method is adopted for the FW implementation. By improving BEMF estimation accuracy and enhancing speed loop robustness, the proposed strategy directly strengthens FW control within the standard CVCP framework. To further improve FW control performance, an ALADRC strategy with real-time bandwidth adjustment is implemented in the speed control loop. While retaining the benefits of conventional ADRC, the adaptive mechanism dynamically adjusts the controller bandwidth according to motor speed, effectively addressing the disturbances and parameter variations commonly encountered in high-speed SPMSM applications. This integrated approach results in improved control robustness and dynamic responsiveness across a wide operating range.

5.2 Conventional Sensorless and Flux-weakening Control of high-speed SPMSM

5.2.1 Flux-Weakening Control of HSPMSM

The $d-$ and $q-$axis voltage equations of the high-speed SPMSM can be expressed as

$$\begin{cases} u_d = R_s i_d + L_s \dot{i}_d - \omega_e L_s i_q \\ u_q = R_s i_q + L_s \dot{i}_d + \omega_e L_s i_q + \omega_e \psi_f \end{cases} \tag{5.1}$$

where u_d, u_q, i_d and i_q are the voltages and currents in the $dq-$frame. For HSPMSM driven by an inverter, due to the limitation of bus voltage and output capacity, the stator phase voltage amplitude and current amplitude need to meet the following requirements:

$$\begin{cases} u_d^2 + u_q^2 \leq U_{s,\max}^2 = (U_{dc}/\sqrt{3})^2 \\ i_d^2 + i_q^2 \leq I_{s,\max}^2 \end{cases} \tag{5.2}$$

where $U_{s,\max}$ is the voltage limit and $I_{s,\max}$ is the current limit. U_{dc} is the DC bus voltage. The resistance and inductance voltages can usually be ignored during high-speed operation. Then, the voltage equations can be simplified as

$$\begin{cases} u_d = -\omega_s L_s i_q \\ u_q = \omega_s L_s i_d + \omega_e \psi_f . \end{cases} \tag{5.3}$$

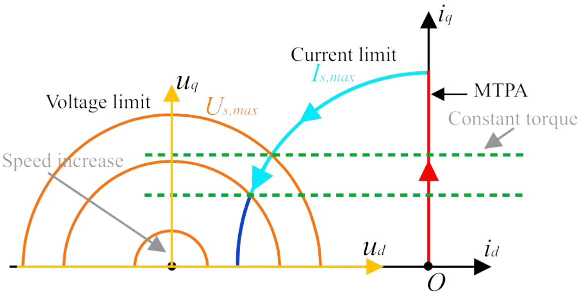

Fig. 5.1: The diagram of SPMSM constant power flux-weakening trajectory.

According to (5.2) and (5.3), the voltage and current limitation can be expressed as

$$\left(i_d + \psi_f / L_s\right)^2 + \left(i_q\right)^2 \leq \left(\frac{U_{s,\max}}{\omega_e L_s}\right)^2 \tag{5.4}$$

According to (5.4), the voltage confinement trajectory is represented as a cluster of concentric circles centered at $(-\psi_f/L_s, 0)$, with the radius varying according to the rotational speed ω_m. In contrast, the current limit is depicted as a circle centered at the origin, with a radius equal to the maximum limit current. Since the torque output of a SPMSM depends only on i_q, the torque constraint is represented by a series of horizontal lines which are parallel to the d-axis, as shown in Fig. 5.1.

Therefore, for SPMSM, the maximum torque per ampere (MTPA) control corresponds to $i_d = 0$ within the rated speed region. As the speed increases and the phase voltage amplitude approaches the maximum value permitted by the DC bus voltage, a higher speed can no longer be achieved through voltage adjustment alone, and the $i_d = 0$ control strategy becomes ineffective. Consequently, at a given torque, the motor must adjust both i_d and i_q to enable further speed increase by entering the FW region.

Theoretically, when the maximum demagnetization current $i_{d,max}$ is less than the maximum stator current $I_{s,max}$, the maximum achievable speed $\omega_{e,max}$ under FW control can be expressed as:

$$\omega_{e,max} = \frac{U_{s,max}}{\psi_f - L_s i_{d,max}} \tag{5.5}$$

In practical surface-mounted HSPMSM applications, the FW method typically enables an extension of the maximum operational speed by approximately 20% to 30% beyond the rated speed, while maintaining compliance with voltage and current constraints. High-speed SPMSM FW window is narrower than that of IPMSM. However, the estimator advances depend on BEMF and noise properties, not on saliency. Therefore, in this research, the harder SPMSM is validated to demonstrate robustness under the tighter margin typical of high-speed machines.

5.2.2 Estimated BEMF Harmonic Analysis

Due to the influence of the inverter non-idealities, dead-time effects, and magnetic saturation, the stator currents contain $(1 \pm 6k)$-order harmonics. These current harmonics induce corresponding harmonic voltages across the stator impedance, which can further degrade the accuracy of BEMF estimation and system performance.

The (3.1) can be expressed as a superposition of the fundamental and harmonic components, as follows:

$$\begin{cases} i_\alpha = i_{\alpha f} + i_{\alpha h} \\ i_\beta = i_{\beta f} + i_{\beta h} \end{cases} \tag{5.6}$$

with

$$\begin{cases} i_{\alpha f} = I_1 \cos(\omega_\mathrm{e} t + \varphi_1) \\ i_{\beta f} = I_1 \sin(\omega_\mathrm{e} t + \varphi_1) \end{cases} \tag{5.7}$$

$$\begin{cases} i_{\alpha h} = \sum\limits_{k=1}^{n} I_{1\pm 6k} \cos((1 \pm 6k)\,\omega_\mathrm{e} t + \varphi_{1\pm 6k}) \\ i_{\beta h} = \sum\limits_{k=1}^{n} I_{1\pm 6k} \sin((1 \pm 6k)\,\omega_\mathrm{e} t + \varphi_{1\pm 6k}) \end{cases} \tag{5.8}$$

where I_1, $I_{1\pm 6k}$, φ_1 and $\varphi_{1\pm 6k}$ are the stator current amplitude and initial phase of fundamental and $(1 \pm 6k)$-order harmonics, respectively. $i_{\alpha f}$, $i_{\alpha h}$, $i_{\beta f}$ and $i_{\beta h}$ are the fundamental and $(1 \pm 6k)$-order harmonics of i_α and i_β, respectively.

Current harmonics directly impair the accuracy of BEMFs by introducing waveform distortion and increasing the THD. This degradation can lead to errors in rotor position and speed estimation, increased torque ripple, and reduced observer performance. Since the BEMFs obtained by the

ESO inherently contain rotor position information, the presence of current harmonics results in the estimated BEMFs, $\hat{e}_\alpha$ and $\hat{e}_\beta$, being contaminated with harmonic components.

The BEMFs in (3.2) can be expressed as a superposition of the fundamental and harmonic components, as follows:

$$\boldsymbol{e}_m = \boldsymbol{e}_f + \boldsymbol{e}_h \tag{5.9}$$

with

$$\boldsymbol{e}_f = \begin{bmatrix} -E_1 \sin\left(\omega_e t + \theta_{e1}\right) \\ E_1 \cos\left(\omega_e t + \theta_{e1}\right) \end{bmatrix} \tag{5.10}$$

$$\boldsymbol{e}_h = \begin{bmatrix} -\sum\limits_{k=1}^{n} E_{6k\pm1} \sin\left(\pm\left(6k \pm 1\right)\omega_e t + \theta_{e(6k\pm1)}\right) \\ \sum\limits_{k=1}^{n} E_{6k\pm1} \cos\left(\pm\left(6k \pm 1\right)\omega_e t + \theta_{e(6k\pm1)}\right) \end{bmatrix} \tag{5.11}$$

where $\boldsymbol{e}_m = [e_{\alpha m}, e_{\beta m}]^T$. $\boldsymbol{e}_f = [e_\alpha, e_\beta]^T$ and $\boldsymbol{e}_h = [e_{\alpha h}, e_{\beta h}]^T$ are the fundamental and $(1 \pm 6k)$-order harmonics of the BEMFs. E_1, $E_{6k\pm1}$, θ_{e1}, and $\theta_{e(6k\pm1)}$ are the BEMFs amplitude and initial estimated rotor position of fundamental and $(1 \pm 6k)$-order harmonics, respectively.

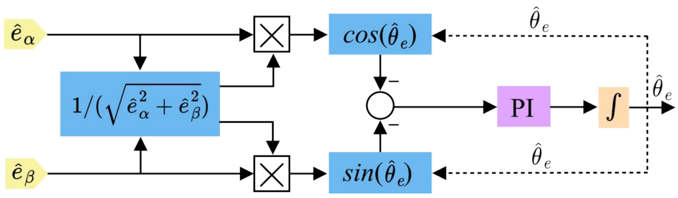

Fig. 5.2: The diagram of a normalized quadrature PLL.

As shown in Fig. 5.2, the rotor position is estimated using a PLL. The position error signal ε within the PLL is expressed as:

$$\begin{aligned} \varepsilon &= -\hat{e}_\alpha \cos\theta_e - \hat{e}_\beta \sin\theta_e \\ &= E_1 \sin\left[\left(\hat{\omega}_e - \omega_e\right)t + \theta_{r1} - \theta_{e1}\right] \\ &+ \sum_{k=1}^{n} E_{6k\pm1} \sin\left[\left(\left(1 \pm 6k\right)\hat{\omega}_e - \omega_e\right)t + \theta_{r(6k\pm1)} - \theta_{e1}\right] \end{aligned} \tag{5.12}$$

where θ_{r1} and $\theta_{r(6k\pm1)}$ are the initial actual rotor position of fundamental and $(1 \pm 6k)$-order harmonics, respectively.

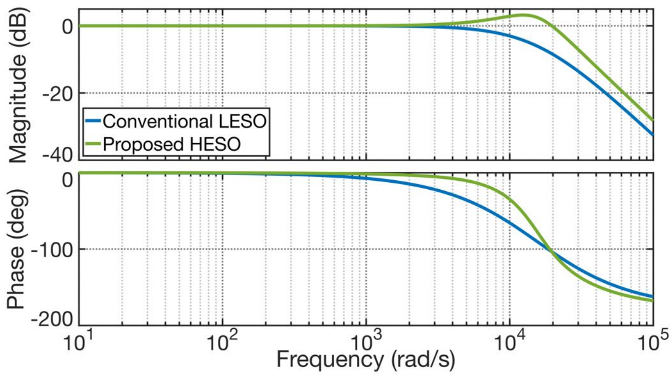

Fig. 5.3: Comparison of the Bode diagram between conventional LESO and HESO.

As can be seen from (5.12), the presence of $(1 \pm 6k)$-order harmonics in the BEMFs introduces observation errors in the PLL-based estimator. Consequently, the position error signal ε becomes contaminated with harmonic interference, which degrades the accuracy of rotor position estimation.

5.3 Proposed SOGI-HESO for Sensorless Control

The analysis of conventional LESO and the deduction of HESO have been presented in the Chapters 4.3 and 4.4. Hence, a detailed analysis of these theories are omitted here for conciseness.

The principle of HESO in reducing phase lag lies in its ability to incorporate the dynamic evolution of the BEMF into the observer model. Unlike the conventional LESO, which acts as a second-order low-pass filter (LPF) and therefore suffers from inherent phase delay, the HESO introduces derivative states of the BEMF. These additional states act as predictive elements, enabling the observer to follow rapid changes in BEMF more closely, especially when the input varies rapidly, as in the FW regions of high-speed SPMSM. Consequently, the frequency response of HESO exhibits a higher effective bandwidth and a flatter phase characteristic, significantly mitigating phase lag in the estimation process.

To compare the performance of conventional LESO and HESO, the Bode diagram is presented in Fig. 5.3. Compared with the conventional LESO, the HESO is superior in the high-frequency region both in bandwidth and roll-off speed.

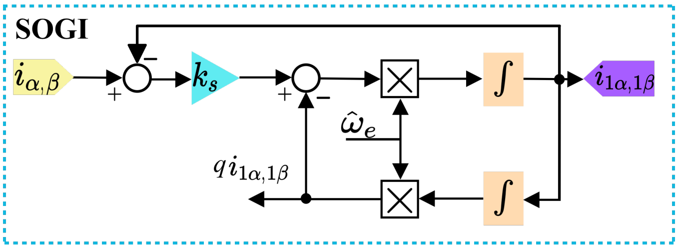

Fig. 5.4: The schematic diagram of the SOGI structure.

5.3.1 SOGI-Based BEMF Estimation

To enhance the accuracy of the HESO, SOGIs are employed to filter out current and voltage harmonics and are integrated with the HESO framework. The schematic diagram of the SOGI structure is shown in Fig. 5.4, which illustrates its capabilities in frequency selection and signal integration.

The inputs to the SOGI are u_α, u_β, i_α, and i_β, which contain DC components, fundamental components, and harmonic components. The k_s represents the gain coefficient of the SOGI. The signals $i_{1\alpha}$ and $i_{1\beta}$ are the filtered current outputs. The SOGI acts as a band-pass filter (BPF) for the BEMFs, effectively attenuating harmonics and noise to improve the accuracy of BEMF estimation.

The transfer function of SOGI can be expressed as:

$$D(s) = \frac{i_{1\alpha,1\beta}}{i_{\alpha,\beta}} = \frac{k_s \hat{\omega}_e s}{s^2 + k_s \hat{\omega}_e s + \hat{\omega}_e^2} \tag{5.13}$$

$$Q(s) = \frac{qi_{1\alpha,1\beta}}{i_{\alpha,\beta}} = \frac{k_s \hat{\omega}_e^2}{s^2 + k_s \hat{\omega}_e s + \hat{\omega}_e^2} \tag{5.14}$$

where $q = e^{-\pi/2j}$, and k_s is the damping coefficient. $D(s)$ and $Q(s)$ represent the transfer functions of the SOGI in the in-phase and quadrature directions, respectively. Specifically, $D(s)$ functions as a second-order BPF, while $Q(s)$ serves as a second-order LPF.

The amplitude and phase frequency characteristics of (5.13) are as follows:

$$i_{1\alpha,1\beta} = D(s) i_{\alpha,\beta} \tag{5.15}$$

$$\begin{cases} \mid D(j\omega) \mid = (k_s\hat{\omega}_e\omega_o)/\sqrt{\left(\hat{\omega}_e^2 - \omega_o^2\right)^2 + (k_s\omega_o\hat{\omega}_e)^2} \\ \angle D(j\omega) = atan2\left((\hat{\omega}_e^2 - {\omega_o}^2), k_s\hat{\omega}_e\omega_o\right) \end{cases} \tag{5.16}$$

where $|D(j\omega)|$ and $\angle D(j\omega)$represent the amplitude and phase angle of the transfer functions $D(s)$. ω_o denotes the center frequency of the SOGI. When the estimated angular frequency $\hat{\omega}_e$ equals the center frequency ω_o, the system achieves error-free tracking of the input signal's angular frequency. The phase-frequency responses of the SOGI demonstrate its ability to suppress harmonic components while accurately extracting sinusoidal input signals without magnitude attenuation or phase distortion.

The SOGI sets its center frequency using the previous sample electrical speed, thereby avoiding any algebraic loop with the HESO. Moreover, the estimator dynamics are an order of magnitude faster than the mechanical speed variations, which keeps the phase lag small and ensures stable tracking even during abrupt transients.

Bode diagrams of the SOGI under varying frequencies and damping coefficients k_s are shown in Fig. 5.5. These diagrams illustrate the influence of k_s and frequency tuning on the amplitude and phase characteristics of the SOGI, highlighting its capability to selectively filter the fundamental component while attenuating undesired harmonics and noise.

Here, k_s is set to 2.5. Smaller values can introduce under-damped peaking and greater harmonic sensitivity, whereas larger values increase phase lag and broaden the passband, admitting more noise.

5.3.2 Speed Control Based on Adaptive LADRC in the FW Region

To enhance the FW control performance, an ALADRC method is employed in the speed control loop. While retaining the advantages of conventional ADRC, the adaptive bandwidth mechanism dynamically adjusts the control bandwidth based on the motor speed. This approach addresses the challenges posed by disturbances and environmental variations commonly encountered in HSPMSMs, thereby further improving control performance.

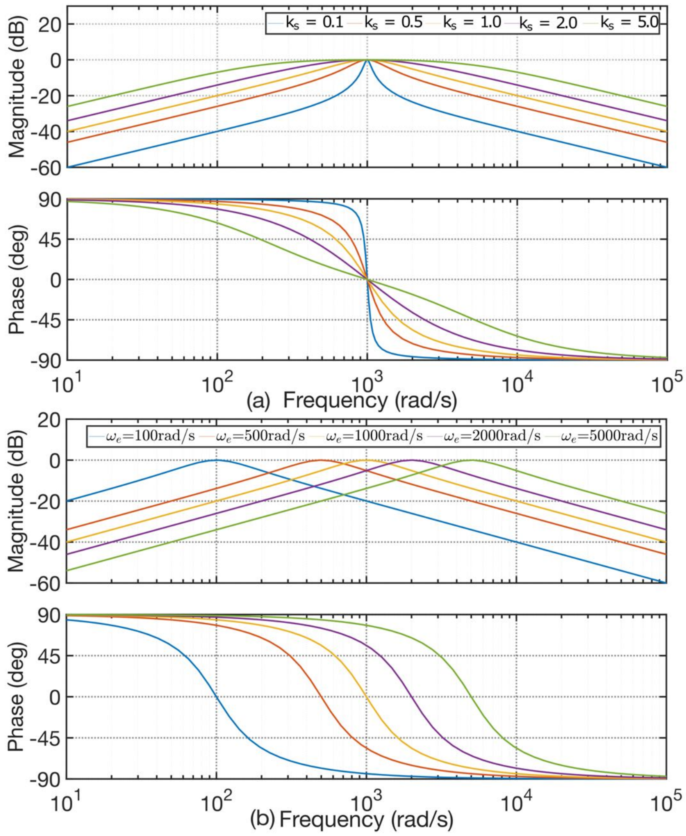

Fig. 5.5: Bode diagrams of the SOGI in different (a) damping coefficients, and (b) frequencies.

The adaptive bandwidth function, adjusted online according to the rotor speed, can be expressed as:

$$\omega_c' = \omega_{cmin} + (\omega_{cmax} - \omega_{cmin})softsign(c_1 \cdot |\omega_e|) \tag{5.17}$$

where $softsign(x) = x/(1+ \mid x \mid)$, c_1 is the adaptation gain. ω_{cmin} and ω_{cmax} are the minimum and maximum observer bandwidths in the adaptive controller, respectively. A fixed LADRC must choose a single bandwidth that compromises between transient speed and steady-state noise. ALADRC uses an adaptive bandwidth, while increasing the value during transients also reduces the ESO residual. This provides a clear theoretical reason for the adaptive scheme outperforms a fixed-bandwidth LADRC.

In the speed control loop, according to (3.3) and (3.4), it can be observed that the relationship between the input and output of the speed controller follows a first-order differential equation. Accordingly, a first-order ALADRC is employed for speed regulation. Since the output of the second-order LESO does not involve differential terms, the tracking differentiator (TD) is omitted in this design.

According to (3.3) and (3.4), the speed can be expressed as

$$\dot{\omega}_m = \frac{K_T}{J} i_q^* + \frac{T_d}{J} \tag{5.18}$$

where K_T is torque constant, and i_q^* denotes the reference q-axis current. T_d/J represents the total external and internal disturbance of the system, and $T_d = K_T(i_q - i_q^*) - T_L - B\omega_m$.

According to (4.2), the second order LESO of (5.18) can be rewrite as

$$\begin{cases} e_r = z_1 - \omega_m \\ \dot{z}_1 = z_2 - \beta_{r1} e_r + b_0 u_0 \\ \dot{z}_2 = -\beta_{r2} e_r \end{cases} \tag{5.19}$$

where $u_0 = i_q$ is the input of the system. e_r is the error signal of the rotation speed. z_1 is the observed value of the speed. z_2 is the observed value of the disturbance, and $b_0 = K_T/J$. β_{r1} and β_{r2} are the observer gains.

Then, the linear state error feedback (LSEF) can be expressed as

$$\begin{cases} e_{r1} = \omega_m^* - z_1 \\ u_0 = K_p \cdot e_{r1} \\ u = (u_0 - z_2)/b_0 \end{cases} \tag{5.20}$$

where ω_m^* is the reference speed, K_p is the control rate gain of the LSEF, e_{r1} is the speed error, and u is the output of the LSEF. Therefore, the speed controller can be finally designed as:

$$i_q^* = \frac{u_0 - z_2}{b_0} = \frac{K_p(\omega_m^* - \omega_m) - z_2}{b_0} \tag{5.21}$$

The block diagram of the ALADRC-based speed controller is illustrated in Fig. 5.6. According to the observer design principles presented in [111], the relationship between the observer parameters and the bandwidth ω_{ro} is given by:

$$K_p = \omega_c{}', \beta_{r1} = 2\omega_{ro}, \beta_{r2} = \omega_{ro}^2, \omega_{ro} = 3\omega_c{}'. \tag{5.22}$$

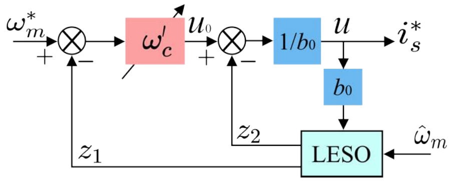

Fig. 5.6: The block diagram of the ALADRC-based speed controller.

5.4 Stability and Performance Analysis of SOGI-HESO

5.4.1 Stability and Analysis of SOGI-HESO

The SOGI is a linear time-invariant (LTI) system, and its stability is determined by the location of its poles. When the damping factor and natural frequency are properly selected, the poles lie in the left-half of the s-plane, ensuring system stability. According to the SOGI transfer function in (5.13), the system remains stable for all positive values of the damping coefficient k_s. Then, the stability analysis of the individual HESO is presented. According to (4.7), the HESO transfer function of $E_\alpha(s)$ can be obtained as

$$\frac{\hat{E}_\alpha(s)}{E_\alpha(s)} = -\frac{\beta_2 s + \beta_3}{s^3 + (\mu + \beta_1)s^2 + \beta_2 s + \beta_3} \tag{5.23}$$

The stability of this system can be analyzed by inspecting the characteristic polynomial from the denominator of the transfer function. The characteristic polynomial can be expressed as

$$D(s) = s^3 + (\mu + \beta_1)s^2 + \beta_2 s + \beta_3 \tag{5.24}$$

let $a_1 = \mu + \beta_1$, $a_2 = \beta_2$, $a_0 = \beta_3$, then the polynomial can be rewrite as

$$D(s) = s^3 + a_2 s^2 + a_1 s + a_0 \tag{5.25}$$

According to the Routh–Hurwitz criterion, the generalized Routh array for (5.25) is shown in Table 5.1.

Table 5.1: Routh Array for First-level HESO Polynomial.

s^3	1	β_2
s^2	$\mu+\beta_1$	β_3
s^1	$\frac{(\mu+\beta_1)\beta_2-\beta_3}{\mu+\beta_1}$	0
s^1	β_3	0

The stability condition is the elements in the first column of the Routh table must be positive. Thus, the stability condition can be expressed as

$$\mu+\beta_1>0,\beta_3>0,(\mu+\beta_1)\beta_2>\beta_3. \tag{5.26}$$

where μ, β_1, β_3 are positive guaranteed. In other words, if the condition of $\beta_1\beta_2 > \beta_3$ is satisfied, the characteristic polynomial explicitly has all poles in the left half-plane and the ESO is stable. According to the HESO gains selection principle in [85, 111], and combined the results of theoretical analysis and actual testing, the following gain parameters are finally designed as

$$\beta_1=2\omega_1,\beta_2=2{\omega_1}^2,\beta_3={\omega_1}^3. \tag{5.27}$$

where ω_1 is the observer bandwidth of HESO. ω_1 is set between two and three times the electrical fundamental in FW, but keep it no more than one-quarter of the sampling frequency. With SOGI prefiltering, this choice of ω_1 reduces phase lag without noise peaking and keeps the observer poles safely inside the unit circle. Therefore, since the SOGI is linear and BIBO stable, and the observer gain is designed for stability, the cascade SOGI-HESO system is stable as long as its individual stability criteria are satisfied.

5.4.2 Performance Analysis of SOGI as Pre-Filter and Post-Filter

As shown in Fig. 5.7, both SOGI pre-filtering and SOGI post-filtering can be employed to enhance the BEMF. To evaluate the effectiveness of these two strategies, an FFT analysis was conducted on the input current as well as the outputs obtained from each SOGI filtering method.

In Fig. 5.8, the FFT analysis reveals that SOGI pre-filtering provides superior suppression of harmonics and high-frequency noise, resulting in a cleaner and more robust input signal for the

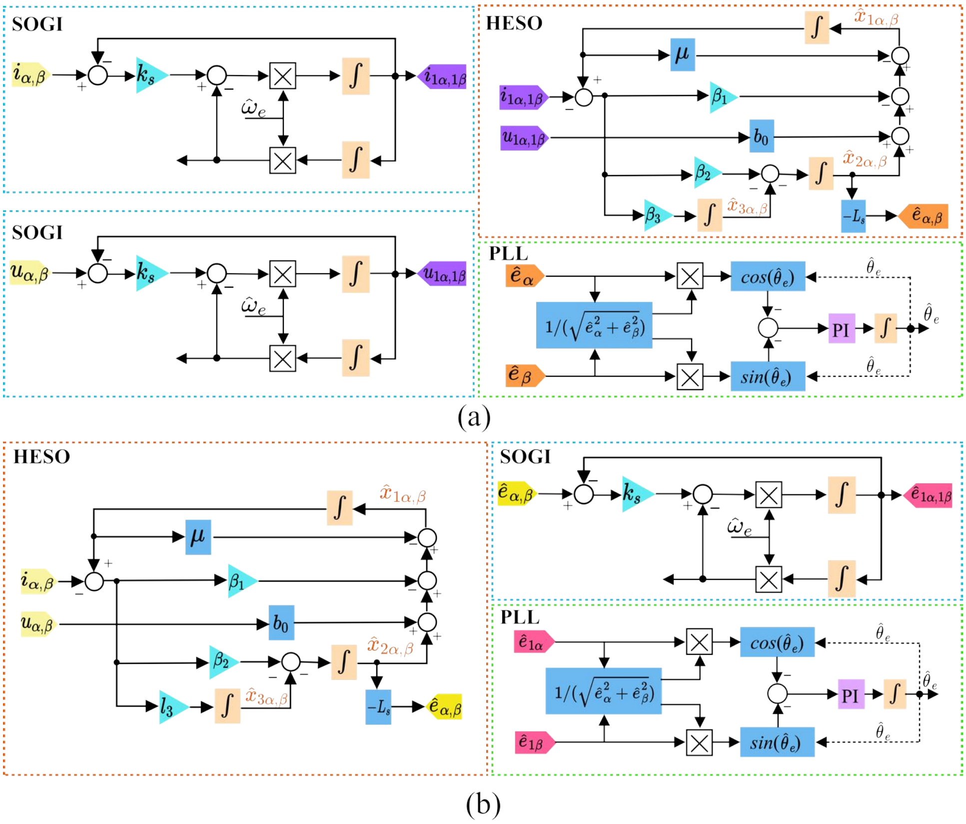

Fig. 5.7: The structures of (a) SOGI pre-filter and (b) SOGI post-filter.

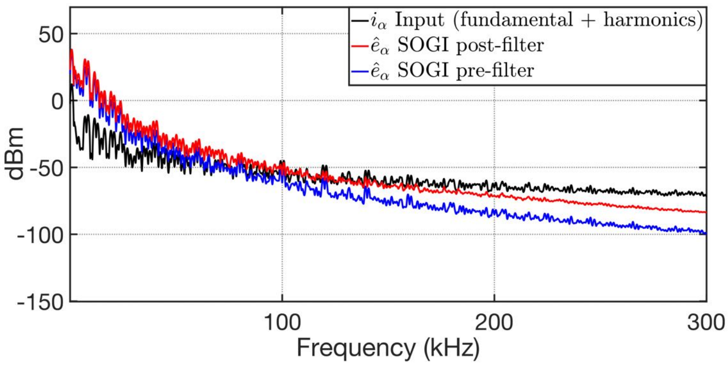

Fig. 5.8: Single-sided FFT magnitude of input current and SOGI-filtered outputs

observer. In contrast, while SOGI post-filtering can effectively reduce output noise, it allows harmonics and noise to influence the internal states of the observer, which may degrade estimation accuracy. In Fig. 5.8, the pre-filter curve sits 10–20 dB lower than the red curve, indicating stronger attenuation of broadband switching components and higher-order harmonics before they reach the observer. Therefore, placing the SOGI in front of the HESO yields a cleaner input spectrum than filtering after the observer, which supports better estimation quality and allows using a higher

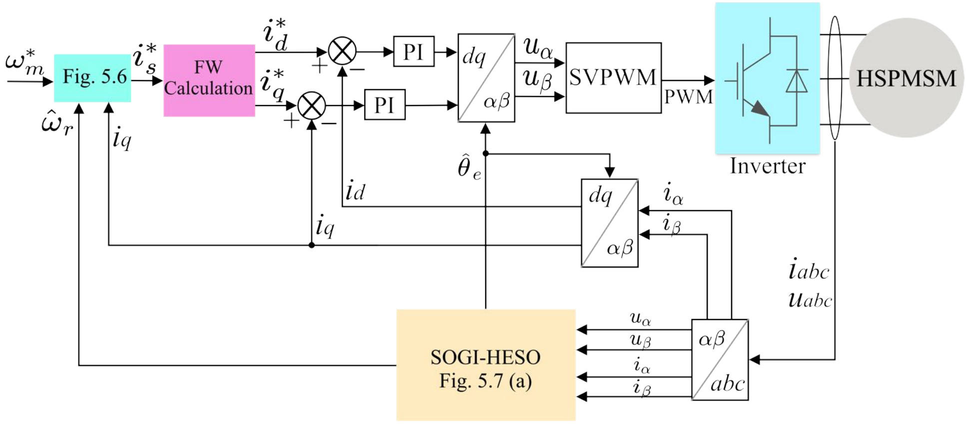

Fig. 5.9: The control diagram of the proposed SOGI-HESO combined with ALADRC.

observer bandwidth with less penalty

Therefore, employing SOGI as a pre-filter is preferable for sensorless HSPMSM control, as it provides a cleaner input to the observer, resulting in improved estimation accuracy, enhanced stability, and greater robustness against noise and harmonics. The control diagram of the proposed SOGI-HESO combined with ALADRC is illustrated in Fig. 5.9. As this research does not primarily focus on FW control strategies, the conventional CVCP FW method is adopted for implementation.

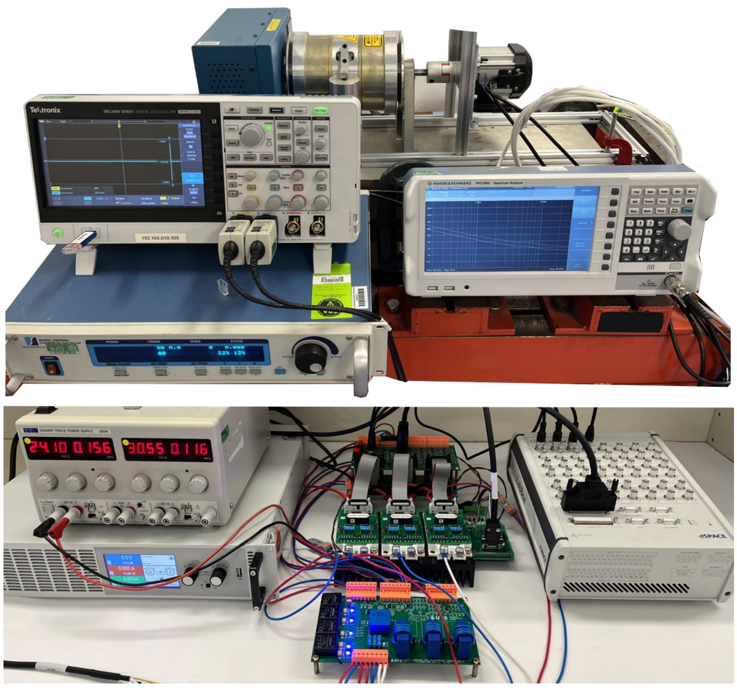

Fig. 5.10: Overview of testbench and drive system setup.

5.5 Experimental Test and Results

An overview of the experimental test platform is shown in Fig. 5.10. A small-scale high-speed SPMSM test setup is built, consisting of a dSPACE MicroLabBox, interface boards, a voltage and current sampling board, a three-phase inverter utilizing Infineon FF600R12ME4 modules, and an high-speed SPMSM testbench. The control algorithms for the high-speed SPMSM were implemented using a dSPACE MicroLabBox (DS1202) processor. All tasks were executed at a sampling frequency of 10 kHz. Detailed specifications of the tested high-speed SPMSM are listed in Table 5.2, and the associated observer gains and controller parameters are summarized in Table 5.3.

Table 5.2: Parameters of high-speed SPMSM System.

Parameters	Unit	Value
Rated Speed	r/min	12,000
Rated torque	N.m	0.375
Rated Power	kW	0.45
Rated voltage	V	311
Rated current	A	3.5
Maximum speed	A	15,500
Maximum current	A	6.5
No. of pole pairs	-	3
Stator resistance	Ω	1.9
d-axis inductance (L_s)	mH	2.7
q-axis inductance(L_s)	mH	2.7
Magnet flux linkage	Wb	0.045

Table 5.3: Observer Parameters of ESO.

Parameters	Value	Parameters	Value
l_1 (LESO)	4.01e+04	K_i (PI)	0.23
l_2 (LESO)	8.38e+08	ω_{cmin} (ALADRC)	1.25e+03
β_1 (HESO)	3.07e+04	ω_{cmax} (ALADRC)	2.20e+03
β_2 (HESO)	7.10e+08	c_1 (ALADRC)	0.3
β_3 (HESO)	6.69e+12	k_s (SOGI)	2.5
K_p (PI)	0.05	l_2 (LADRC)	2.19e+03

5.5.1 Steady-State Performance Analysis

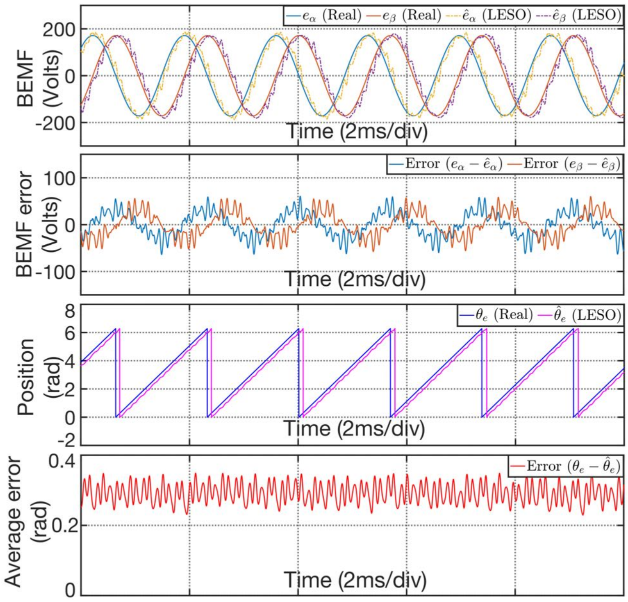

Fig. 5.11: Steady-state results of conventional LESO at 12,000 r/min with no load.

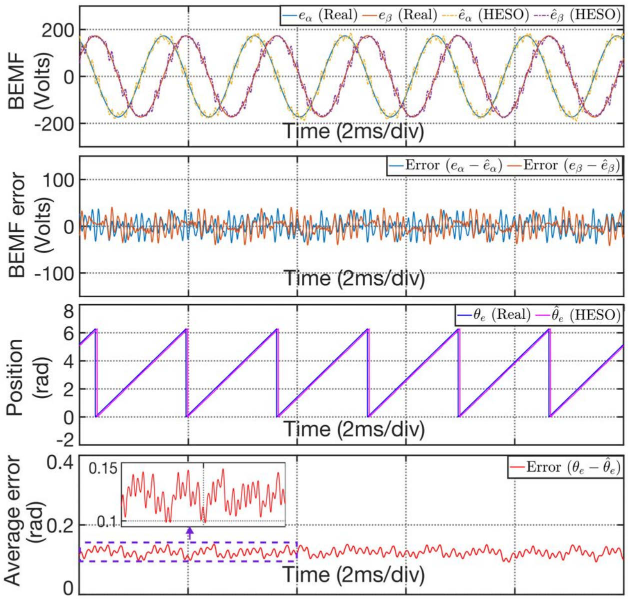

Fig. 5.12: Steady-state results of HESO at 12,000 r/min with no load.

In Figs. 5.11-5.28, the steady-state performance of conventional LESO, HESO, and the proposed SOGI-HESO is compared at various speeds and load conditions..

In Figs. 5.11-5.16, the steady-state performance is compared at the rated speed of 12,000 r/min without load. As shown in Figs. 5.11-5.13, the amplitudes of the BEMF estimation error are 55

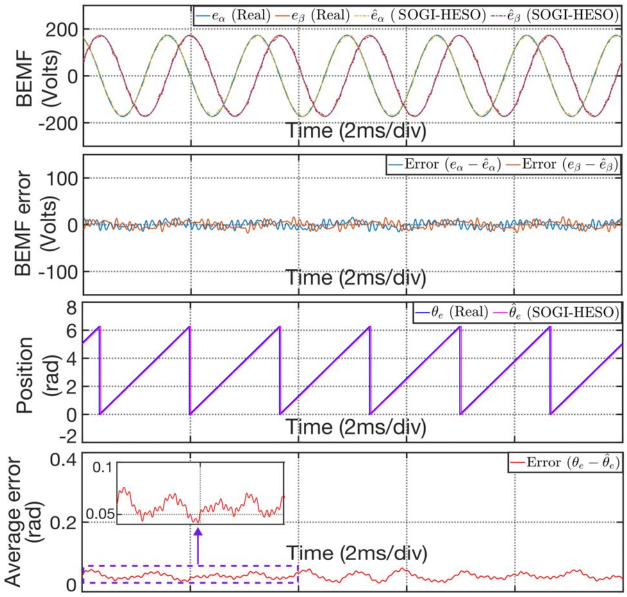

Fig. 5.13: Steady-state results of SOGI-HESO at 12,000 r/min with no load.

V, 33 V, and 11 V for LESO, HESO, and SOGI-HESO, respectively. The corresponding average position estimation errors are approximately 0.34 rad, 0.13 rad, and 0.06 rad.

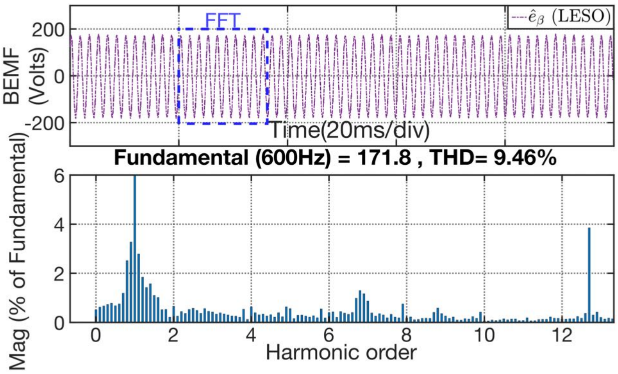

Fig. 5.14: FFT result of conventional LESO at 12,000 r/min with no load.

In Figs.5.14-5.16, FFT analysis of the estimated BEMF signals yields THD values of 14.46%, 11.74%, and 4.14% for LESO, HESO, and SOGI-HESO, respectively. Compared to LESO and HESO, the position estimation error and the THD of SOGI-HESO are reduced significantly. These results demonstrate that the SOGI-HESO suppresses harmonics and reduces estimation error in the MTPA region.

In Figs. 5.17-5.22, the steady-state performance is compared at the speed of 15,000 r/min without load in the FW region. As shown in Figs. 5.17-5.19, the amplitudes of the BEMF estimation error

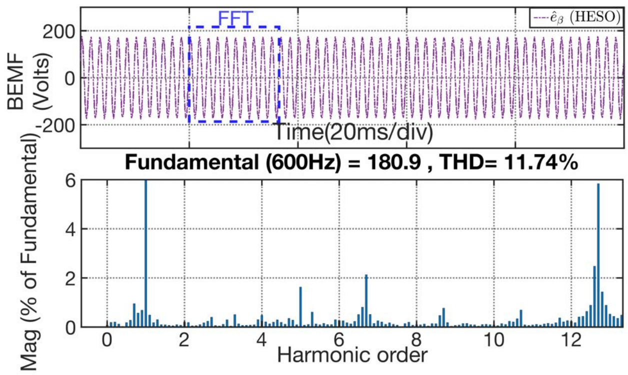

Fig. 5.15: FFT result of HESO at 12,000 r/min with no load.

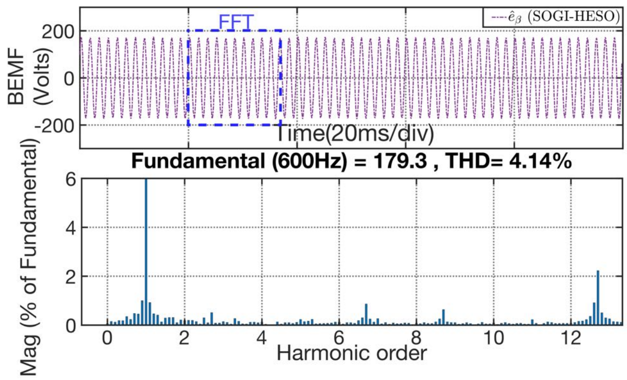

Fig. 5.16: FFT result of SOGI-HESO at 12,000 r/min with no load.

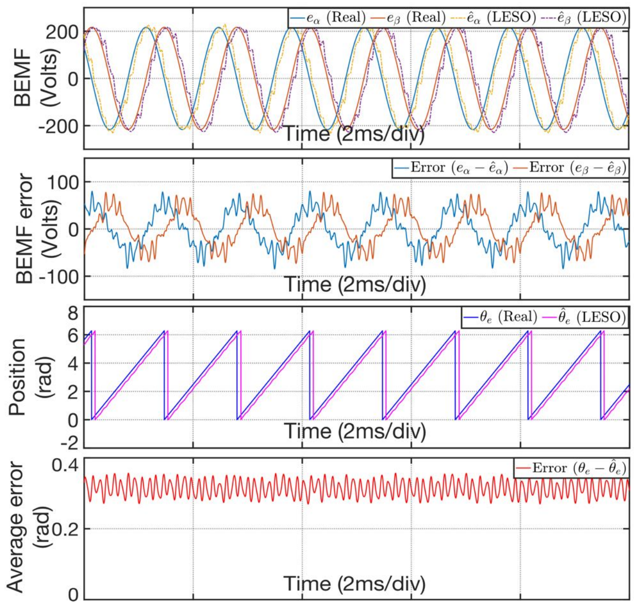

Fig. 5.17: Steady-state results of conventional LESO at 15,000 r/min with no load.

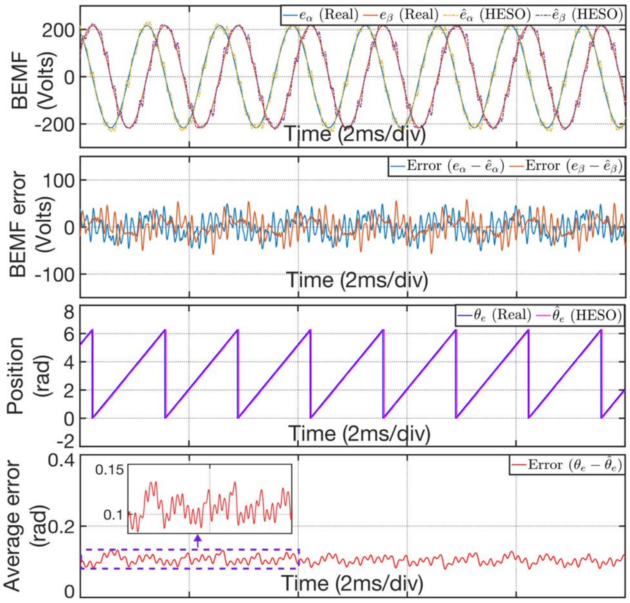

Fig. 5.18: Steady-state results of HESO at 15,000 r/min with no load.

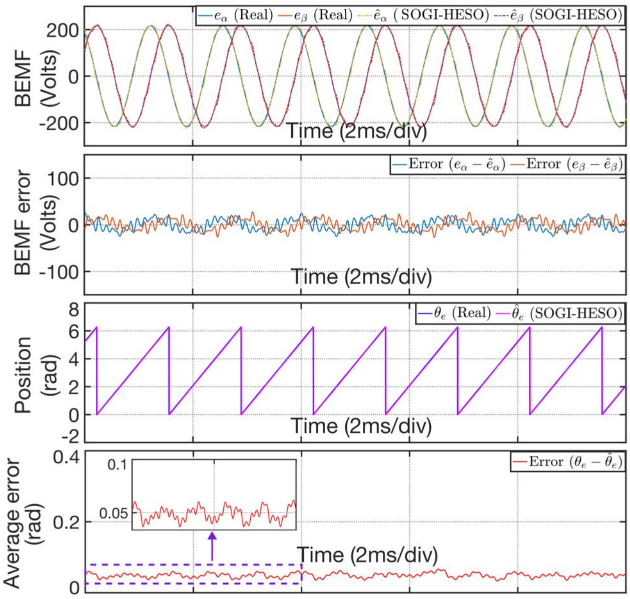

Fig. 5.19: Steady-state results of SOGI-HESO at 15,000 r/min with no load.

are 89 V, 40 V, and 15 V for LESO, HESO, and SOGI-HESO, respectively. The corresponding average position estimation errors are approximately 0.32 rad, 0.11 rad, and 0.05 rad.

In Figs. 5.20-5.22, FFT analysis of the estimated BEMF signals yields THD values of 7.28%, 9.9%, and 4.78% for LESO, HESO, and SOGI-HESO, respectively. Compared to LESO and HESO, the position estimation error of SOGI-HESO is reduced by 84.3% and 54.5%, respectively, while

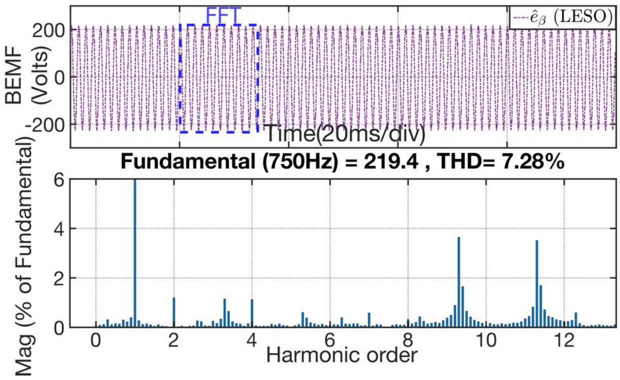

Fig. 5.20: FFT result of conventional LESO at 15,000 r/min with no load.

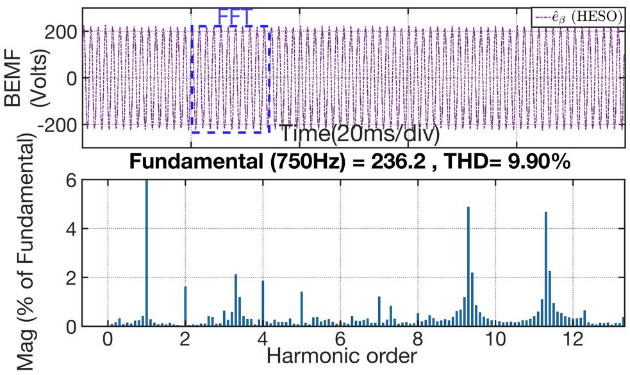

Fig. 5.21: FFT result of HESO at 15,000 r/min with no load.

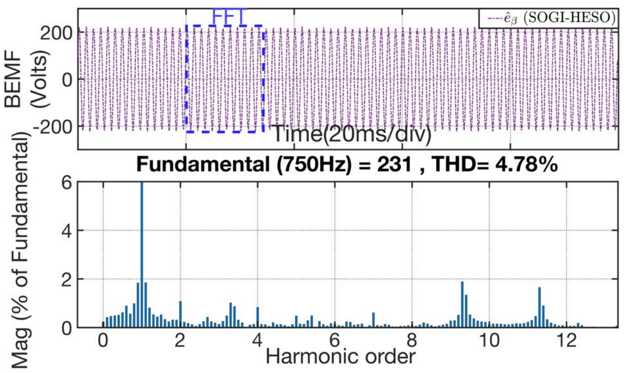

Fig. 5.22: FFT result of SOGI-HESO at 15,000 r/min with no load.

the THD is reduced by 34.3% and 51.7%. These results confirm that the proposed SOGI-HESO significantly improves position estimation accuracy in the FW region. The results comparison for the conventional LESO, HESO, and the proposed SOGI-HESO is listed in Table 5.4. Performance metrics are evaluated at representative MTPA and flux-weakening operating points defined in Table 4.2.

Table 5.4: The comparison of different observer methods.

Speed (r/min)	Items	LESO	HESO	SOGI-HESO
12,000 (MTPA)	BEMF error amplitude (Volts)	55	33	11
12,000 (MTPA)	Average position errors (rad)	0.34	0.13	0.06
12,000 (MTPA)	BEMF THD (%)	9.46	11.74	4.14
15,000 (FW)	BEMF error amplitude (Volts)	89	40	15
15,000 (FW)	Average position errors (rad)	0.32	0.11	0.05
15,000 (FW)	BEMF THD (%)	7.28	9.9	4.78

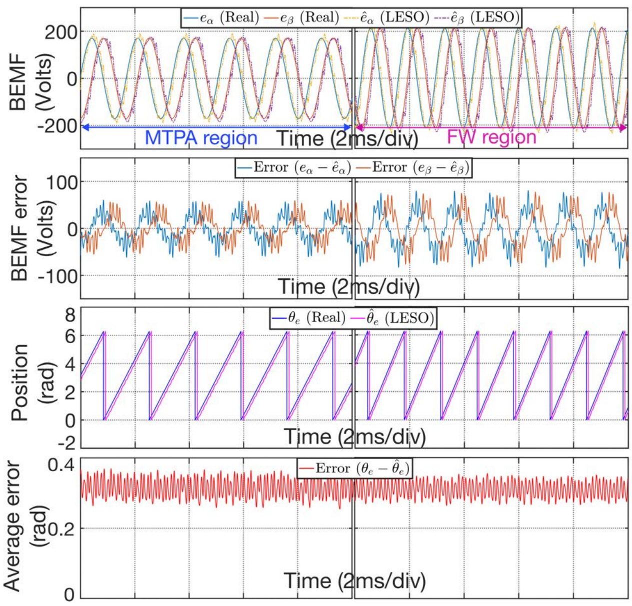

Fig. 5.23: Steady-state results of conventional LESO at 12,000 r/min and 15,000 r/min with load.

In Figs. 5.23-5.28, the steady-state performance with load is compared at the speeds of 12,000 r/min and 15,000 r/min. In the MTPA region, the 100% rated load was applied at the rated speed of 12,000 r/min. In the FW region, the 60% rated load was applied at the maximum speed of 15,000 r/min, which is the highest load that keeps the inverter within linear modulation, respects the safe i_d limit, and leaves a voltage margin for dynamic events. As shown in Figs. 5.23-5.25, the proposed SOGI-HESO continues to track the BEMF and rotor position accurately at both speeds.

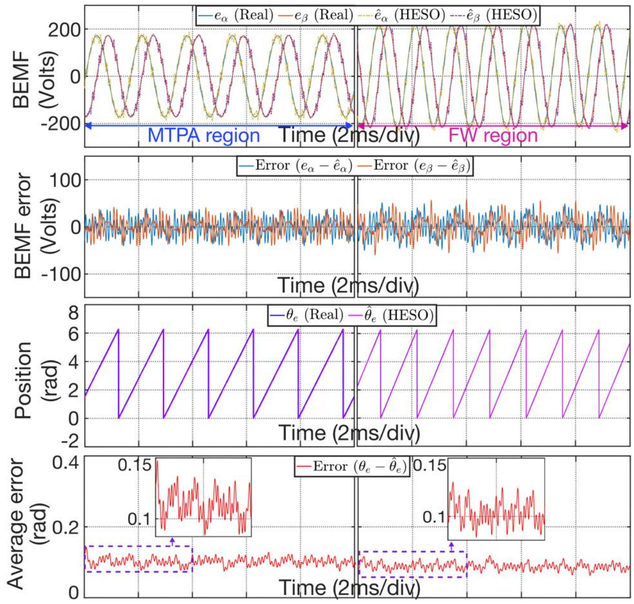

Fig. 5.24: Steady-state results of HESO at 12,000 r/min and 15,000 r/min with load.

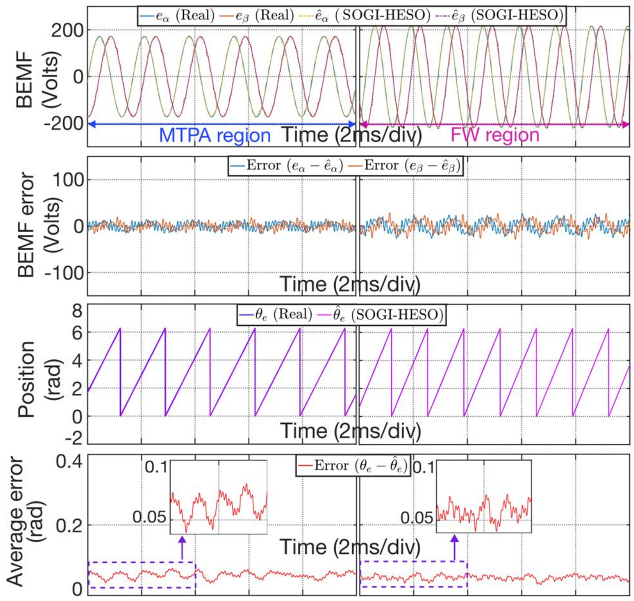

Fig. 5.25: Steady-state results of SOGI-HESO at 12,000 r/min and 15,000 r/min with load.

Across both speeds, the proposed SOGI-HESO yields visibly cleaner waveforms, smaller BEMF error, accurate position traces, and lower THD, while LESO and HESO show larger error ripple.

Compared with the no-load FFT results in Table 5.4, the LESO's limited bandwidth and larger phase lag allow more load-induced harmonics and noise to enter the BEMF estimate, increasing THD. By contrast, the HESO lowers phase lag, and the SOGI-HESO adds harmonic pre-filtering,

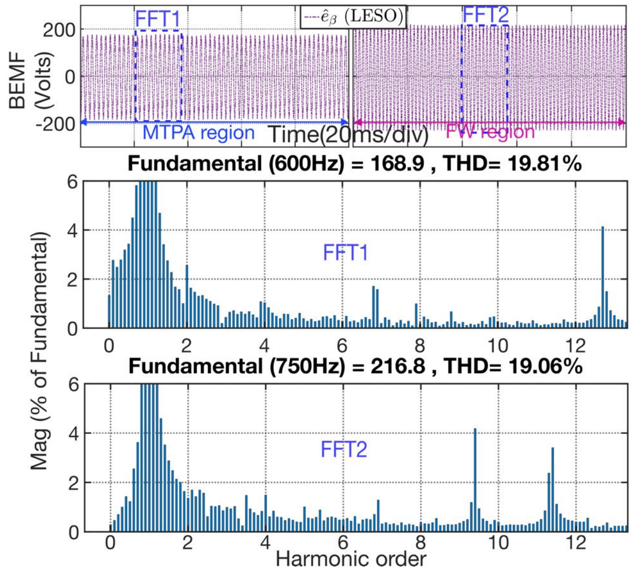

Fig. 5.26: FFT result of conventional LESO at 12,000 r/min and 15,000 r/min with load.

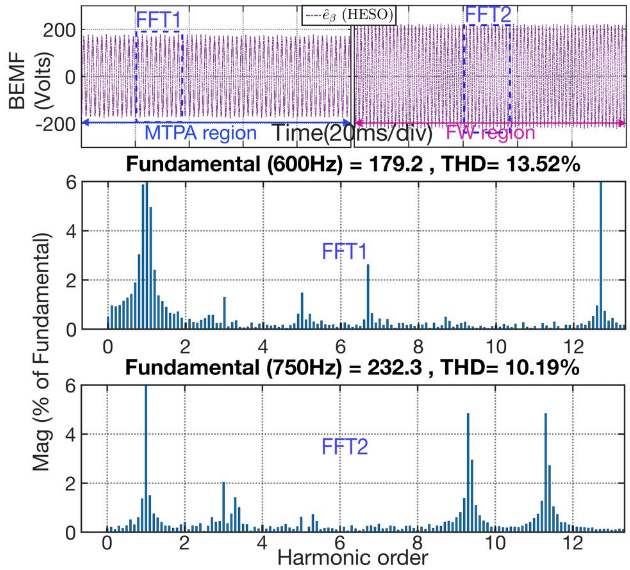

Fig. 5.27: FFT result of HESO at 12,000 r/min and 15,000 r/min with load.

so the estimated BEMF remains nearly sinusoidal and its THD is largely unchanged under load, as shown in Figs. 5.26-5.28. These results confirm that the proposed SOGI-HESO effectively sustains accurate estimation in loaded MTPA and FW regions.

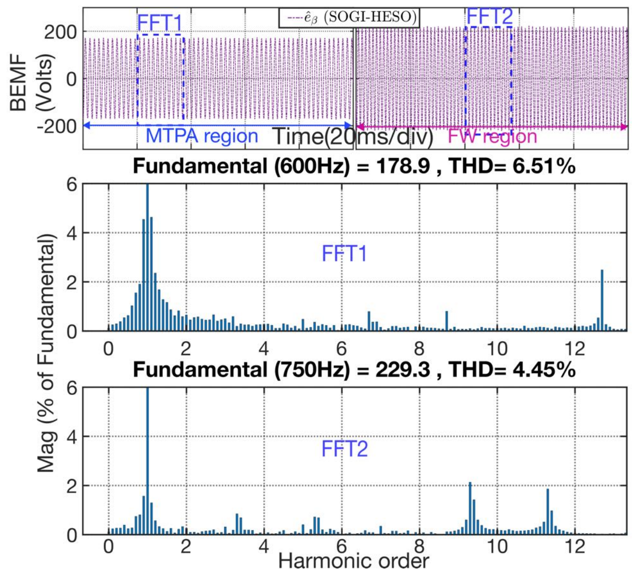

Fig. 5.28: FFT result of SOGI-HESO at 12,000 r/min and 15,000 r/min with load.

5.5.2 Transient Process and Disturbance Analysis

To validate the transient performance of the SOGI-HESO-based methods during step speed transients and step load change, three different speed loop controllers are compared, including conventional PI, LADRC, and the ALADRC. In Figs. 5.29-5.40, the step speed transient performance from 12,000 r/min to 15,000 r/min with 50% rated load and the step load change performance at 15,000 r/min from 0 to 60% rated load are compared, respectively.

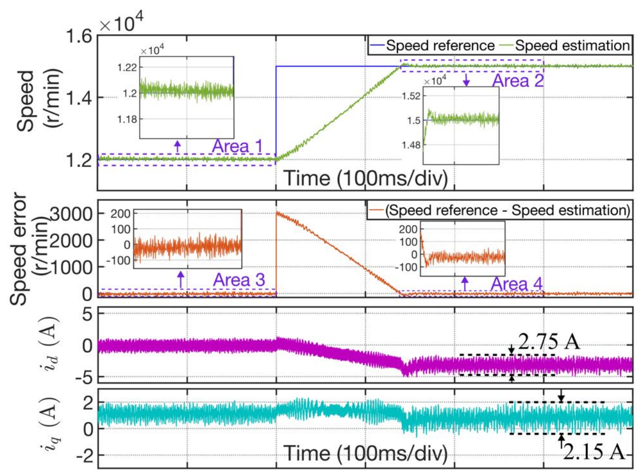

Fig. 5.29: SOGI-HESO-based PI with step speed change from 12,000 r/min to 15,000 r/min with 50% rated load.

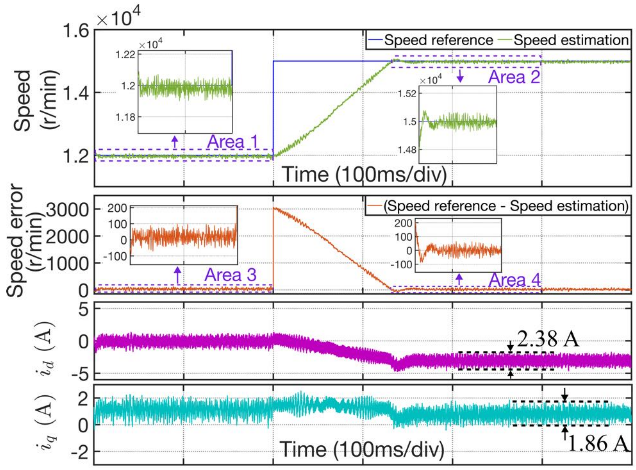

Fig. 5.30: SOGI-HESO-based LADRC with step speed change from 12,000 r/min to 15,000 r/min with 50% rated load.

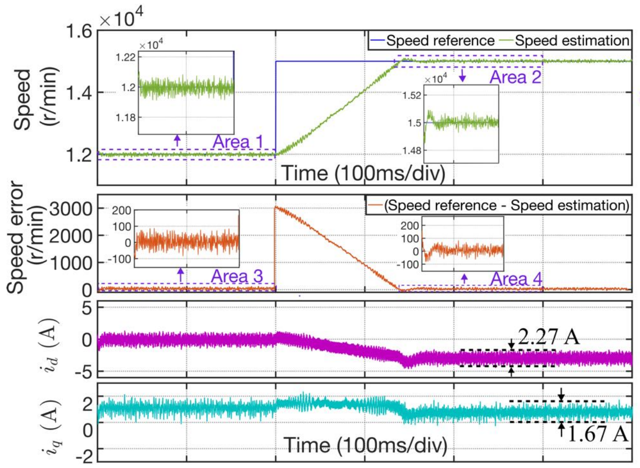

Fig. 5.31: SOGI-HESO-based ALADRC with step speed change from 12,000 r/min to 15,000 r/min with 50% rated load.

As shown in the enlarged views in Figs. 5.29-5.31, the speed error amplitudes at 12,000 r/min are 118 r/min, 96 r/min, and 83 r/min, and at 15,000 r/min are 95 r/min, 90 r/min, and 80 r/min for the PI, LADRC, and ALADRC methods, respectively. The $d-$ and $q-$axis current waveforms indicate that the proposed SOGI-HESO-based ALADRC reduces both the oscillation amplitude and current tracking error compared to the other controllers.

Furthermore, FFT analysis of the phase currents shows that the total harmonic distortion (THD) is 13.57% for PI, 13.46% for LADRC, and 11.66% for ALADRC, demonstrating that SOGI-HESO-based ALADRC achieves improved current quality in addition to enhanced speed control performance in the FW region, as shown in Figs 5.32-5.34. Therefore, these comparisons confirm

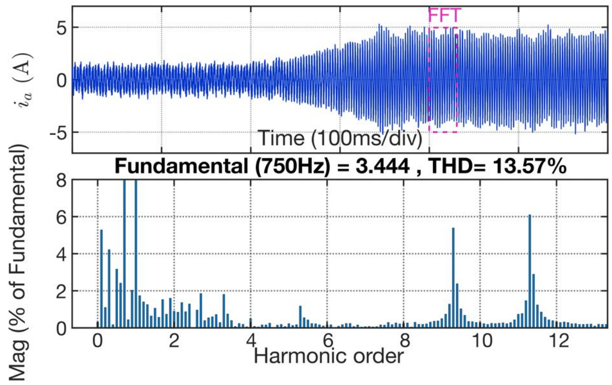

Fig. 5.32: Phase current FFT result of SOGI-HESO-based PI with step speed change at 50% rated load.

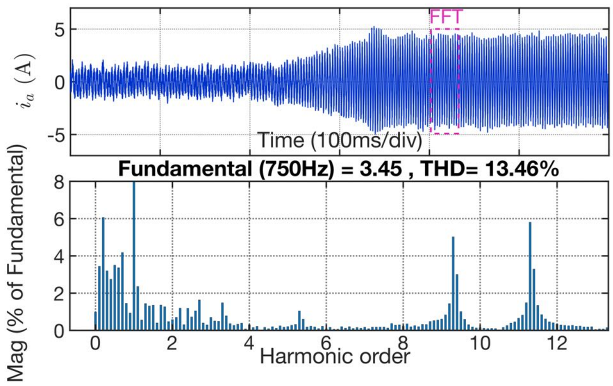

Fig. 5.33: Phase current FFT result of SOGI-HESO-based LADRC with step speed change at 50% rated load.

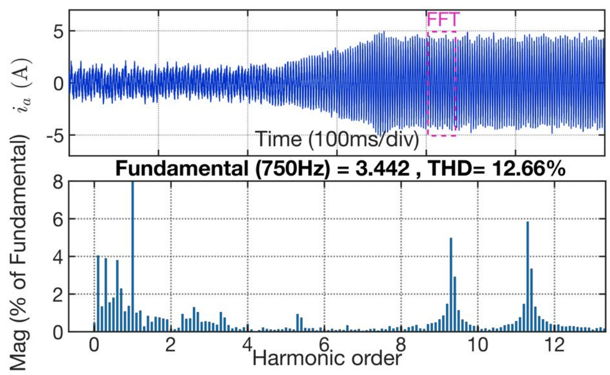

Fig. 5.34: Phase current FFT result of SOGI-HESO-based ALADRC with step speed change at 50% rated load.

Table 5.5: The transient performance for different controllers.

Items	PI	LADRC	ALADRC
Speed error at 12,000 r/min	118 r/min	96 r/min	83 r/min
Speed error at 15,000 r/min	95 r/min	90 r/min	80 r/min
Peak overshoot (r/min)	123	97	89
Peak to Peak i_d (A)	2.75	2.38	2.27
Peak to Peak i_q (A)	2.15	1.86	1.67
Phase current i_a THD (%)	13.57	13.46	12.66

the effectiveness of adaptive bandwidth adjustment in enhancing dynamic response for high-speed operating conditions. The transient performance results are listed in Table 5.5, and the transient metrics follow the definitions in Table 4.2. As quantified in Table 5.5, the ALADRC reduces peak speed overshoot by 28% and peak-to-peak i_q ripple by 22% compared with the PI controller under speed-step from 12,000 to 15,000 r/min.

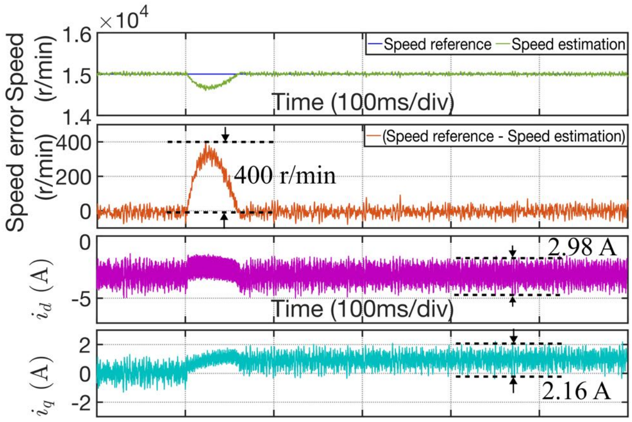

Fig. 5.35: SOGI-HESO-based PI with step load change from 0 to 60% rated load at 15,000 r/min.

In Figs. 5.35-5.37, the speed error amplitudes under a load step are 400 r/min, 375 r/min, and 355 r/min for the PI, LADRC, and ALADRC controllers, respectively. Under the load step change, the $d-$ and $q-$axis current waveforms indicate that the proposed ALADRC method effectively reduces both the oscillation amplitude and the current tracking error compared to the other control strategies.

Furthermore, FFT analysis of the phase current i_a reveals total harmonic distortion (THD) values of 13.86% for PI, 13.41% for LADRC, and 12.97% for ALADRC, demonstrating that the proposed

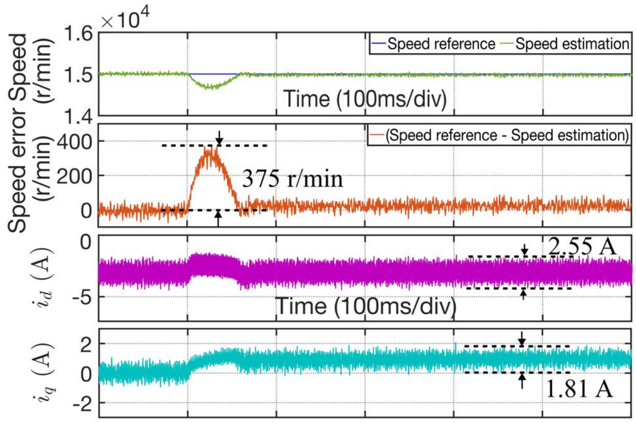

Fig. 5.36: SOGI-HESO-based LADRC with step load change from 0 to 60% rated load at 15,000 r/min.

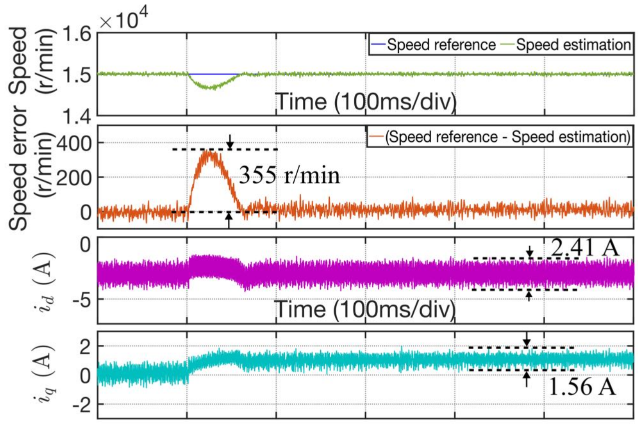

Fig. 5.37: SOGI-HESO-based ALADRC with step load change from 0 to 60% rated load at 15,000 r/min.

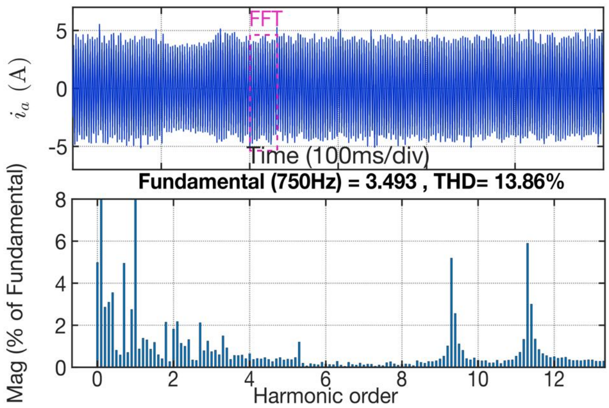

Fig. 5.38: Phase current FFT result of SOGI-HESO-based PI with step load change.

SOGI-HESO-based ALADRC not only enhances speed control performance but also improves current quality, as shown in Figs 5.38 to 5.40.

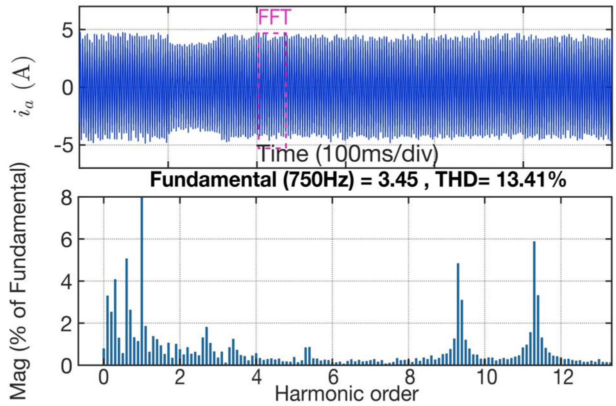

Fig. 5.39: Phase current FFT result of SOGI-HESO-based LADRC with step load change.

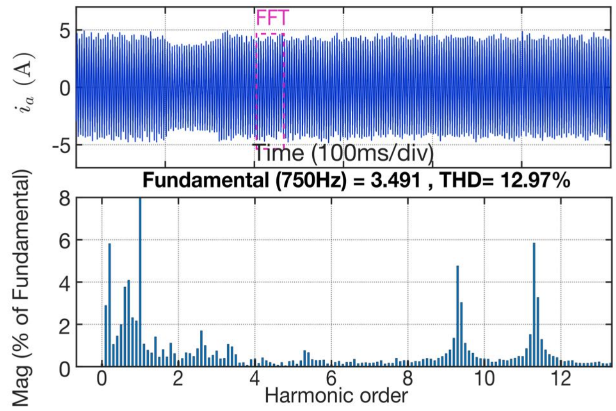

Fig. 5.40: Phase current FFT result of SOGI-HESO-based ALADRC with step load change.

5.5.3 Parameters Mismatch and Speed Range Analysis

From Fig. 5.41 to Fig. 5.47, the parameter robustness under varying load conditions and the operation speed range test are presented, respectively.

The parameter mismatch tests are presented in Figs. 5.41 to 5.46. In Figs. 5.42 to 5.46, the proposed SOGI-HESO-based ALADRC maintains stable operation under various parameter mismatch scenarios. As shown in Figs. 5.44 and 5.45, the slightly smaller speed errors in 1.2 ψ_f and 0.8 L_s arise because these mismatches effectively ease control. Higher flux improves the BEMF signal-to-noise ratio and reduces the i_q needed for a given load, while lower inductance shortens the electrical time constant, making the current loop faster. In contrast, 1.2 L_s degrades dynamics and yields the largest error, consistent with the expected trend.

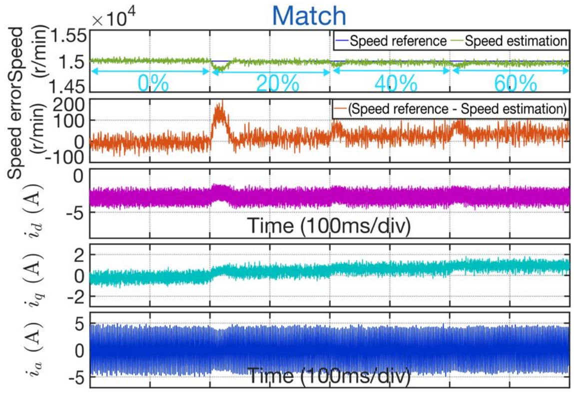

Fig. 5.41: Results of speed estimation, speed error, $d-$and $q-$axis currents, and phase current with varying load conditions at parameters match.

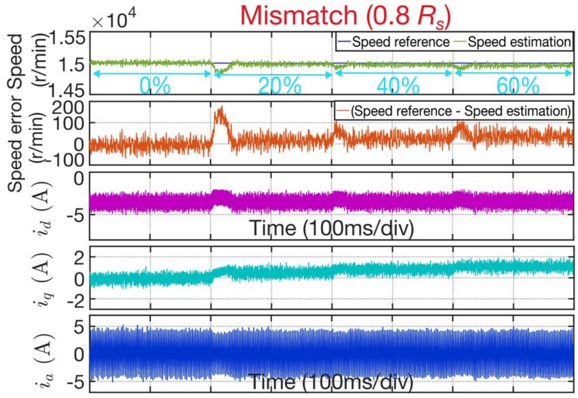

Fig. 5.42: Results of speed estimation, speed error, $d-$and $q-$axis currents, and phase current with varying load conditions at parameters mismatch $0.8R_s$.

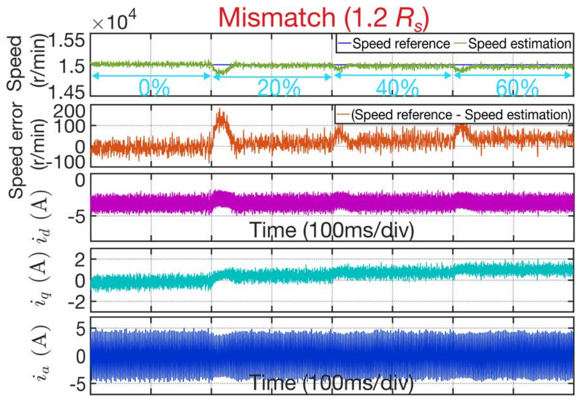

Fig. 5.43: Results of speed estimation, speed error, $d-$and $q-$axis currents, and phase current with varying load conditions at parameters mismatch $1.2R_s$.

In the FW region, underestimating the magnet flux (0.8 ψ_f) commands a less negative i_d and a larger i_q, which increases the effective flux and thus u_q toward the voltage limit, risking PWM saturation and loss of regulation. Therefore, to avoid damage to the hardware, this result is not

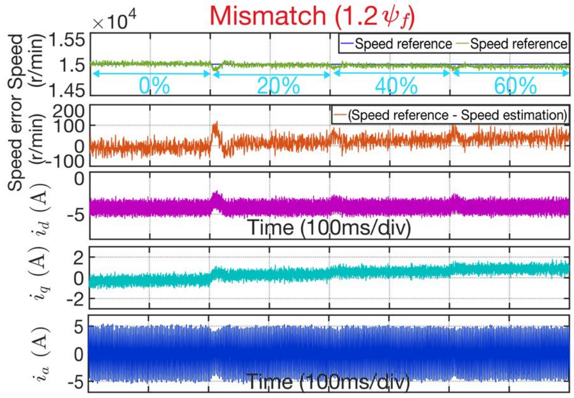

Fig. 5.44: Results of speed estimation, speed error, $d-$and $q-$axis currents, and phase current with varying load conditions at parameters mismatch $1.2\psi_f$.

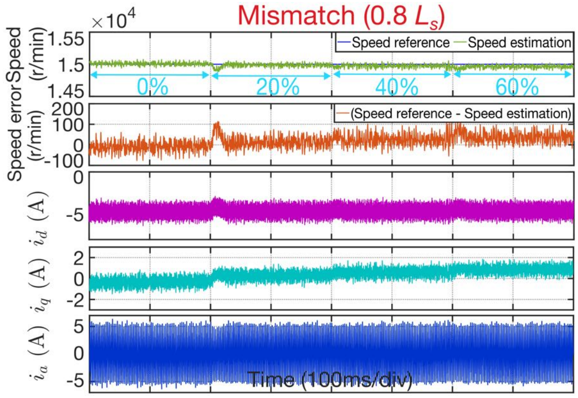

Fig. 5.45: Results of speed estimation, speed error, $d-$and $q-$axis currents, and phase current with varying load conditions at parameters mismatch $0.8L_s$.

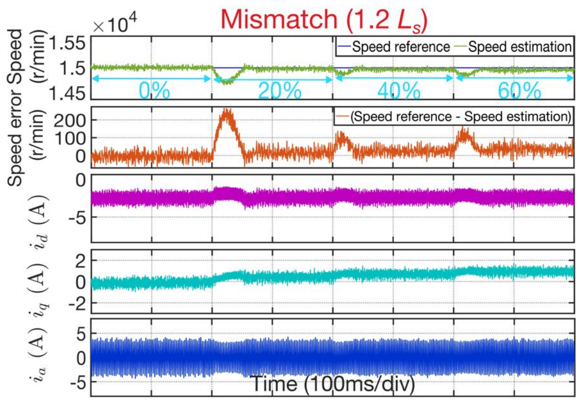

Fig. 5.46: Results of speed estimation, speed error, $d-$and $q-$axis currents, and phase current with varying load conditions at parameters mismatch $1.2L_s$.

included.

These results indicate that parameter mismatches have little impact on the performance of the

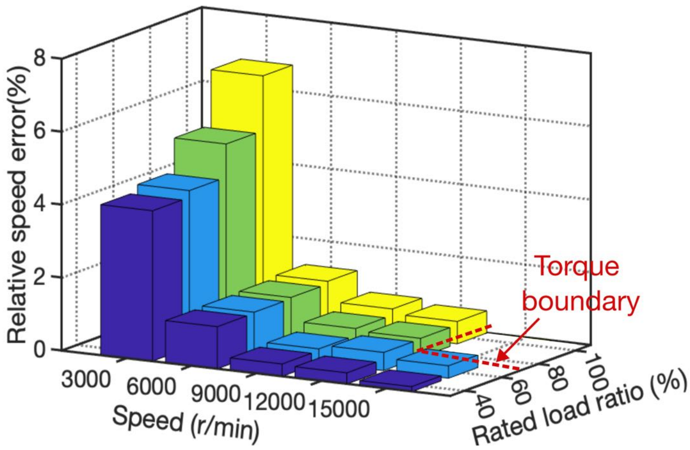

Fig. 5.47: Relative speed error at various speeds and load conditions.

proposed SOGI-HESO-based ALADCR. Furthermore, the proposed method demonstrates a rapid dynamic response to abrupt load variations, effectively tracking sudden torque commands.

To validate the operational speed range, the proposed method was evaluated starting from a low speed and variable load conditions, with the corresponding estimation performance included. The relative speed estimation error, defined as the deviation between the estimated speed and the reference speed, normalized to the reference, is used to assess estimation accuracy across different speeds. As shown in Fig. 5.47, the lowest tested speed in the experiment is 3000 r/min. The results indicate that the relative speed estimation error is highest at low speeds with rated load, and decreases as the motor accelerates, which is consistent with the characteristics of HESO-based sensorless control. While the proposed method is optimized for high-speed operation, it remains functional in the lower-speed region.

5.6 Summary

In this chapter, a second-order generalized integrator - high-order extended state observer (SOGI-HESO) combined with an adaptive linear active disturbance rejection control (ALADRC) strategy was proposed to improve rotor position estimation accuracy and the speed control performance of sensorless high-speed SPMSM operating in the FW region. The design methodology of the SOGI-HESO framework was presented, emphasizing its ability to attenuate current harmonics and measurement noise, improving the BEMF estimation quality and reducing phase lag. Additionally, an ALADRC with real-time bandwidth adaptation was implemented in the speed loop to ensure fast dynamic response and disturbance rejection under varying operating conditions. Experimental validations, including steady-state estimation, transient response, harmonic suppression, and parameter mismatch, demonstrated the effectiveness of the proposed SOGI-HESO with ALADRC, confirming significant improvements in estimation accuracy, robustness, and control performance compared to conventional methods.

Chapter 6

Conclusions and Future Works

6.1 Conclusions

This thesis investigates the modeling, sensorless estimation, and robust control of high-speed SPMSMs, addressing the challenges of fast electromagnetic analysis, high-speed position estimation, and system robustness under flux-weakening operation. To achieve accurate, stable, and efficient control of high-speed SPMSMs, three key methodologies were proposed and validated, forming a unified framework that bridges model simplification, sensorless estimation, and robust control. The presented work provides theoretical insights and experimental foundations for improving both control precision and computational efficiency in high-speed motor systems.

The major contributions of this thesis can be summarized as follows:

1. In terms of fast and accurate electromagnetic modeling, a MOR method based on POD was proposed for the electromagnetic performance analysis of BPMSMs.
    - The proposed method significantly reduces computation time while maintaining high accuracy in torque, flux density, and levitation force estimation, achieving errors below 2% compared with FEA.
    - The motivation stems from the need for rapid yet precise evaluation to support high-speed sensorless and robust control development, as MOR enables efficient iterative analysis without compromising fidelity.

2. In terms of sensorless estimation accuracy and dynamic performance, a cascade high-order extended state observer (CHESO) was proposed to enhance rotor position and speed estimation for high-speed PMSMs. Experimental validation, including steady-state rotor position estimation, transient performance evaluation, and adaptive feedforward compensation tests, demonstrated the effectiveness and improvements offered by the proposed sensorless control strategy for high-speed SPMSMs.

    - The design integrates two-level observer structures to improve noise suppression and transient tracking.
    - Compared with the conventional LESO, the CHESO achieves higher estimation accuracy and superior robustness over a wide speed range.
    - An adaptive feedforward control strategy was employed to enhance the dynamic response and disturbance rejection capabilities of the high-speed SPMSM drive system.

3. In terms of sensorless control in the flux-weakening (FW) region, a second-order generalized integrator – high-order extended state observer (SOGI-HESO) combined with an adaptive linear active disturbance rejection control (ALADRC) scheme was developed. Experimental validations, including steady-state estimation, transient response, harmonic suppression, and parameter mismatch, demonstrated the effectiveness of the proposed SOGI-HESO with ALADRC, confirming significant improvements in estimation accuracy, robustness, and control performance compared to conventional methods.

    - The proposed SOGI-HESO improves BEMF estimation accuracy, reduces phase lag, and provides smoother control transitions during rapid acceleration.
    - The adaptive bandwidth design dynamically balances noise attenuation and fast response, enhancing control performance under flux-weakening and high-speed operations.

The proposed control framework is application-adaptable through parameter tuning rather than structural redesign. For electric vehicle applications, control parameters can be tuned to prioritise torque smoothness, efficiency, and wide-speed-range operation, while for flywheel energy storage systems, the emphasis can be shifted toward ultra-high-speed operation, fast transient response, and robustness against parameter variations. In both cases, the same observer and controller structures are retained, with tuning parameters and operating constraints adjusted to meet application-specific performance requirements, demonstrating the flexibility and practicality of the proposed approach.

In conclusion, these studies form a coherent and progressive framework that enables high-speed PMSMs to achieve improved efficiency, estimation accuracy, and robust performance under sensorless operational conditions, laying the theoretical and experimental foundation for the practical deployment of high-speed SPMSMs in energy and transportation systems. The developed modeling and control methodologies provide a solid foundation for future research into data-driven and robust control systems for high-speed PMSM drives.

6.2 Suggestions for Future Research Directions

While the solutions presented in this thesis address critical challenges, further research is needed to expand their applicability and robustness under broader conditions.

The research conducted in this thesis provides valuable insights into the modeling, control, and sensorless operation of high-speed PMSMs. Although significant progress has been achieved in improving estimation accuracy, dynamic performance, and system robustness, several aspects require further investigation to enhance the generality and practical applicability of the proposed methods. The following issues still need to be further considered:

1. This thesis primarily focuses on sensorless control. Further studies should aim to integrate optimized pulse patterns to minimize harmonics and switching losses while combining them with advanced iron loss estimation techniques to improve overall system efficiency. Investigating modulation schemes that balance efficiency and thermal stress in high-speed operations remains an important direction for future research. Also, future work should include a systematic evaluation of electromagnetic interference (EMI) effects on sensorless estimation accuracy and the co-design of control algorithms and hardware-level EMI mitigation strategies for high-speed PMSM drives.

2. The current work mainly relies on physics-based observer design for sensorless estimation and control. Future work should explore hybrid approaches that integrate data-driven algorithms with conventional observer frameworks to capture nonlinear effects, aging, and parameter

variations. The development of adaptive hybrid models combining fast dynamic response with learning-based adaptability could significantly improve system robustness and real-time performance.

3. While this thesis focuses on control and estimation, the long-term reliability and maintenance of high-speed SPMSM systems have not been addressed. Future research should incorporate predictive maintenance frameworks that use historical and real-time data for fault diagnosis and lifetime prediction. Developing intelligent decision-making tools capable of autonomous derating and component replacement scheduling would enhance reliability, reduce downtime, and support sustainable operation in industrial and transportation applications.

These future directions will extend the scope of this research, bridging high-performance control with practical reliability, efficiency, and sustainability in large-scale industrial and transportation applications.

Appendix A

Reproducibility and Implementation Details

This appendix summarises the software environment, implementation platform, sampling rates, tuning parameters, and operating conditions used in this thesis.

Table A.1: Reproducibility and Implementation Summary

Item	Description	Software version/ Parameter value
Software environment	MATLAB/Simulink used for modelling and simulation. Control and observer algorithms implemented in discrete time and deployed using embedded C code.	MATLAB R2023b
Implementation platform	Experimental validation carried out on a dSPACE real-time control platform. ControlDesk is used for parameter tuning, signal monitoring, and data acquisition.	dSPACE MicroLabBox (DS1202), dSPACE ControlDesk 2024-A
Sampling rates and switching frequency	The inverter switching frequency was set equal to the current control and observer update rate. Sampling rates were kept constant during each experiment.	10kHz
Observer and controller tuning	LESO, CHESO, and SOGI-HESO observers designed using bandwidth-based tuning rules, with observer bandwidth selected as a conservative multiple of the electrical fundamental frequency. PI and ALADRC speed controllers tuned using conventional frequency-domain guidelines to ensure stability and acceptable transient response.	Listed in Tables 4.6, 5.3
Operating conditions for comparison	Main comparisons conducted under medium- and high-speed operation, including flux-weakening regions. Dynamic performance evaluated using step speed and step load torque changes. Robustness tests performed with stator resistance, inductance, and permanent-magnet flux varied from 80% to 120% of nominal values.	Results listed in Tables 4.7, 5.4 and 5.5
Simulation and experimental validation	Model order reduction results in Chapter 3 are validated against finite element simulations, while the sensorless estimation and control results in Chapters 4 and 5 are validated through both simulation and experimental testing.	Experimental results in Chapters 4.6 and 5.5

Bibliography

[1] Shangjian Dai, JB Wang, Zhigang Sun, and Ellis Chong. Deadbeat predictive current control for high-speed PMSM drives with low switching-to-fundamental frequency ratios. *IEEE Transactions on Industrial Electronics*, 69(5):4510–4521, 2022.

[2] Fengyan Yi, Qingqing Su, Chunxiao Feng, Xingmao Wang, Lei Yang, Jiaming Zhou, Zhixian Fan, Shangfeng Jiang, Zhiming Zhang, Tao Yu, et al. Response analysis and stator optimization of ultrahigh-speed PMSM for fuel cell electric air compressor. *IEEE Transactions on Transportation Electrification*, 9(4):5098–5110, 2022.

[3] Muhammad Saad Rafaq and Jin-Woo Jung. A comprehensive review of state-of-the-art parameter estimation techniques for permanent magnet synchronous motors in wide speed range. *IEEE Transactions on Industrial Informatics*, 16(7):4747–4758, 2019.

[4] Sarbajit Paul, Jae-Gil Lee, Pil-Wan Han, Junghwan Chang, and Xuan-Truong Luong. Design consideration of rectangular conductors and slot wedge for ac winding loss reduction in high speed train traction motor. *IEEE Transactions on Vehicular Technology*, 73(11):16543–16556, 2024. doi: 10.1109/TVT.2024.3422508.

[5] Yongping Sun, Ming Yang, Bo Wang, Yangyang Chen, and Dianguo Xu. Precise position control based on resonant controller and second-order sliding mode observer for PMSM-driven feed servo system. *IEEE Transactions on Transportation Electrification*, 9(1):196–209, 2022.

[6] Quanyao Yang, Kun Mao, Shiqiang Zheng, Chong Zhou, and Qing Zhong. Position sensorless drive with online parameters estimation for magnetic suspension centrifugal compressor. *IEEE Transactions on Power Electronics*, 38(8):9384–9394, 2023.

[7] Caiyong Ye, Dezuan Yu, Kaifeng Liu, Yongzihao Dai, Cong Deng, Jiangtao Yang, and Jianping Zhang. Research of a stator PM excitation solid rotor machine for flywheel energy storage system. *IEEE Transactions on Industrial Electronics*, 69(12):12140–12151, 2021.

[8] Baiqi Zang and Yiguang Chen. Multiobjective optimization and multiphysics design of a 5 MW high-speed IPMSM used in FESS based on NSGA-II. *IEEE Transactions on Energy Conversion*, 38(2):813–824, 2022.

[9] Lammotor. Comparison of motor stator and rotor technologies of Tesla, BYD, and Huawei. Available online:`https://lammotor.com/comparison-of-motor-of-tesla-byd-and-huawei/`, 2024. (accessed on 26 September 2025).

[10] EMBER EMBER. Electricity data explorer. Available online:`https://ember-energy.org/data/electricity-data-explorer/?data=generation&fuel=wind_and_solar&tab=main&chart=trend`, 2025. (accessed on 20 September 2025).

[11] Fritz Braeuer, Julian Rominger, Russell McKenna, and Wolf Fichtner. Battery storage systems: An economic model-based analysis of parallel revenue streams and general implications for industry. *Applied Energy*, 239:1424–1440, 2019.

[12] Marvin Killer, Mana Farrokhseresht, and Nikolaos G Paterakis. Implementation of large-scale li-ion battery energy storage systems within the emea region. *Applied energy*, 260: 114166, 2020.

[13] Reza Hemmati and Hedayat Saboori. Emergence of hybrid energy storage systems in renewable energy and transport applications–A review. *Renewable and Sustainable Energy Reviews*, 65:11–23, 2016.

[14] Kai Xu, Youguang Guo, Gang Lei, and Jianguo Zhu. A review of flywheel energy storage system technologies. *Energies*, 16(18):6462, 2023.

[15] Michiel Koot, John TBA Kessels, Bram De Jager, WPMH Heemels, PPJ Van den Bosch, and Maarten Steinbuch. Energy management strategies for vehicular electric power systems. *IEEE transactions on vehicular technology*, 54(3):771–782, 2005.

[16] Hasan Mehrjerdi. Dynamic and multi-stage capacity expansion planning in microgrid integrated with electric vehicle charging station. *Journal of Energy Storage*, 29:101351, 2020.

[17] Paolo Lazzeroni, Sergio Olivero, Maurizio Repetto, Federico Stirano, and Marc Vallet. Optimal battery management for vehicle-to-home and vehicle-to-grid operations in a residential case study. *Energy*, 175:704–721, 2019.

[18] Junqiang He, Changli Shi, Tongzhen Wei, and Dongqiang Jia. Stochastic model predictive control of hybrid energy storage for improving agc performance of thermal generators. *IEEE Transactions on Smart Grid*, 13(1):393–405, 2021.

[19] Hossein Azizi Moghaddam, Mohammad Hosein Saeedinia, Sobhan Mohamadian, Mohammad Saeed Mahdavi, and Gevork B Gharehpetian. Integrated modeling of power network and connected flywheel energy storage system for optimal power and energy ratings of flywheel. *IEEE Transactions on Energy Conversion*, 36(3):1589–1599, 2020.

[20] Andrea Floris, Mario Porru, Alfonso Damiano, and Alessandro Serpi. Energy management and control system design of an integrated flywheel energy storage system for residential users. *Applied Sciences*, 11(10):4615, 2021.

[21] CRRC. Unveiling the future of high-speed rail: CR450 EMU prototype debuts at 400 km/h a breakthrough in rail technology, the CR450 EMU sets new standards for speed, safety, and comfort. Available online:`https://www.crrcgc.cc/en/2025-02/13/article_20250213172030823O5.html`, 2025. (accessed on 26 September 2025).

[22] Giordano Scarciotti and Alessandro Astolfi. Data-driven model reduction by moment matching for linear and nonlinear systems. *Automatica*, 79:340–351, 2017.

[23] Kuan Lu, Kangyu Zhang, Haopeng Zhang, Xiaohui Gu, Yulin Jin, Shibo Zhao, Chao Fu, and Yongfeng Yang. A review of model order reduction methods for large-scale structure systems. *Shock and Vibration*, 2021(1):6631180, 2021.

[24] Cao Guoyun, Wang Chong, and Chen Chen. Center manifold method to simplify the analysis of fold bifurcation associated with voltage collapse. *Proceedings-Chinese Society of Electrical Engineering*, 22(7):40–43, 2002.

[25] Chen Gang, Sun Jian, and Li Yueming. Active flutter suppression control law design method based on balanced proper orthogonal decomposition reduced order model. *Nonlinear Dynamics*, 70(1):1–12, 2012.

[26] Shangjiang Guo and Li Ma. Stability and bifurcation in a delayed reaction–diffusion equation with dirichlet boundary condition. *Journal of Nonlinear Science*, 26(2):545–580, 2016.

[27] María-Luisa Rapún and José M Vega. Reduced order models based on local POD plus Galerkin projection. *Journal of Computational Physics*, 229(8):3046–3063, 2010.

[28] Joseph A Beck, Jeffrey M Brown, Charles J Cross, and Joseph C Slater. Component-mode reduced-order models for geometric mistuning of integrally bladed rotors. *AIAA journal*, 52 (7):1345–1356, 2014.

[29] Katarzyna Bizon, Gaetano Continillo, Marek Berezowski, and Joanna Smu la-Ostaszewska. Optimal model reduction by empirical spectral methods via sampling of chaotic orbits. *Physica D: Nonlinear Phenomena*, 241(17):1441–1449, 2012.

[30] Zhongqiang Zhang, Xiu Yang, and Guang Lin. POD-based constrained sensor placement and field reconstruction from noisy wind measurements: A perturbation study. *Mathematics*, 4(2):26, 2016.

[31] Changpin Li and Li Ma. Lyapunov–schmidt reduction for fractional differential systems. *Journal of Computational and Nonlinear Dynamics*, 11(5):051022, 2016.

[32] David Amsallem, Matthew Zahr, Youngsoo Choi, and Charbel Farhat. Design optimization using hyper-reduced-order models. *Structural and Multidisciplinary Optimization*, 51(4): 919–940, 2015.

[33] Dan Xie and Min Xu. A comparison of numerical and semi-analytical proper orthogonal decomposition methods for a fluttering plate. *Nonlinear Dynamics*, 79(3):1971–1989, 2015.

[34] Zhaoli Zheng, Fahui Zhu, Di Zhang, and Yonghui Xie. A developed component mode synthesis for parametric response analysis of large-scale asymmetric rotor. *Journal of Mechanical Science and Technology*, 33(3):995–1005, 2019.

[35] Colas Joannin, Benjamin Chouvion, Fabrice Thouverez, Jean-Philippe Ousty, and Moustapha Mbaye. A nonlinear component mode synthesis method for the computation

of steady-state vibrations in non-conservative systems. *Mechanical Systems and Signal Processing*, 83:75–92, 2017.

[36] Dan Yu and Suman Chakravorty. A randomized proper orthogonal decomposition technique. In *2015 American Control Conference (ACC)*, pages 1137–1142. IEEE, 2015.

[37] David B Segala and Peiman Naseradinmousavi. On the inclusion of time derivatives of state variables for parametric model order reduction for a beam on a nonlinear foundation. *Journal of Dynamic Systems, Measurement, and Control*, 139(8):081009, 2017.

[38] Fangxiong Cheng, Hui Xu, and Xinlong Feng. Model order reduction method based on (r) POD-ANNs for parameterized time-dependent partial differential equations. *Computers & Fluids*, 241:105481, 2022.

[39] Sarbajit Paul and Junghwan Chang. Fast numerical analysis of electric motor using nonlinear model order reduction. *IEEE Transactions on Magnetics*, 54(3):1–4, 2017.

[40] Hiroki Sakamoto, Kazuya Okamoto, and Hajime Igarashi. Fast analysis of rotating machine using simplified model-order reduction based on POD. *IEEE transactions on magnetics*, 56 (2):1–4, 2020.

[41] Yuki Sato, Felipe Campelo, and Hajime Igarashi. Fast shape optimization of antennas using model order reduction. *IEEE Transactions on Magnetics*, 51(3):1–4, 2015.

[42] Sk Mashfiqur Rahman, Omer San, and Adil Rasheed. A hybrid approach for model order reduction of barotropic quasi-geostrophic turbulence. *Fluids*, 3(4):86, 2018.

[43] Kai Li, Jiaqing Kou, and Weiwei Zhang. Unsteady aerodynamic reduced-order modeling based on machine learning across multiple airfoils. *Aerospace Science and Technology*, 119: 107173, 2021.

[44] Xu Wang, Jiaqing Kou, and Weiwei Zhang. Unsteady aerodynamic prediction for iced airfoil based on multi-task learning. *Physics of Fluids*, 34(8), 2022.

[45] Daning Huang and Peretz P Friedmann. An aerothermoelastic analysis framework with reduced-order modeling applied to composite panels in hypersonic flows. *Journal of Fluids and Structures*, 94:102927, 2020.

[46] Jiajia Chen, Sideng Hu, Zhou Qiang, Shiyou Yang, and Zhuoxiang Ren. A broadband enhanced nodal-order reduction methodology for large-scale equation sets of 3-D transient field problems. *IEEE Transactions on Magnetics*, 56(3):1–4, 2020.

[47] Alberto Oliveri, Matteo Lodi, Mauro Parodi, Flavio Stellino, and Marco Storace. Model reduction for optimized online compensation of hysteresis and creep in piezoelectric actuators. *IEEE Transactions on Circuits and Systems II: Express Briefs*, 65(11):1748–1752, 2017.

[48] Antoine Pierquin, Thomas Henneron, Stéphane Clenet, and Stephane Brisset. Model-order reduction of magnetoquasi-static problems based on POD and Arnoldi-based Krylov methods. *IEEE Transactions on Magnetics*, 51(3):1–4, 2015.

[49] Daniel Klis, Stefan Burgard, Ortwin Farle, and Romanus Dyczij-Edlinger. A self-adaptive model-order reduction algorithm for nonlinear eddy-current problems based on quadratic–bilinear modeling. *IEEE Transactions on Magnetics*, 52(3):1–4, 2015.

[50] Cameron Entzminger, Wei Qiao, Liyan Qu, and Jerry L Hudgins. A high-accuracy, low-order thermal model of SiC MOSFET power modules extracted from finite element analysis via model order reduction. In *2019 IEEE Energy Conversion Congress and Exposition (ECCE)*, pages 4950–4954. IEEE, 2019.

[51] Fabian Müller, Andreas Siokos, Johann Kolb, Martin Nell, and Kay Hameyer. Efficient estimation of electrical machine behavior by model order reduction. *IEEE Transactions on Magnetics*, 57(6):1–4, 2021.

[52] L Montier, T Henneron, S Clenet, and B Goursaud. Model order reduction applied to a linear finite element model of a squirrel cage induction machine based on POD approach. *IEEE Transactions on Magnetics*, 57(6):1–4, 2021.

[53] Oliver Lass and Stefan Ulbrich. Model order reduction techniques with a posteriori error control for nonlinear robust optimization governed by partial differential equations. *SIAM Journal on Scientific Computing*, 39(5):S112–S139, 2017.

[54] Mehrnaz Farzam Far, Floran Martin, Anouar Belahcen, Paavo Rasilo, and Hafiz Asad Ali Awan. Real-time control of an IPMSM using model order reduction. *IEEE Transactions on Industrial Electronics*, 68(3):2005–2014, 2020.

[55] Kazuya Okamoto, Hiroki Sakamoto, and Hajime Igarashi. Implementation of simplified model order reduction based on POD for dynamic simulation of electric motors. In *2019 22nd International Conference on the Computation of Electromagnetic Fields (COMPUMAG)*, pages 1–4. IEEE, 2019.

[56] Toshihito Shimotani, Yuki Sato, Takahiro Sato, and Hajime Igarashi. Fast finite-element analysis of motors using block model order reduction. *IEEE transactions on magnetics*, 52 (3):1–4, 2015.

[57] Thomas Henneron and Stéphane Clenet. Model order reduction applied to the numerical study of electrical motor based on POD method taking into account rotation movement. *International Journal of Numerical Modelling: Electronic Networks, Devices and Fields*, 27(3):485–494, 2014.

[58] Laurent Montier, Thomas Henneron, Stéphane Clénet, and Benjamin Goursaud. Transient simulation of an electrical rotating machine achieved through model order reduction. *Advanced Modeling and Simulation in Engineering Sciences*, 3(1):10, 2016.

[59] Abel Sancarlos, Elias Cueto, Francisco Chinesta, and Jean-Louis Duval. A novel sparse reduced order formulation for modeling electromagnetic forces in electric motors. *SN Applied Sciences*, 3(3):1–19, 2021.

[60] Xiaodong Sun, Zhengwang Xue, Jianguo Zhu, Youguang Guo, Zebin Yang, Long Chen, and Jianfeng Chen. Suspension force modeling for a bearingless permanent magnet synchronous motor using Maxwell stress tensor method. *IEEE Transactions on Applied Superconductivity*, 26(7):1–5, 2016.

[61] Xiaodong Sun, Yichen Shen, Zhi Zhou, Zebin Yang, and Long Chen. Modeling and control of a bearingless permanent magnet synchronous motor. *International Journal of Applied Electromagnetics and Mechanics*, 53(1):151–165, 2017.

[62] Yueping Sun, Bokai Su, and Xiaodong Sun. Optimal design and performance analysis for interior composite-rotor bearingless permanent magnet synchronous motors. *IEEE Access*, 7:7456–7465, 2018.

[63] Zhuang Xu and Chris Gerada. An extended state loop filter with position error observer for sensorless IPMSM drives. *IEEE Transactions on Industrial Electronics*, 69(12):12213–12224, 2022. doi: 10.1109/TIE.2021.3134061.

[64] Giulio De Donato, Giacomo Scelba, Mario Pulvirenti, Giuseppe Scarcella, and Fabio Giulii Capponi. Low-cost, high-resolution, fault-robust position and speed estimation for PMSM drives operating in safety-critical systems. *IEEE Transactions on Power Electronics*, 34(1):550–564, 2019. doi: 10.1109/TPEL.2018.2820042.

[65] Ying Zuo, Chunyan Lai, and K. Lakshmi Varaha Iyer. A review of sliding mode observer based sensorless control methods for PMSM drive. *IEEE Transactions on Power Electronics*, 38(9):11352–11367, 2023. doi: 10.1109/TPEL.2023.3287828.

[66] Zhendong Zhang. Sensorless back EMF based control of synchronous PM and reluctance motor drives—A review. *IEEE Transactions on Power Electronics*, 37(9):10290–10305, 2022. doi: 10.1109/TPEL.2022.3162963.

[67] Ali Habib Almarhoon, Z. Q. Zhu, and Peilin Xu. Improved rotor position estimation accuracy by rotating carrier signal injection utilizing zero-sequence carrier voltage for dual three-phase PMSM. *IEEE Transactions on Industrial Electronics*, 64(6):4454–4462, 2017. doi: 10.1109/TIE.2016.2561261.

[68] Gaolin Wang, Maria Valla, and Jorge Solsona. Position sensorless permanent magnet synchronous machine drives—A review. *IEEE Transactions on Industrial Electronics*, 67 (7):5830–5842, 2020. doi: 10.1109/TIE.2019.2955409.

[69] Yonggang Li, Yashan Hu, and Weimin Wu. Full-speed range sensorless control scheme for dual three-phase IPMSM based on dual decoupled sub-spaces. In *2025 IEEE 8th International Electrical and Energy Conference (CIEEC)*, pages 190–197, 2025. doi: 10.1109/CIEEC64805.2025.11116338.

[70] Zhuang Xu, Tianru Zhang, Yuli Bao, He Zhang, and Chris Gerada. A nonlinear extended state observer for rotor position and speed estimation for sensorless IPMSM drives. *IEEE Transactions on Power Electronics*, 35(1):733–743, 2019.

[71] Dario Pasqualotto, Saverio Rigon, and Mauro Zigliotto. Sensorless speed control of synchronous reluctance motor drives based on extended Kalman filter and neural magnetic model. *IEEE Transactions on Industrial Electronics*, 70(2):1321–1330, 2022.

[72] Abhisek Pal, Sukanta Das, and Ajit K Chattopadhyay. An improved rotor flux space vector based MRAS for field-oriented control of induction motor drives. *IEEE Transactions on Power Electronics*, 33(6):5131–5141, 2017.

[73] Mengting Ye, Yanfei Cao, Wei Chen, Tingna Shi, and Changliang Xia. Full-speed-range sensorless control of high-speed permanent magnet synchronous motor based on the prediction methodology. *IEEE Transactions on Power Electronics*, 2024.

[74] Mengting Ye, Tingna Shi, Chen Li, Yan Yan, and Changliang Xia. High-precision sensorless control of high-speed permanent magnet synchronous motor based on the prediction methodology. *IEEE Transactions on Power Electronics*, 2024.

[75] Xinda Song, Jiancheng Fang, Bangcheng Han, and Shiqiang Zheng. Adaptive compensation method for high-speed surface PMSM sensorless drives of EMF-based position estimation error. *IEEE Transactions on Power Electronics*, 31(2):1438–1449, 2015.

[76] Zdenek Novak and Martin Novak. Adaptive PLL-based sensorless control for improved dynamics of high-speed pmsm. *IEEE Transactions on Power Electronics*, 37(9):10154–10165, 2022.

[77] Mingjin Hu, Wenfei Yu, Jiaxin Lei, Zheng Wu, Wei Hua, and Yinfeng Hu. Sensorless control of a high-speed PMSM with rapid acceleration for air compressors using a high-order extended state observer. In *2021 IEEE Energy Conversion Congress and Exposition (ECCE)*, pages 4781–4787. IEEE, 2021.

[78] Jindong Zhang, Fei Peng, Yunkai Huang, Yu Yao, and Zichong Zhu. Online inductance identification using PWM current ripple for position sensorless drive of high-speed surface-mounted permanent magnet synchronous machines. *IEEE Transactions on Industrial Electronics*, 69(12):12426–12436, 2021.

[79] Yinfeng Hu, Kai Liu, Wei Hua, and Mingjin Hu. First-order model based inductance identification with least square method for high-speed sensorless control of permanent

magnet synchronous machines. *IEEE Transactions on Power Electronics*, 38(7):8719–8729, 2023.

[80] Yinfeng Hu, Wei Hua, Mingjin Hu, and Yuchen Wang. Inductance–resistance online identification for sensorless high-speed PMSM considering resistive characteristic of invertor nonlinearity. *IEEE Transactions on Industrial Electronics*, 71(3):2343–2355, 2023.

[81] Lizhi Qu, Wei Qiao, and Liyan Qu. An enhanced linear active disturbance rejection rotor position sensorless control for permanent magnet synchronous motors. *IEEE Transactions on Power Electronics*, 35(6):6175–6184, 2019.

[82] Baiqiang Yu, Anwen Shen, Bao Chen, Xin Luo, Qipeng Tang, Jinbang Xu, and Mingfu Zhu. A compensation strategy of flux linkage observer in SPMSM sensorless drives based on linear extended state observer. *IEEE Transactions on Energy Conversion*, 37(2):824–831, 2021.

[83] Feng Jiang, Songjun Sun, Anming Liu, Yunliu Xu, Zhixiong Li, Xicai Liu, and Kai Yang. Robustness improvement of model-based sensorless SPMSM drivers based on an adaptive extended state observer and an enhanced quadrature PLL. *IEEE Transactions on Power Electronics*, 36(4):4802–4814, 2020.

[84] Yonggang Li, Yashan Hu, Xiandong Ma, and Li Liu. Sensorless control of dual three-phase IPMSM based on frequency adaptive linear extended state observer. *IEEE Transactions on Power Electronics*, 38(11):14492–14503, 2023.

[85] Yan Li, Zhen Chen, Xiaoyong Sun, Zi-Qiang Zhu, and Xiangdong Liu. A generic bandwidth determination method for 3rd-LESO and analysis of the extended 4th-LESO candidates in saliency-based sensorless control. *IEEE Transactions on Energy Conversion*, 39(2):1394–1411, 2023.

[86] Zhiqiang Wang, Xiayu Yan, Xinmin Li, Chen Li, and Tingna Shi. Field weakening control method of SPMSM based on quadrature axis voltage feedback. *IEEE/ASME Transactions on Mechatronics*, pages 1–11, 2025. doi: 10.1109/TMECH.2025.3586950.

[87] Runze Jing, Dawei Ding, Guoqiang Zhang, Qiwei Wang, Gaolin Wang, and Dianguo Xu. Active-damping-based field-weakening control strategy with voltage angle regulation for

high-speed SPMSM drive. *IEEE Transactions on Industrial Electronics*, 71(2):1421–1431, 2024. doi: 10.1109/TIE.2023.3262850.

[88] Léopold Sepulchre, Maurice Fadel, Maria Pietrzak-David, and Guillaume Porte. MTPV flux-weakening strategy for PMSM high speed drive. *IEEE Transactions on Industry Applications*, 54(6):6081–6089, 2018. doi: 10.1109/TIA.2018.2856841.

[89] Leopold Sepulchre, Maurice Fadel, Maria Pietrzak-David, and Guillaume Porte. Flux-weakening strategy for high speed PMSM for vehicle application. In *2016 International Conference on Electrical Systems for Aircraft, Railway, Ship Propulsion and Road Vehicles & International Transportation Electrification Conference (ESARS-ITEC)*, pages 1–7, 2016. doi: 10.1109/ESARS-ITEC.2016.7841413.

[90] Senyi Liu, Zaixin Song, Yuxin Liu, Yong Chen, and Chunhua Liu. Flux-weakening controller design of dual three-phase PMSM drive system with copper loss minimization. *IEEE Transactions on Power Electronics*, 38(2):2351–2363, 2022.

[91] Fei Du, Zheng Liu, Jian Li, Yang Lu, and Guofeng Li. Restart strategy for sensorless control of permanent magnet synchronous motor in flux-weakening region. *IEEE Transactions on Transportation Electrification*, 11(5):11243–11254, 2025. doi: 10.1109/TTE.2025.3574686.

[92] Adrish Bhaumik and Sukanta Das. Predictive torque control strategy for speed adaptive flux observer based sensorless induction motor drive in flux-weakening region. *IEEE Transactions on Power Electronics*, 36(12):14110–14118, 2021. doi: 10.1109/TPEL.2021.3089611.

[93] Dong Guo, Venkata Dinavahi, Qi Wu, and Wei Wang. Sliding mode high speed control of PMSM for electric vehicle based on flux-weakening control strategy. In *2017 36th Chinese Control Conference (CCC)*, pages 3754–3758, 2017. doi: 10.23919/ChiCC.2017.8027944.

[94] Kye-Lyong Kang, Jang-Mok Kim, Keun-Bae Hwang, and Kyung-Hoon Kim. Sensorless control of PMSM in high speed range with iterative sliding mode observer. In *Nineteenth Annual IEEE Applied Power Electronics Conference and Exposition, 2004. APEC '04.*, volume 2, pages 1111–1116 vol.2, 2004. doi: 10.1109/APEC.2004.1295961.

[95] Wenhao Wu, Jingbin Bi, Junlei Wei, Yuhan Zhang, Jixuan Liu, and Hang Yu. Feedforward flux observer based on SOGI current extractor for PMSM sensorless control. In *2024 IEEE*

10th International Power Electronics and Motion Control Conference (IPEMC2024-ECCE Asia), pages 1018–1023. IEEE, 2024.

[96] Xinkai Zhu, Jiwei Huang, Pengda Wang, Yonggang Li, Guangyu Qi, Yucai Wu, Yuling He, and Yongchang Zhang. An improved sliding model observer sensorless control for PMSM based on fuzzy logic controller and DSOGI-FLL. *IEEE Transactions on Transportation Electrification*, 2024.

[97] Li Ding, Yun Wei Li, and Navid R Zargari. Discrete-time SMO sensorless control of current source converter-fed PMSM drives with low switching frequency. *IEEE Transactions on Industrial Electronics*, 68(3):2120–2129, 2020.

[98] Syed Ali Asad Rizvi and Attaullah Y Memon. An extended observer-based robust nonlinear speed sensorless controller for a PMSM. *International Journal of Control*, 92(9):2123–2135, 2019.

[99] Siyi Chen, Ying Luo, and YouGuo Pi. PMSM sensorless control with separate control strategies and smooth switch from low speed to high speed. *ISA transactions*, 58:650–658, 2015.

[100] Cristiano M. Verrelli, Stefano Bifaretti, Emilio Carfagna, Alessandro Lidozzi, Luca Solero, Fabio Crescimbini, and Marco Di Benedetto. Speed sensor fault tolerant PMSM machines: From position-sensorless to sensorless control. *IEEE Transactions on Industry Applications*, 55(4):3946–3954, 2019. doi: 10.1109/TIA.2019.2908337.

[101] Hui Wu, Chun Gan, Hongzhe Wang, Shuanghong Wang, Ronghai Qu, and Xingzhong Liu. Active disturbance rejection speed control with double-stage-ESO considering aperiodic and periodic disturbances for PMSM drives. *IEEE Transactions on Industrial Electronics*, 2025.

[102] Shanfeng Zhu, Wenxin Huang, Yajun Zhao, Xiaogang Lin, Dingfeng Dong, Wen Jiang, Yong Zhao, and Xu Wu. Robust speed control of electrical drives with reduced ripple using adaptive switching high-order extended state observer. *IEEE Transactions on Power Electronics*, 37(2):2009–2020, 2021.

[103] Tianru Zhang, Zhuang Xu, Jing Li, He Zhang, and Chris Gerada. A third-order super-twisting extended state observer for dynamic performance enhancement of sensorless IPMSM drives. *IEEE Transactions on Industrial Electronics*, 67(7):5948–5958, 2019.

[104] Linzhi Wang, Yong Yu, Bo Wang, and Dianguo Xu. Bandwidth-based tuning method for PMSM field-weakening control with speed adaptation. *IEEE Transactions on Industrial Electronics*, 2025.

[105] Wei Xu, Moustafa Magdi Ismail, Yi Liu, and Md Rabiul Islam. Parameter optimization of adaptive flux-weakening strategy for permanent-magnet synchronous motor drives based on particle swarm algorithm. *IEEE Transactions on Power Electronics*, 34(12):12128–12140, 2019.

[106] Soroush Ahooye Atashin, Hossein Abootorabi Zarchi, and Gholamreza Arab Markadeh. Online adaptive current vector adjustment for deep flux-weakening control of IPMSM. *IEEE Transactions on Power Electronics*, 38(2):2339–2350, 2022.

[107] Minghe Tian, Bo Wang, Yong Yu, Qinghua Dong, and Dianguo Xu. Enhanced one degree-of-freedom ADRC with sampled-data iterative learning controller for PMSM uncertain speed fluctuations suppression. *IEEE Transactions on Transportation Electrification*, 10(4): 8321–8335, 2024. doi: 10.1109/TTE.2024.3351097.

[108] Haiyang Cao, Yongting Deng, Yuefei Zuo, Xiufeng Liu, Jianli Wang, and Christopher H. T. Lee. A variable structure ADRC for enhanced disturbance rejection and improved noise suppression of PMSM speed system. *IEEE Transactions on Industrial Electronics*, 72(5): 4481–4495, 2025. doi: 10.1109/TIE.2024.3468613.

[109] Yongchang Zhang, Jialin Jin, and Lanlan Huang. Model-free predictive current control of PMSM drives based on extended state observer using ultralocal model. *IEEE Transactions on Industrial Electronics*, 68(2):993–1003, 2020.

[110] Tianru Zhang, Zhuang Xu, and Chris Gerada. A nonlinear extended state observer for sensorless IPMSM drives with optimized gains. *IEEE Transactions on Industry Applications*, 56(2):1485–1494, 2019.

[111] Hongbo Sun, Xiaoyu Zhang, Xiangbin Liu, and Hongye Su. Adaptive robust sensorless control for PMSM based on improved back EMF observer and extended state observer. *IEEE Transactions on Industrial Electronics*, 2024.

[112] Krzysztof Lakomy and Rafal Madonski. Cascade extended state observer for active disturbance rejection control applications under measurement noise. *ISA transactions*, 109:1–10, 2021.